

# Computational Fluid Dynamics of a Floating Offshore Wind Turbine using OpenFOAM

LUCA SCARLATTI

DELFT UNIVERSITY OF TECHNOLOGY



# COMPUTATIONAL FLUID DYNAMICS OF A FLOATING OFFSHORE WIND TURBINE USING OPENFOAM

Author:

**Luca Scarlatti**

Thesis supervisors:

**Dr.ir. Axelle Viré**  
**Dr.ir. Delphine de Tavernier**

Thesis committee:

**Dr.ir. Axelle Viré**  
**Dr.ir. Oriol Colmes Gene**

Faculty of Aerospace Engineering, Delft University of Technology  
Faculty of Electrical Engineering, Mathematics, Computer Science, Delft University of  
Technology



# ABSTRACT

Floating Offshore Wind Energy represents an enormous potential for the future of wind energy and will play a pivotal role in the global energy transition. However, important technical challenges still need to be overcome by the industry regarding the standardization of processes like transportation, floating substructure concept, and supply chain optimization. To successfully achieve these milestones, FOWTs must be accurately modelled to minimize uncertainties to ultimately attract investors and capital in the industry. This thesis has the objective of developing and validating a high-fidelity model for the hydrodynamics of FOWTs with the ultimate goal of creating reliable results to be used as a benchmark for faster mid-fidelity software mostly used in the offshore industry.

The model expanded throughout this thesis is developed in OpenFOAM C++ framework. The whole numerical model is built upon three main pillars: **Waves2Foam** used for the generation of relaxation zones in the numerical wave tank for wave-current generation and absorption; **MoorDyn/Moody** numerical tools employed for the mooring lines spatial discretization for the station keeping of the floating platform; **InterFoam** applied as the main OpenFOAM solver for the multi-phase solution which, in combination with a mesh morphing technique and a rigid body solver, is capable of deforming the mesh to accommodate the 6DOF motions of the platform.

A sequential approach has been undertaken. The first step involves the simulation of second-order Stokes wave propagation in an infinite 2D wave tank, followed by a sensitivity study with an associated uncertainty quantification. The next step involves conducting 3D simulations of a floating box, comparing motion and forces under different mooring models: dynamic FEM, dynamic lumped mass, and quasi-static catenary. In the last step, the results and lessons learned from the previous studies are combined for coupled hydrodynamic/aerodynamic simulations of the OC4 DeepCwind semi-submersible floater with the 5MW NREL offshore wind turbine. Forces, displacements, and tensions are extrapolated and compared with experimental and numerical results, validating the model's accuracy.

Simulated across diverse wind and wave conditions, the OpenFOAM model demonstrated remarkable robustness and excellent ability to achieve convergence even under challenging environmental conditions, while maintaining a high level of result accuracy. The framework effectively reproduced the hydrodynamic behavior of a Floating Offshore Wind Turbine (FOWT), establishing itself as a dependable and reliable tool for conducting future high-fidelity FOWT simulations.



# ACKNOWLEDGEMENTS

Finalizing this thesis report marks the end of my university career, concluding my Master's in Sustainable Energy Technology at TU Delft. It is an important step for my personal growth as it allows me to work as an engineer and to apply in the real world all the knowledge I have been learning in the past 5 years. The support of my friends and family was crucial for me to get where I am now. First, I would like to thank Axelle Viré and Delphine de Tavernier for following me during the whole thesis project and giving me insightful bits of advice on the technical difficulties I was encountering. I would like to thank Pere Fontera Pericas for sharing with me your precious tips and tricks learned last year during your thesis, saving me lots of time and headaches. I would also like to thank all my friends here in the Netherlands. You have made my journey at TU Delft more exciting and more enjoyable, giving life to moments that I will remember smiling for the rest of my life. You have supported me in moments of need and celebrated me on successful occasions, making me feel like I was at home.

I would like to thank my girlfriend Chiara, for always being there for me. In every moment and especially during the toughest ones, you would always give me the strength to keep striving towards my goals and my dreams. To my friends in Genova, no matter how far I have been from Italy in the past years, our friendship never faded away, and our friendly competitions made us reach goals that none of us would have ever imagined. Finally, to my family back in Italy, who have been dealing with me for almost 24 years. Thanks for giving me unconditional support and love for all the choices I made during my life, and thanks for being someone I always look up to.

*Luca Scarlatti  
Delft, November 2023*



# CONTENTS

<b>Abstract</b>	<b>iii</b>
<b>Acknowledgements</b>	<b>v</b>
<b>List of Figures</b>	<b>ix</b>
<b>List of Tables</b>	<b>xiii</b>
<b>Nomenclature</b>	<b>xv</b>
<b>1 introduction</b>	<b>1</b>
1.1 General Context . . . . .	1
1.2 Offshore Wind . . . . .	2
1.3 Floating Offshore Wind . . . . .	2
1.3.1 FOWT Floater Concepts . . . . .	3
1.4 Research Motivation . . . . .	4
1.5 Research Objective . . . . .	5
1.6 Thesis Outline . . . . .	6
<b>2 Background Theory &amp; Methodology</b>	<b>7</b>
2.1 Analytical Theory . . . . .	7
2.1.1 Floating Static Stability . . . . .	7
2.1.2 Floating Dynamic Stability . . . . .	9
2.1.3 Regular Wave Theory . . . . .	12
2.2 Numerical Method Theory . . . . .	15
2.2.1 Navier-Stokes/VoF Numerical Method . . . . .	16
2.2.2 Discretization Method: Finite Volumes Method . . . . .	17
2.2.3 Solution Algorithm and Pressure-Velocity Coupling . . . . .	18
2.2.4 Waves2Foam Toolbox . . . . .	20
2.2.5 Dynamic Solver for 6-DOF Rigid Body Motions . . . . .	20
<b>3 Convergence study of a Numerical Wave Tank</b>	<b>27</b>
3.1 convergence study by grid refinement on an infinite domain . . . . .	27
3.1.1 Model Set-up . . . . .	28
3.1.2 Model Results . . . . .	29
3.2 Convergence of Key Numerical Parameters . . . . .	31
3.2.1 Expansion Ratio . . . . .	33
3.2.2 Relaxation Zones Length . . . . .	34
3.2.3 Maximum Residual in the Poisson Iterative Solution for Pressure . . . . .	35

<b>4</b>	<b>Mooring Line Model Study</b>	<b>37</b>
4.1	Mooring Line Configurations . . . . .	37
4.2	Mathematical Mooring Models Description. . . . .	38
4.2.1	LinearSpring . . . . .	38
4.2.2	waves2FoamMooring . . . . .	39
4.2.3	MoorDyn . . . . .	40
4.2.4	Moody . . . . .	41
4.3	Model Set-Up . . . . .	42
4.4	Simulation Results . . . . .	45
<b>5</b>	<b>Wind/Waves Simulation of OC4 Phase II Semi-Submersible Floater</b>	<b>51</b>
5.1	Offshore Code Comparison Collaboration . . . . .	51
5.1.1	OC4 . . . . .	52
5.1.2	OC5 . . . . .	52
5.1.3	OC6 . . . . .	53
5.2	Simulation background & motivation. . . . .	53
5.3	Model Set Up . . . . .	55
5.3.1	Mesh Convergence. . . . .	57
5.4	OC4/OC5 Free Decay Tests . . . . .	58
5.5	OC6 Free Decay Tests . . . . .	62
5.6	Effect of Aerodynamics on hydrodynamics . . . . .	64
5.6.1	Model setup and assumptions . . . . .	64
5.6.2	Results . . . . .	65
<b>6</b>	<b>Conclusions</b>	<b>77</b>
6.1	Thesis summary . . . . .	77
6.2	Answer to research question . . . . .	78
6.3	Final conclusions and further research . . . . .	81
<b>A</b>	<b>Mooring line input files</b>	<b>93</b>
<b>B</b>	<b>Additional results Chapter 4</b>	<b>99</b>
<b>C</b>	<b>Mesh convergence</b>	<b>101</b>

# LIST OF FIGURES

1.1	pre-commercial & commercial FOW projects in Europe. . . . .	3
1.2	floaters concepts for FOWT: barge, semi-submersible, spar buoy, tension leg platform, taken from [26] . . . . .	4
2.1	static equilibrium of a FOWT tilted in pitch direction due to external forces	8
2.2	Stability triangle, comparing the main stability driver component for stability for TLP spar and semi-sub floaters, taken from [4] . . . . .	9
2.3	Response Amplitude Operator in function of the excitation frequency $\omega$ , taken from [55] . . . . .	11
2.4	Frequencies and periods of the vertical motions of the ocean surface, taken from [40] . . . . .	12
2.5	Comparison of second-order third-order, fourth-order, fifth-order Stokes waves and Airy wave (linear wave theory), taken from [15]. . . . .	14
2.6	Validity of different wave theories, taken from [9] . . . . .	15
2.7	Types of numerical models applied in wave-structure interaction . . . . .	16
2.8	6 DOFs represented, with 3 translations (surge, sway, heave) and 3 rotations (roll, pitch, yaw) . . . . .	21
2.9	Dynamic Mesh Methods available in OpenFOAM environment . . . . .	22
3.1	error between wave simulated and second order stokes wave analytical solution. $\delta p$ is the phase error and $\delta a$ is the amplitude error . . . . .	27
3.2	graph plotting in logarithmic scale the relative amplitude error at the first wave gauge normalized by the wave height H for each of the 8 wave periods	30
3.3	graph plotting the amplitude error at each 400 time step of the first wave period normalized by the wave height H . . . . .	31
3.4	graph plotting in logarithmic scale the relative phase error at the position of the first wave gauge normalized by the wave height H for 7 wave periods	32
3.5	Representation of the simulated NWT . . . . .	33
3.6	Expansion ratio value effect on the accuracy of the resulting wave amplitude (left figure), and on the execution time of the simulation (right figure)	34
3.7	Relaxation zone length value effect on the accuracy of the resulting wave amplitude (left figure), and on the execution time of the simulation (right figure) . . . . .	35
3.8	Pressure maximum residual value effect on the accuracy of the resulting wave amplitude (left figure), and on the execution time of the simulation (right figure) . . . . .	36
4.1	Different line configurations (a) single-point taut mooring, (b) multi-point taut spread, (c) multi catenary, (d) lazy-S configuration. Adjusted from [19]	38

4.2	Geometry of catenary line, taken from [62]. . . . .	40
4.3	visualization of spatial discretization performed by moorDyn. $r_i$ is the position vector at each node, $l_{i+1/2}$ is the segment length between node $i$ and node $i + 1$ . Taken from [35] . . . . .	41
4.4	Top view of the numerical domain with generation, propagation, and absorption zones . . . . .	42
4.5	Side view of the numerical domain, with generation, propagation, and absorption zones . . . . .	42
4.6	Floating box dimensions . . . . .	42
4.7	initial mesh set-up for the first wave case H12T18 . . . . .	44
4.8	Comparing surge motion between experimental and SPH results with three mooring line models using Navier-Stokes/VoF waves2Foam solver. Case H12T18 . . . . .	45
4.9	Comparing heave motion between experimental and SPH results with three mooring line models using Navier-Stokes/VoF waves2Foam solver. Case H12T18 . . . . .	46
4.10	Comparing pitch rotation between experimental and SPH results with three mooring line models using Navier-Stokes/VoF waves2Foam solver. Case H12T18 . . . . .	47
4.11	Box motion using moorDyn. From top left the time screenshot is taken after 9, 13, 20 and 23 seconds. The water surface is visualized with a contour line of $\alpha_{\text{water}}$ equal to 0.5, and the color map is related to the water pressure. Case H12T18. . . . .	48
4.12	Box motion problem using waves2FoamMooring, at 9 and 20 seconds. water surface visualized with $\alpha_{\text{water}}$ equal to 0.5. . . . .	48
4.13	Tension at anchor point is shown, where line 1 is a front line, and line 3 is a back line. . . . .	49
5.1	OC4-DeepCwind floating wind system design . . . . .	54
5.2	(a) side view . . . . .	57
5.3	(b) top view . . . . .	57
5.4	Results of mesh convergence study . . . . .	58
5.5	representation of the full meshed domain with ParaView. To notice the different cell size in the FOWT boundary layer and in the free surface region . . . . .	59
5.6	Results of free decay motions in time domain in order from top left to bottom right: surge, sway, heave, pitch. . . . .	61
5.7	Damping ratios determined with the logarithmic decrement. From top left: surge, heave, pitch. . . . .	62
5.8	Comparison of free decay test in surge, heave, and pitch direction between the present OpenFOAM results, experimental results, and DNVG results using potential flow solver Bladed . . . . .	63
5.9	Thrust curve of 5MW NREL reference offshore turbine [54]. . . . .	65
5.10	Snapshot of the FOWT at $t=0.0s$ (start of the simulation) using ParaView postProcessing for case 3. Contour surface at 0.95 $\alpha_{\text{water}}$ for capturing the surface elevation. Color grid representing the fluid dynamic pressure . . . . .	66

5.11 Snapshot of the FOWT at t=40.0s using ParaView postProcessing for case 3. Contour surface at 0.95 alpha_water for capturing the surface elevation. Color grid representing the fluid dynamic pressure . . . . .	67
5.12 CASE1 surge time-domain floater displacement . . . . .	67
5.13 CASE1 heave time-domain floater displacement . . . . .	68
5.14 CASE1 pitch time-domain floater displacement . . . . .	68
5.15 CASE1 mooring tensions in kN . . . . .	69
5.16 water/air interface elevation in time. Comparison between numerical and analytical solutions . . . . .	69
5.17 CASE2 surge and pitch time-domain FOWT displacements . . . . .	70
5.18 CASE2: on the left comparison between aerodynamic and hydrodynamic forces, on the right hydrodynamic forces from reference paper CFD [91] and present OpenFOAM. . . . .	70
5.19 CASE2 comparison between viscous and pressure total forces and moments on the floater boundary. . . . .	71
5.20 In the left figure, pressure force against time in x, y, and z direction. In the right graph, pressure moment against time around x, y, and z axis. Case 2 .	71
5.21 In the left figure, viscous force against time in x, y, and z direction. In the right graph, viscous moment against time around x, y, and z axis. Case 2 .	72
5.22 CASE3 FOWT motions. Left graph surge, right graph pitch. . . . .	73
5.23 CASE3 FOWT motions extrapolation of local maxima and minima to determine motions RAOs . . . . .	74
5.24 CASE3 FOWT motion RAOs. Left graph RAOs for case1. Right graph RAOs for cases2 and 3. . . . .	74
5.25 CASE3 FOWT load RAOs. The left graph force RAOs for case1. Right graph force RAOs for cases 2 and 3. . . . .	75
5.26 CASE3 FOWT load RAOs. The left graph force RAOs Fx and Fz for cases 1, 2, and 3. Right graph moments RAOs Mx and My for cases 1, 2, and 3. . . .	75
6.1 Case 3 flow dynamic pressure at t=60.0s side view and top view. . . . .	79
6.2 Case 3 turbulent eddy viscosity at t=60.0s side view and top view. . . . .	79
A.1 MoorDyn input file: OpenFOAM case folder/Mooring . . . . .	94
A.2 Moody input file: OpenFOAM case folder/Mooring . . . . .	96
A.3 Waves2FoamMooring input file: OpenFoam case folder/constant/dynamic-MeshDict . . . . .	97
B.1 Additional result comparing heave motion between waves2FoamMooring model with adjusted length, experimental, and SPH . . . . .	99
B.2 Additional result comparing surge motion between waves2FoamMooring model with adjusted length, experimental, and SPH . . . . .	100
B.3 Additional result comparing pitch rotation between waves2FoamMooring model with adjusted length, experimental, and SPH . . . . .	100
B.4 Additional result comparing anchor tension of line 1 between waves2Foam-Mooring model with adjusted length, experimental, and SPH . . . . .	100

---

C.1	Coarse mesh, front view . . . . .	101
C.2	Coarse mesh, side view . . . . .	101
C.3	Medium-coarse mesh, front view . . . . .	102
C.4	Medium-coarse mesh, side view . . . . .	102
C.5	Medium-fine mesh, front view . . . . .	102
C.6	Medium-fine mesh, side view . . . . .	102
C.7	Fine mesh, front view . . . . .	102
C.8	Fine mesh, side view . . . . .	102

# LIST OF TABLES

3.1	parameters for numerical wave and domain setup . . . . .	28
3.2	Boundary conditions for velocity, alpha, and pressure . . . . .	29
3.3	Parameter values for the expansion ratio convergence study . . . . .	34
3.4	Parameter values for the relaxation zones length convergence study . . . . .	35
3.5	Parameter values for the maximum pressure residual for the Poisson equation convergence study . . . . .	36
4.1	Position of anchors and fairlead attachments to the floating box. Fairlead 1 and anchor 1 define mooringLine 1, fairlead 2 and anchor 2 define mooringLine 2, etc . . . . .	43
4.2	Wave conditions simulated in OpenFOAM using waves2Foam . . . . .	43
4.3	Box and mooring lines relevant parameters . . . . .	44
5.1	Platorm gross properties . . . . .	55
5.2	Turbine gross properties . . . . .	55
5.3	Mooring lines gross properties . . . . .	56
5.4	FOWT full system main properties . . . . .	56
5.5	Mesh convergence study . . . . .	58
5.6	Natural periods for 6 DOFs . . . . .	59
5.7	Initial displacement free decay tests . . . . .	59
5.8	non-linear periodic regular wave and wind field with associated thrust force analyzed cases . . . . .	64



# NOMENCLATURE

## ABBREVIATIONS

Abbreviation	Definition
USD	United States Dollar
IEA	International Energy Agency
AEY	Annual Energy Yield
YoY	Year on Year
FOW	Floating Offshore Wind
FOWT	Floating Offshore Wind Turbine
TLP	Tension Leg Platform
HPC	High Performance Computer
CFD	Computational Fluid Dynamics
NWT	Numerical Wave Tank
FEM	Finite Element Method
FSI	Fluid Structure Interaction
COG	Center of Gravity
COB	Center of Buoyancy
COF	Center of Flotation
DOF	Degree of Freedom
RAO	Response Amplitude Operator
MPM	Most Probable Maximum
BC	Boundary Condition
RANS	Raynolds Averaged Navier Stokes
LES	Large Eddy Simulation
DNS	Direct Numerical Simulation
SPH	Small Particle Hydrodynamics
NS	Navier Stokes
VoF	Volume of Fluid
FVM	Finite Volume Method
PDE	Partial Differential Equation
SIMPLE	Simple Implicit Method for Pressure Linked Equations
PISO	Pressure Implicit with Splitting Operations
PIMPLE	Pressure Implicit Method for Pressure Linked Equations
ODE	Ordinary Differential Equation
ALE	Algebraic Lagrangian Eulerian
cph	cell per wave height
CFL	Courant-Friedrichs-Lewy

Abbreviation	Definition
AE	Elastic module
E	Young's modulus
DLL	Dynamic Linked Library
NREL	National Renewable Energy Laboratory
QTF	Quadratic Transfer Function
BEM	Boundary Element Theory
CM	Center of Mass

## SYMBOLS

Symbol	Definition	Unit
$g$	Gravity	$[m/s^2]$
$M$	Moment	$[Nm]$
$F$	Force	$[N]$
$\mathbf{I}$	Inertia Tensor	$[kg \cdot m^2]$
$m$	displacement	$[m]$
$\dot{x}$	velocity	$[m/s]$
$\ddot{x}$	acceleration	$[m/s^2]$
$\mathbf{M}$	Mass matrix	$[kg]$
$\mathbf{A}$	Added mass matrix	$[kg]$
$\mathbf{B}$	Damping Matrix	$[kg/s]$
$\mathbf{C}$	Hydrostatic stiffness matrix	$[N/m]$
$\mathbf{K}$	Mooring line stiffness matrix	$[N/m]$
$T$	Wave period	$[s]$
$H$	Wave height	$[m]$
$h$	water depth	$[m]$
$k$	Wave number	$[m^{-1}]$
$\underline{u}$	Velocity field	$[m/s]$
$p$	Pressure	$[Pa]$
$p_{rgh}$	Dynamic pressure	$[N/m^2] [Pa]$
$T$	Tension	$[N]$
$\rho$	Density	$[kg/m^3]$
$\omega$	Frequency	$[rad/s]$
$\lambda$	Wavelength	$[m]$
$\nabla$	Volume of displace fluid	$[m^3]$
$\xi_a$	Wave amplitude	$[m]$
$\phi$	Velocity potential	$[-]$
$\nabla^2$	Laplacian operator	$[-]$
$\nabla \cdot$	Divergence	$[-]$
$\nabla$	Gradient	$[-]$
$\mu$	Dynamic viscosity	$[Ns/m^2]$

---

Symbol	Definition	Unit
$\alpha$	Volume fraction	[-]
$\tau$	Viscous stress tensor	[N/m <sup>2</sup> ] [Pa]
$\delta p$	Phase error	[-]
$\delta a$	Amplitude error	[-]
$\zeta$	Damping ratio	[-]
$\delta$	Logarithmic decrement	[-]

---



# 1

## INTRODUCTION

### 1.1. GENERAL CONTEXT

With energy markets remaining extremely vulnerable, 2022 energy shock is a reminder of the fragility and unsustainability of our current energy system. Prices for spot purchases of natural gas have reached levels never seen before, exceeding the equivalent of 250 USD for a barrel of oil. Coal prices have also hit record levels, while oil rose well above 100 USD per barrel. High gas and coal prices account for 90% of the upward pressure on electricity costs around the world.

Nonetheless, the modern 2022 energy crisis can represent a boost for clean technology investments and for the energy transition, as happened in the 1970s with the oil crisis. Indeed, in the most affected regions, higher shares of renewables were correlated with lower electricity prices, but these were far from being enough. As stated in the IEA World Energy Outlook 2022 [49], annual clean energy investments will rise to more than 2 trillion USD by 2030, a rise of more than 50% from today's numbers. China, United States of America and European Union represent the most affected markets, and each of them applying different strategies to tackle the energy transition.

The share of fossil fuels in the global energy mix has been stubbornly high, at around 80%, for decades. By 2030 in the STEPS scenario (Stated Policy Scenario, a more conservative benchmark for the future that does not take for granted that governments will reach all announced goals [46]), this share falls below 75%, and to just above 60% by 2050. This would be associated with a rise of around 2.5 °C in global average temperatures by 2100. This result seems far from the Paris Agreement, stipulated back in 2015, in which 196 countries agreed on limiting global warming below 1.5°C Celsius, compared to pre-industrial levels [86]. However, STEPS projection is still 1°C lower than the 2015 projection, thanks to technological gains and policy momentum toward renewables.

Electricity accounts for about 20% of the world's total final consumption of energy, but its share of energy services is higher due to its efficiency. The electricity sector accounted

for 59% of all the coal used globally in 2021, together with 34% of natural gas, 4% of oil, and nearly 52% of all renewables [67]. As it is clearly visible from these numbers, renewables will play an important role in the increasing electricity demand worldwide, and solar and wind energy will definitely be the two key players in this.

## 1.2. OFFSHORE WIND

The wind industry has seen 94 GW of new additions globally in 2021, making it the second most productive year, only 1.8% behind 2020. This new additions bring the cumulative wind capacity at 837 GW, with a 12% of year-to-year growth. Looking closely, 72.5 GW were onshore installations, while the offshore wind market enjoyed its best ever year, with 21.1 GW commissioned, bringing the total cumulative capacity to 57 GW [17]. Regarding offshore wind market, it's YoY (year-to-year) growth reaches 58% representing 7% of total global cumulative wind installations [18].

The steeper growth of offshore wind at the expense of onshore wind is mainly driven by the better environmental conditions found offshore compared to onshore. Stronger winds, with higher mean wind speed throughout the year, and more importantly, more consistent winds, which means that the turbines will be working most of the time. This reflects on a higher AEY (Annual Energy Yield) and on a higher capacity factor. According to Wind Europe [30], in 2021 Europe installed 17.4 GW of wind capacity, and 116 GW are expected to be installed between 2022 and 2026. Of these 116 GW, 27.9 GW will be located offshore, meaning that the installation rate will double from 3 GW to 5.6 GW per year.

However, all the figures mentioned above regarding offshore installations refer to fixed offshore wind turbines. Mainly monopiles, jackets, gravity-based foundations, and tripods (according to Wind Europe report of 2019 [29], 4258 monopiles, 468 jackets, 301 gravity based, and 126 tripods). Bottom-fixed turbines need relatively shallow sea water, up to 60 meters of depth, which is a critical limit for the expansion of the offshore market. Therefore, turbines need to be installed close to shore, limiting the exploitable areas available with good wind resources and having, even if limited, a visual impact on the horizon. As a consequence, to benefit from the large wind resource of the oceans with larger water depths, the only solution is to move from fixed foundations to floating structures.

## 1.3. FLOATING OFFSHORE WIND

Offshore wind's technical potential is 36 000 TWh per year for installations in water less than 60 meters deep and within 60 km from shore. Global electricity demand is currently 23 000 TWh. However, this is only true in countries where the sea doesn't become steep close to the shore. Moving further away from shore and into deeper waters, floating turbines could unlock enough potential to meet the world's total electricity demand 11 times over in 2040 [48].

The idea behind floating wind concept is fairly simple: a wind turbine tower is po-

sitioned on top of a floating structure, which is anchored to the seabed through mooring lines. The industry is adapting various floating foundation technologies (roughly 100 different designs are being explored), and some of them have already been proven in the oil and gas sector [76]. Floating Offshore Wind (FOW) holds the key to an inexhaustible resource potential in Europe, up to 80% of the total wind resource is located in waters of 60 meters or deeper [28]. Currently, there are 50+ projects (demonstrations, pre-commercial and commercial) worldwide [27]. The most important in Europe are listed below in [Figure 1.1](#)

Wind Farm Name	Country	Capacity (MW)	Commissioning date
Hywind Scotland	United Kingdom	30	2017 (in operation)
Windfloat Atlantic	Portugal	25	2019
Flocan 5 Canary	Spain	25	2020
Nautilus	Spain	5	2020
SeaTwirl S2	Sweden	1	2020
Kincardine	United Kingdom	49	2020
Forthwind Project	United Kingdom	12	2020
EFGL	France	24	2021
Groix-Belle-Ile	France	24	2021
PGL Wind Farm	France	24	2021
EolMed	France	25	2021
Katanes Floating Energy Park -Array	United Kingdom	32	2022
Hywind Tampen	Norway	88	2022

Figure 1.1: pre-commercial & commercial FOW projects in Europe.

### 1.3.1. FOWT FLOATER CONCEPTS

Out of the ~ 100 floaters being developed and studied, four designs for floating offshore wind dominate the market: barge, semi-submersible, spar buoy, and tension leg platform (TLP). The first three are loosely moored to the seabed, allowing for easier installation, while the TLP is more firmly connected to the seabed. This allows for a more stable structure [28].

- **SEMI-SUBMERSIBLE**

Is the most applied concept in the pre-commercial projects listed in [Figure 1.1](#). The stability is given by the buoyancy of the large structure made of 3/4 cylinders. Heave plates are usually placed at the bottom of the cylinders, to give some extra stability, in order to decrease the center of gravity and to decrease vertical motions. The semi-submersible floater experiences mainly large wave-induced motions, hence the tower top is moving significantly due to the large rotational motions of the base. The main advantage of this concept is that the floater is water-depth independent. Hence, since the draft of the structure is not more than a couple of meters, the semi-submersible can be assembled in a dry-dock and then towed to the specified site. However, the mooring lines tend to be catenary lines. Since they have to support high horizontal loads, they are extremely long and have a high environmental impact. Consequently, catenary mooring lines may drive up costs and complicate the installation process.

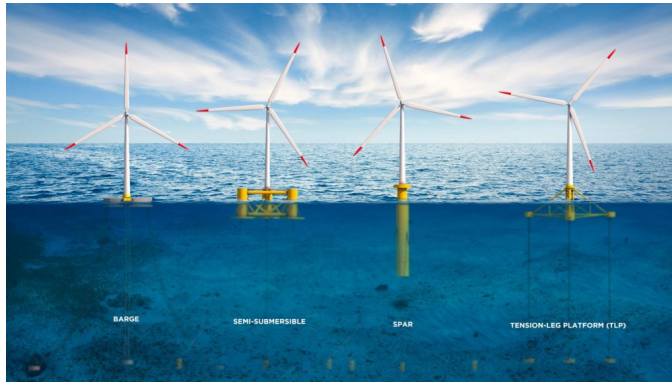


Figure 1.2: floater concepts for FOWT: barge, semi-submersible, spar buoy, tension leg platform, taken from [26]

- **SPAR-BUOY**

This concept is made of a long floating cylinder buoy, which gives floating stability by having the center of buoyancy higher than the center of gravity. This is achieved by having more mass at the bottom of the cylinder (active ballast weight). This type of structure is extremely sensitive to rotational motions, but on the other hand very stiff to translations. Compared to semi-sub, spar buoy is water depth dependent, which requires at least 100 m of depth below. The assembly can be performed both on-site or on a dry deck.

- **TENSION LEG PLATFORM (TLP)**

The main difference compared to semi-submersible and spar buoy is that this structure is not self-stable. Stability is therefore provided by the tensioned mooring lines (synthetic material), vertically anchored to the seabed. However, the advantage of the TLP concept is that it is extremely stiff to all types of motions, and it only experiences small wave induce motions. Assembly can only be done off-shore since it is not self-stable. This complicates the operations and drives up the costs. Hence, the mooring lines are typically shorter than for spar and semi-sub, however, they must carry a higher vertical load, so the material needs to be more resistant.

- **BARGE**

Barge concept, as well as semi-submersible, has a very shallow draft compared to spar buoy. The stability of such structures is ensured by their large waterplane area that provides buoyancy. The concept has been applied by the project in France named EolMed in 2021 [Figure 1.1](#). The floater, designed by Ideol, presents a very large damping pool structure, made of steel and concrete.

## 1.4. RESEARCH MOTIVATION

One of the common challenges in designing a floating offshore wind turbine (FOWT) is the ability to accurately predict critical loads due to various turbulent wind and stochastic-

wave conditions because of the complex multi-physical phenomena in realistic operating conditions. Compared with conventional onshore wind turbine or fixed-bottom wind turbine, a FOWT suffers much more complicated environmental loads: the aerodynamic forces on turbine rotor, the hydrodynamic loads on floating support platform and the mooring forces. Furthermore, the aerodynamic forces on turbine rotor are transmitted to the floating support platform via the tower, affecting the hydrodynamic responses of the platform. The mooring lines provide restoring forces to the platform by giving some additional stiffness; on the other side of the coin, the motion of the platform influence the aerodynamic performance of the turbine blades by changing the relative flow velocity and force experienced by turbine blades. Complex interaction between the components makes coupling prediction of FOWT a challenging task. Thus, careful validation of numerical analysis methods are needed to build confidence in the design process. Several intermediate-scale FOWT models have been deployed. However, all these prototypes are very expensive and complex to perform under controlled conditions. Therefore, wave basin tests for a scaled-down FOWT model are more desirable to reduce risks and costs, which allows the dynamic characteristics of a floating system to be accurately evaluated. Initially conducted by research groups, scaled-down tests range in a variety of design concepts, such as the WindFloat concept by Principle Power, Tri-Floater concept by GustoMSC, TLP concept by CEHINAV-UPM, HYWIND concept by Hydro Oil & Energy, SPAR-type FOWT concept by Yokohama National University, and three DeepCWind concepts by the University of Maine.

Although most of the previous experimental works showed interesting and practical results, these model tests have underlying limitations because they must simultaneously satisfy Froude and Reynolds' numbers scaling laws. When the Froude scaling law is applied, the Reynolds number scaling law is not guaranteed because physically impossible to achieve, and vice versa. Experimental tests of a scaled model normally cost much more than numerical analysis, and in numerical analysis, the influence of a scaled model does not need to be considered due to unlimited scale-up possibility. Therefore, improving the development and application of a high-fidelity numerical analysis method, which can fully consider the complex multi-physical phenomena due to aerohydro dynamics and multiphase fluid-structure interaction of a designed FOWT model under realistic operations, is still an important matter. Moreover, benefitting from the rapid development of high-performance computing (HPC) technique, the CFD method has shown great potential for accurate numerical simulations of FOWT.

## 1.5. RESEARCH OBJECTIVE

The aim of this research thesis is to validate the hydrodynamics of an OpenFOAM model for Floating Offshore Wind Turbines (FOWT). The main research topic is the following:

**'Validation against numerical and experimental results of a fully nonlinear Navier-Stokes/Volume-of-Fluid numerical wave tank, for the simulation of fluid-structure interaction and hydrodynamics effects of a semi-submersible floating offshore wind turbine'**

The main question is analyzed by splitting the topic in three smaller sub-questions:

1. Is it possible to reduce the computational time while keeping the accuracy of the simulations of a 2D Numerical Wave Tank (NWT) by performing convergence studies of some key numerical parameters?
2. Can a lumped-mass and FEM dynamic numerical model for mooring lines be dynamically coupled with the two-phase OpenFOAM solver for hydrodynamic simulations? How does it compare with less accurate quasi-static mooring models in terms of accuracy of results and computational time and resources?
3. How does the dynamically coupled OpenFOAM model behave when simulating full wind/wave simulations of FOWT? How do the CFD results obtained with OpenFOAM compare with experimental, high-fidelity, and mid-fidelity potential-flow solvers results?

## 1.6. THESIS OUTLINE

[chapter 2](#) presents an exhaustive summary of both the analytical and numerical theory of the physical phenomena involved in FOWT simulations. First, an overview of the physics behind rigid body dynamics and non-linear regular ocean waves is studied. Then a recap of OpenFOAM numerical theory is covered focussing on these topics: Navier-Stokes equation derivation and meaning, Finite Volume Method for spatial discretization, PIMPLE iteration for solving the pressure-velocity checkerboard problem, mesh-motions numerical equations to accomodate the body motions. Next, in [chapter 3](#) several convergence studies are performed to analyze and ultimately eliminate the influence of key numerical parameters on the simulation convergence accuracy. Following, in [chapter 4](#) an extensive comparison between quasi-static and dynamic mooring line modeling technique and their respective dynamic coupling with the OpenFOAM solver is provided. Furthermore comparing the results obtained with experimental and additional CFD results to validate the coupling. [chapter 5](#) provides the results of the dynamic wind and waves simulations of a full FOWT system: firstly focussing on the validation by free-decay tests in still water and no wind conditions, and subsequently simulating the FOWT in wave flume with a constant thrust load at hub height representing rotor aerodynamics. To conclude, [chapter 6](#) provides the reader with the key findings and some suggestions for future research.

# 2

## BACKGROUND THEORY & METHODOLOGY

The aim of this chapter is to give an overview of the analytical theory behind the simulations regarding wind and waves. In [section 2.1](#) the physical theory behind the problem of Fluid-Structure Interaction (FSI) is explained, with a focus on static and dynamic stability and waves theory. In [section 2.2](#) the numerical method applied in this work is described, focussing on the CFD OpenFOAM software, the wave generation toolbox waves2Foam, and the dynamic mesh setup.

### 2.1. ANALYTICAL THEORY

#### 2.1.1. FLOATING STATIC STABILITY

The floating stability of a static body is given by Archimedes' law: "**A body immersed in a fluid is subject to an upward vertical force equal to the weight of the liquid displaced by the body**". The mathematical form of this sentence is the following:

$$\Delta = \rho g \nabla \Rightarrow \text{weight} = \text{buoyancy} \quad (2.1)$$

where  $\Delta$  is the weight of the body,  $\rho$  is the density of the fluid,  $g$  is the gravity acceleration and  $\nabla$  is the volume of the displaced fluid by the portion of the body submerged. Until [Equation 2.1](#) is satisfied the object is floating.

As described in [Equation 2.1](#), buoyancy is the vertical up-thrust that the structure experiences due to the displacement of the fluid. This force acts in the center of buoyancy COB **B**, which is the center of mass of the displaced fluid. The center of gravity COG **G**, instead, is the point where the whole weight of the structure may be assumed to act. In ship hydromechanics is also good practice to define the rotations of the structure as heel, rotation along the longitudinal axis, and trim, rotation around the body's transverse horizontal axis. In addition, the center of floatation COF **F** is defined as the geometric centroid of the area of the waterplane, and the center of pressure of environmental forces

**CP(env)** is the point where aerodynamic, hydrodynamic and current forces act and are in equilibrium.

However, floating doesn't necessarily imply that the object is in a stable position. Indeed, when the structure is brought out of balance by an external force or moment, it will translate and/or rotate about its center of gravity. To understand if it is still in a stable equilibrium, horizontal, vertical, and rotational equilibrium needs to be addressed. In

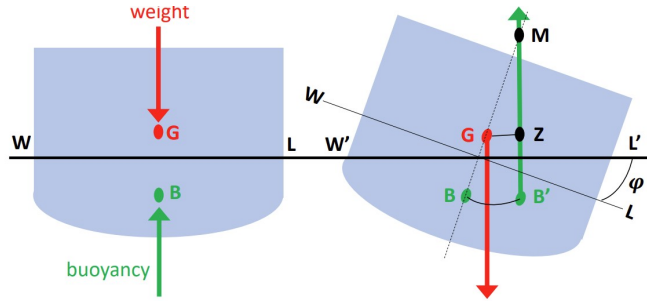


Figure 2.1: static equilibrium of a FOWT tilted in pitch direction due to external forces

order to develop a deeper understanding of the static stability of floating wind turbine systems. In a static environment, the external horizontal force/heeling moment  $M_H$  is balanced by the mooring lines of the floater. The heeling moment, or inclining moment, defined in the x-z plane, can be estimated as  $F_{env}$  multiplied by the vertical distance between CP(env) and the point where  $F_{env}$  is counteracted by the mooring line force (MLA)

$$M_H = F_{env} \cdot (z_{CP(env)} - z_{MLA}) \cos(\varphi). \quad (2.2)$$

The **vertical equilibrium** is easily satisfied by Archimedes' law since the body is in an equilibrium state. The **rotational equilibrium** is the most critical one to achieve. As visible in Figure 2.1 the shift of the center of buoyancy  $B'$  due to the external heeling moment can cause both a counter-clockwise rotation or a clock-wise rotation or righting moment  $M_R$ , depending on the draft of the structure. The first one brings the floater back to its original equilibrium position, hence is defined as a restoring moment. The righting moment moves the structure away from its original stable position, bringing the floater to a more unstable position, and enhancing the effect of the external moment. Whether the structure is going to experience a righting or restoring moment can be determined analytically by introducing the metacenter point M, visible in Figure 2.1. This fictitious point is defined by the intersection of the line defined by the two points B (center of buoyancy) and G (center of gravity) and the vertical line defined by the new buoyancy center  $B'$ .

The main difference between a ship's stability and a FOWT stability is that for a ship G is always lower than B, while for FOWT, G can be higher than B. Hence, it is common practice in FOWT hydromechanics to consider three distinct contributions to object stability: restoring moment due to **waterplane area**, restoring moment due to the **relative**

**position of B and G**, and restoring moment due to **mooring system**. The total restoring moment in pitch direction is given by the sum of all the three contributions aforementioned [4].

$$\begin{aligned}
 M_R &= M_{R,WP} + M_{R,BG} + M_{R,moor} \\
 &= \rho g I_x \frac{\sin(\varphi)}{\cos(\varphi)} + F_B z_B \sin(\varphi) - mg z_G \sin(\varphi) + C_{55,moor} \varphi
 \end{aligned}
 \tag{2.3}$$

The term  $I_x$  is the second moment of area of the initial waterplane area and  $C_{55,moor}$  is the contribution to the total stiffness by the mooring stiffness in pitch-pitch direction. Equation 2.3 can be further simplified by applying the hypothesis of small angles  $\sin(\varphi) \approx \varphi$  and  $\cos(\varphi) \approx 1$ .

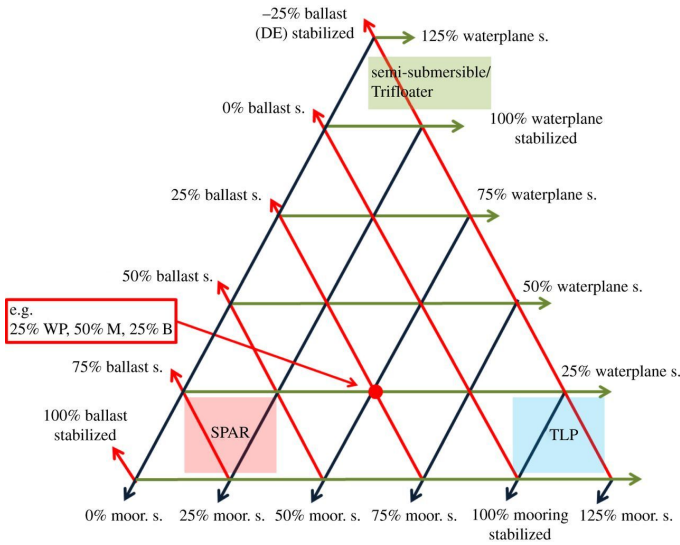


Figure 2.2: Stability triangle, comparing the main stability driver component for stability for TLP spar and semi-sub floaters, taken from [4]

Figure 2.2 is a nice summary of the hydrostatic stability comparing the main driver for static stability for the three main floater concepts, showing the percentage of each contribution to stability is shown on the sides of the triangle. Note that the ballast stabilization  $M_{R,BG}$  can also have a negative percentage influence on the overall stability. This is due to the fact that in some particular designs if the weight-to-buoyancy ratio is one, and the center of gravity G is higher than the buoyancy center B, then the contribution of the ballast is negative.

### 2.1.2. FLOATING DYNAMIC STABILITY

The main difference between floating and bottom-fixed wind turbines is the additional six Degrees of Freedom (DoFs) that the structure has. When considering the dynamics of a floating structure inside a wind and wave field, the equation of motion becomes much more complicated. In this thesis, the floater is modeled as a rigid body, so a structure

with 6 DOFs, 3 translations: **Surge**, linear motion of the structure in the longitudinal direction (along x-axis); **Sway**, linear motion of the structure in the transversal direction (along y-axis); **Heave**, linear motion of the structure in the vertical direction (along z-axis). And 3 rotations: **Roll**, angular motion of the structure around the longitudinal direction (around x-axis); **Pitch**, angular motion of the structure around the transversal direction (around y-axis); **Yaw**, angular motion of the structure around the vertical direction (around z-axis). Starting from Newton's second law of dynamics, one can write the following equation for a floating structure, for eg. in heave direction:

$$\begin{aligned} m\ddot{x}_3 &= \sum F_3 \\ &= F_{excitation} + F_{radiation} + F_{hydrostatic} \end{aligned} \quad (2.4)$$

$F_{hydrostatic}$  is the static reaction force due to the mass of fluid displaced in the motion.  $F_{radiation}$  is the dynamic reaction force, physically speaking is the force that the structure feels due to its motion.  $F_{excitation}$  is the force excitation due to incident waves. Rewriting the radiation force and the static force like  $F_{radiation} = -a_3\ddot{x} - b_3\dot{x}$ ,  $F_s = -\rho g A_{wl}x$  and replacing them into Equation 2.4, the equation of motion can be rewritten as follows:

$$(m + a_3)\ddot{x} + b_3\dot{x} + c_3x = F_{exc,3} \quad (2.5)$$

Further decomposing  $F_{exc}$  in the two components representing the undisturbed wave force (Froude-Krylov force)  $F_w$  and the force of the disturbed waves by the presence of the floating structure  $F_{diffraction}$ . By adding the mooring constraint, the equation of a moored floating rigid body, derived from the simple linear mass-spring-damper equation, can be finally written in the known form

$$(\mathbf{M} + \mathbf{A}(\omega))\ddot{\mathbf{x}} + \mathbf{B}(\omega)\dot{\mathbf{x}} + (\mathbf{C} + \mathbf{K})\mathbf{x} = \mathbf{F}_{exc}(\omega) \quad (2.6)$$

where

- **M** is the 6x6 mass matrix of the floater;
- **A** is the 6x6 added mass matrix, caused by the dynamic pressure of water that is displaced during the motion of the structure;
- **B** is the 6x6 damping matrix caused by the fluid, so it's not mechanical damping
- **C** is the 6x6 restoring matrix due to hydrostatic stiffness;
- **K** is the 6x6 restoring matrix due to the presence of mooring lines attached to the structure.
- **F<sub>exc</sub>** is the external excitation force (waves, wind, current, turbulence)
- $\omega$  is the frequency of the external force in rad/s

Equation 2.6 is a second-order linear differential equation, which has a homogeneous solution and a particular solution. The latter can be written as  $x = x_a \cos(\omega t + \varepsilon_{x,F})$  where

$x_a$  can be computed directly from Equation 2.6:  $x_a = \sqrt{\frac{F_a^2}{(-(M+A)\omega^2 + (C+K))^2 + (\omega B)^2}}$ , which can be also written as

$$\frac{x_a}{F_a} = \frac{1}{\sqrt{-(M+A)\omega^2 + (C+K))^2 + (B\omega)^2}} \quad (2.7)$$

where  $F_a$  represents the amplitude of the external force which caused the motion of the structure. Most of the time this force is a harmonic excitation force proportional to the incoming wave  $\zeta = \zeta_a e^{i\omega t}$ . Equation 2.7 represents the **Response Amplitude Operator (RAO)**, and it physically represents the relation between the amplitude of the motion and the amplitude of the force that caused the motion. The RAO is an extremely important value for the rigid body dynamic since its maximum value indicates that the structure is experiencing resonance at that certain excitation frequency, while its minimum value indicates that the floater is not responding to the motion, due to the low energy or due to the high inertia of the structure. From Figure 2.3 one can visualize the three different phases of rigid body motion. The first is when the amplitudes of the structure and the external force are equal, meaning that the rigid body equation is dominated by the restoring forces given by  $\mathbf{K}$  and  $\mathbf{C}$ . The second is the resonance area, where the frequency of the harmonic force is in phase with the one of the rigid body, leading to dangerously large motions that need to be avoided at any cost. The third happens when the frequency of the excitation force is relatively high compared to the one of the body, leading to a phase lagging in the motions due to its inertia given by the mass terms  $\mathbf{M}$  and  $\mathbf{A}$ . RAOs are ex-

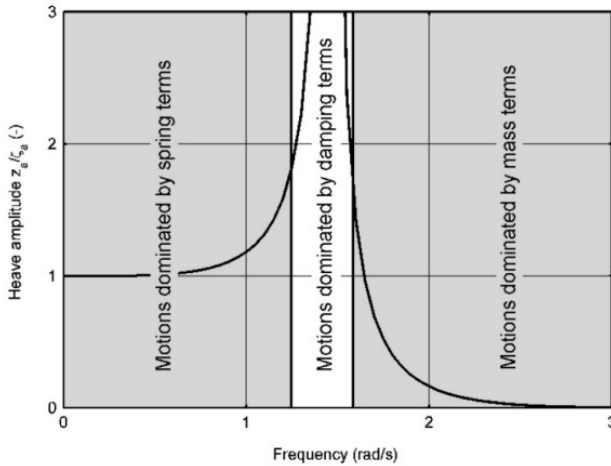


Figure 2.3: Response Amplitude Operator in function of the excitation frequency  $\omega$ , taken from [55]

remely important for the dynamic analysis of floating structures by implicitly telling the workability conditions of floating structures. Moreover, RAOs can be both motion RAOs and load RAOs, which can then give significant statistical results on the Most Probable Maximum (MPM) load that a floating structure will experience during its entire lifetime.

### 2.1.3. REGULAR WAVE THEORY

In this thesis, non-linear regular wind-generated ocean waves are considered and simulated in the numerical model. However, wind-generated gravity waves are only one type of wave. Proper classification of waves can be performed in terms of their period or frequency. From the wave energy content spectrum, [Figure 2.4](#), one can also notice that the majority of the energy of ocean waves is concentrated in the range of frequency of gravity waves, which is roughly between 1 and 25 seconds. Regular wind-generated Ocean

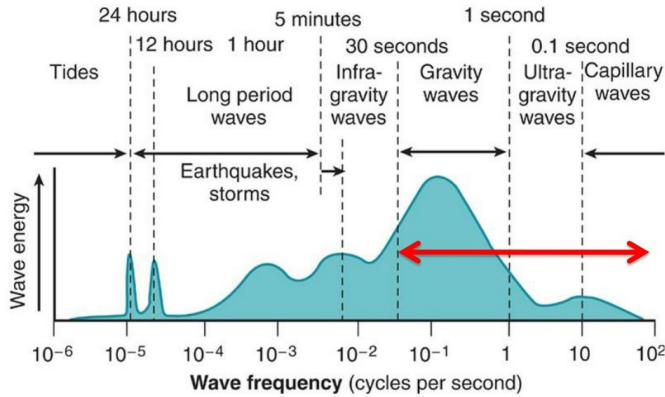


Figure 2.4: Frequencies and periods of the vertical motions of the ocean surface, taken from [\[40\]](#)

waves can be described both in a time and in a spatial domain. The main parameters that need to be known in order to describe a wave theory are the wave time period  $T$  [s], wavelength  $\lambda$  [m], wave height  $H$  [m], water depth  $h$  [m], wave frequency  $\omega$  [rad/s], wave number  $k$  [rad/m], wave amplitude  $\xi_a$  [\[56\]](#).

#### LINEAR WAVE THEORY

The Linear Wave Theory (Airy theory) is the easiest way to describe regular waves, namely ocean waves with a small amplitude compared to the wavelength [\[40\]](#). In the first-order Airy theory, water is considered to be incompressible, inviscid, and irrotational. For the latter property, a velocity potential ( $\phi$ ) exists, which satisfies the Laplacian equation ( $\nabla^2\phi = 0$ ) [\[57\]](#). It then follows the potential flow theory with three boundary conditions to be described correctly. The **kinematic bottom boundary condition**, states that the flow velocity through the sea floor must be equal to zero. The **free surface dynamic boundary condition** states that the water pressure at the free surface is equal to the atmospheric pressure. The **free surface kinematic boundary condition** states that no flow of water is allowed through the free surface. Combining the three BCs described above, the following second-order differential equation is obtained

$$\frac{\partial^2 \phi}{\partial t^2} + g \frac{\partial \phi}{\partial t} = 0 \quad (2.8)$$

and its simplest solution has the form of a progressive regular wave  $\xi(x, t) = \xi_a \cos(kx - \omega t)$ . The resulting regular wave potential function can be written as

$$\phi(x, z, t) = \xi_a \frac{g}{\omega} \frac{\cosh(k(h+z))}{\cosh(kh)} \sin(kx - \omega t) \quad (2.9)$$

Equation 2.9 is particularly important because if combined with the free surface BC, the fundamental **dispersion relation** is obtained, which correlates the wave number  $k$  (space derived parameter) with the wave frequency  $\omega$  (time derived parameter).

$$\omega^2 = kg \tanh(kh) \quad (2.10)$$

At this point, a distinction between deep and shallow waters must be done, in order to simplify the dispersion relation accordingly. Deep water waves are defined as such if the ratio between water depth and wavelength is more than 0.5, therefore seabed effects are neglected. If this is the case, then the dispersion relation is simplified to Equation 2.11.

$$\omega^2 = kg \quad (2.11)$$

While, if the ratio is  $\frac{h}{\lambda} < \frac{1}{20}$  then the waves are considered in shallow waters, and consequently the seabed effects are of importance, leading to a different form for the dispersion relation.

$$\omega = k\sqrt{gh} \quad (2.12)$$

The difference between deep and shallow water waves is also reflected in the orbital velocity of the water particles:  $u_x = \frac{\partial\phi}{\partial x}$  and  $u_y = \frac{\partial\phi}{\partial y}$ . In deep waters, the water particles move in circles in accordance with the harmonic wave. In shallow waters, the effect of the seabed changes the circular motion of the particles into an elliptic motion, until it reaches a solely horizontal motion at the sea bottom due to the large friction force.

The Airy theory is universally applicable, since in average water depths and at moderate wave heights, it gives results that are more realistic than those of higher-order theory, even for steeper waves. This is true also because the uncertainties coming from the probabilistic-statistical process in evaluating measured data are more serious than those arising from neglect of nonlinearities in wave theory [15]. However, according to [82] and [60], the linear Airy theory derived previously proves to be valid only for small values of wave amplitude. As a matter of fact, when the amplitude of a wave increases, the circular paths followed by water particles no longer remain closed. Instead, after each crest passes, the particles experience displacement from their initial positions. This phenomenon is referred to as Stokes drift. Also, the wave elevation from being a harmonic surface profile becomes a trochoid, with a limiting case becoming a cycloid. Linear wave theory serves as a first-order approximation in meeting the requirements of the free surface conditions. It is possible to enhance this theory by introducing higher-order terms consistently through the application of the Stokes expansion method.[31]. However, as the order of the Stokes wave theories increases, the associated validity is limited to deep waters applications only.

### STOKES WAVE THEORY

In the following simulation chapters (chapter 3, chapter 4, and chapter 5), **second-order Stokes waves** are chosen to be suitable for the simulations performed. In this regard, the Stokes wave theory is based on the expansion of the surface elevation in powers of the linear wave height. First-order Stokes theory is equal to Airy theory. Second-order Stokes wave theory instead differs from the linear theory for having steeper crests and wider troughs, visible in Figure 2.5. The series expansion based on the velocity potential can be performed up to the fifth order. Alternatively, the stream function can also be developed into a power series, refer to [21].

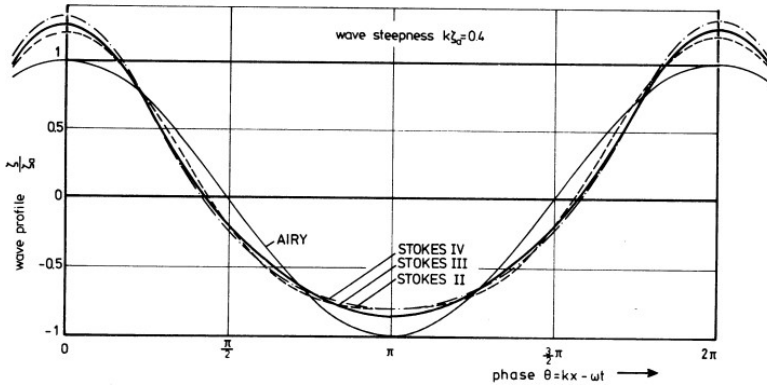


Figure 2.5: Comparison of second-order third-order, fourth-order, fifth-order Stokes waves and Airy wave (linear wave theory), taken from [15].

The surface elevation profile for a regular second-order Stokes wave is defined by:

$$\xi = \frac{H}{2} \cos(kx - \omega t) + \frac{\pi H^2}{8\lambda} \frac{\cosh(kh)}{\sinh^3(kh)} (2 + \cosh(2kh)) \cos 2(kx - \omega t) \quad (2.13)$$

Equation 2.13 in the case of deep water simplifies to:

$$\xi = \frac{H}{2} \cos(kx - \omega t) + \frac{\pi H^2}{8\lambda} \cos 2(kx - \omega t) \quad (2.14)$$

As stated before, the main difference between linear and second-order Stokes waves is the crest and trough height. In this regard, for linear wave theory, the crest wave height ratio is

$$\left( \frac{\xi_{crest}}{H} \right)_{Airy} = \frac{1}{2} + \frac{\pi H}{4\lambda} \Big|_{\frac{H}{\lambda} \rightarrow \infty} \leq 0.52 \quad (2.15a)$$

$$\left( \frac{\xi_{crest}}{H} \right)_{2^{nd}\text{-Stokes}} = \frac{1}{2} \frac{\pi H}{a\lambda} \leq 0.635 \quad (2.15b)$$

### VALIDITY RANGE OF WAVE THEORIES

According to DNV recommended practice C205 [23], to determine the validity range of a specific wave theory for a given offshore site, the regular wave parameters such as wave height and period as well as water depth are studied. Three non-dimensional parameters are defined for this purpose:  $S = \frac{H}{\lambda_0} = \mathbf{wave\ steepness}$  parameter,  $\mu = \frac{h}{\lambda_0} = \mathbf{shallow\ water}$  parameter, and  $U_R = \frac{h\lambda^2}{h^3} = \mathbf{Ursell\ number}$ . For regular steep waves, the fifth-order

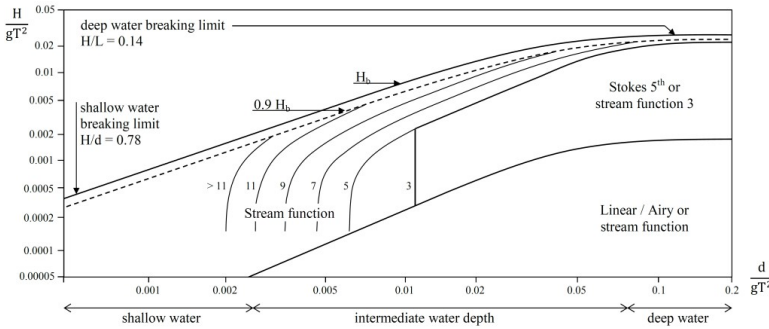


Figure 2.6: Validity of different wave theories, taken from [9]

Stokes wave theory applies. Stokes wave theory is not applicable to very shallow water. Hence, cnoidal wave theory or stream function wave theory should be used. If Ursell number is around 30, both Stokes wave theory and cnoidal wave theory have inaccuracies and the stream function method is recommended [57].

## 2.2. NUMERICAL METHOD THEORY

Traditionally the design of offshore structures has been carried out by applying semiempirical formulations, laboratory testing, and experiments. They both allow for characterizing the operability, functionality, and reliability regimes. Wave-structure interaction involves studying all the processes derived from the action of waves impacting offshore structures. Once waves reach the structure, both elements need to be studied to analyze the mutual effects. Ideally, the models should be able to reproduce as many physics aspects and as close to reality as feasible. Figure 2.7 shows the numerical methods applied until now, each of them has its own assumptions and simplifications making it suitable for some applications and unsuitable for others. The potential flow models include, among others, the Boussinesq type, the Non-Linear Shallow Water (NLSW) and the diffraction-radiation, all resolving simplified versions of the Navier–Stokes equations averaged vertically under the Eulerian (continuous fluid) hypothesis. Also called 2DH (two-dimensional horizontal plane) models due to their assumptions, they are ideal for solving diffraction, refraction, and shoaling of waves. Moreover, due to their relatively simple equations, they are particularly suitable for simulating large domains (up to kilometers) and full-time domain simulations (irregular sea states of several hours) with very low computational resources needed. However, potential flow models present limitations coming from their initial hypotheses, considering linear velocity profiles, and consequently without considering vertical components.

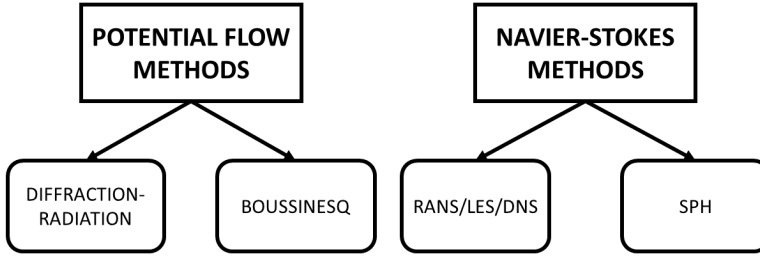


Figure 2.7: Types of numerical models applied in wave-structure interaction

Models based on the Navier–Stokes equations can be distinguished depending on how the flow is treated. If the flow is considered continuous in space the models are called **Eulerian**. On the contrary, if the flow is considered as an ensemble of different particles, this approach is called **Lagrangian**. The Smooth Particle Hydrodynamics method, or SPH, solves the Navier-Stokes equation in a discrete way, following the Lagrangian approach. This numerical model presents a few advantages compared to Eulerian methods. The first is that it does not depend on a mesh, hence eliminating every numerical error/approximation coming from it. On top of that, the solution procedure is less complex than for Eulerian models with a much higher performance. According to [1], SPH approach has two major drawbacks. Firstly, since SPH method was initially developed for astronomical applications and the predicted power spectrum is far too steep and therefore fails to resolve small-scale motions. Secondly, due to their highly compressible behavior, SPH approach needs to be reduced numerically to represent incompressible flows, which induces an artificial loss in wave height, limiting the size of the simulation domains to avoid numerical wave damping. Next, the Eulerian approach to Navier-Stokes equations is thoroughly described, which is the method implemented in OpenFOAM and used in this thesis.

### 2.2.1. NAVIER-STOKES/VOF NUMERICAL METHOD

In the following thesis, the **Navier-Stokes/VoF** method will be applied using OpenFOAM software, a CFD open-source software for the fluid-structure interaction problem [68]. This numerical method consists of an Eulerian approach to the conservation of the momentum equation. It is a method that solves highly non-linear equations, considering the fluid as a continuum. The Volume of Fluid (VoF) is a method implemented in OpenFOAM to solve multiphase flow problems.

All fluid flows are governed by mass, momentum, and energy conservation principles. In the case of ocean hydrodynamics, incompressible fluid with constant viscosity can be considered. The continuity equation for an incompressible fluid is the following:

$$\nabla \cdot \underline{u} = 0 \quad (2.16)$$

where  $\underline{u}$  is the velocity field, and  $\nabla \cdot$  is the divergence operator,  $\nabla \cdot \underline{u} = \left( \frac{\partial u_x}{\partial x} + \frac{\partial u_y}{\partial y} + \frac{\partial u_z}{\partial z} \right)$ .

The conservation of momentum, instead, is derived from Newton's second law, and considering a Newtonian fluid, the equation becomes

$$\rho \left( \frac{\partial \underline{u}}{\partial t} + \underline{u} \cdot \nabla \underline{u} \right) = \mu \nabla^2 \underline{u} - \nabla p^*. \quad (2.17)$$

In Equation 2.17  $\rho$  is the fluid density,  $\nabla = \left( \frac{\partial}{\partial x}; \frac{\partial}{\partial y}; \frac{\partial}{\partial z} \right)$  is the gradient operator, and the operation  $\underline{u} \cdot \nabla \underline{u}$  gives the directional derivative of the velocity field with respect to  $\underline{u}$ .  $\mu$  is the dynamic viscosity expressed in  $[kg/m \cdot s]$ ,  $\nabla^2$  is the Laplacian operator, which is the divergence of the gradient. In the Cartesian coordinate system, the Laplacian operator is defined as the sum of the second partial derivatives with respect to each independent variable  $\nabla \cdot \nabla \underline{u} = \left( \frac{\partial^2 \underline{u}}{\partial x^2} + \frac{\partial^2 \underline{u}}{\partial y^2} + \frac{\partial^2 \underline{u}}{\partial z^2} \right)$ . The last term is the gradient of the hydrodynamic pressure  $p^*$  defined as  $p^* = p - \rho gh$ , where  $p$  is the absolute pressure,  $g$  is the gravitational acceleration force and  $h$  is the height. Equation 2.17 is also known as the Navier-Stokes equation, and together with Equation 2.16 are the fundamental governing equations of fluid dynamics that describe the motion of fluids as a relationship between flow velocity and pressure.

To keep track of the interface between air and water, OpenFOAM uses the Volume of Fluids method (VoF), developed by Hirt and Nicholas in 1981 [38]. This type of problem in literature is referred to as multiphase problem. The free surface  $\alpha$  is specified in terms of volume fraction, in the case of water-air interface  $\alpha \in [0, 1]$  meaning that when  $\alpha = 1$  is fully water, while when  $\alpha = 0$  is fully air and everything in between is a mixture of the two phases. The local values of density  $\rho$  and of dynamic viscosity  $\mu$  are specified in terms of  $\alpha$  in the following way:

$$\rho = \alpha \rho_w + (1 - \alpha) \rho_a \quad (2.18)$$

$$\mu = \alpha \mu_w + (1 - \alpha) \mu_a. \quad (2.19)$$

Once the velocity field is resolved and known at a certain time step, the value of  $\alpha$  is updated using the conservation equation, developed by Rusche [80].

$$\frac{\partial \alpha}{\partial t} + \nabla \cdot \underline{u} \alpha + \nabla \cdot \underline{u}_r \alpha (1 - \alpha) = 0 \quad (2.20)$$

where  $u_r$  is an artificial velocity, usually called compression velocity. The boundedness of the solution, keeping the value of  $\alpha$  between 0 and 1 is guaranteed by using the MULES (MULTidimensional Limiter for Explicit Solution) in the OpenFOAM case folder.

### 2.2.2. DISCRETIZATION METHOD: FINITE VOLUMES METHOD

The Finite Volume Method (FVM) is a numerical technique that discretizes the partial differential equations PDEs form for the conservation laws (Equation 2.17, Equation 2.20, etc) over differential volumes into discrete algebraic equations over finite volumes. In a similar fashion to the finite difference or finite element method, the first step in the solution process is the discretization of the geometric domain into non-overlapping elements or finite volumes. The partial differential equations are then discretized into algebraic equations by integrating them over each discrete element. The system of algebraic

equations is then solved to compute the values of the dependent variable for each of the elements. In the finite volume method, some of the terms in the conservation equation are turned into face fluxes and evaluated at the finite volume faces. Because the flux entering a given volume is identical to that leaving the adjacent volume, the FVM is strictly conservative [66].

A simplified 1D discretization over a uniform 1D grid sequence is shown: the starting set includes the 1D momentum equation and continuity equations

$$\frac{\partial(\rho u)}{\partial x} = 0 \quad (2.21)$$

$$\frac{\partial(\rho uu)}{\partial x} = \frac{\partial}{\partial x} \left( \mu \frac{\partial u}{\partial x} \right) - \frac{\partial p}{\partial x} \quad (2.22)$$

The first step of the FVM is the integration of the momentum equation in the center  $C$  of the cell. The second step consists of using the divergence theorem (or Gauss' theorem) to transform the volume integrals of the convective and diffusive terms into surface integrals. Next, the surface integrals can be rewritten as the summation of the fluxes over the faces  $w$  and  $e$  of the cell. Using a single-point Gaussian integration method to numerically solve the surface integrals, the following momentum equation is obtained

$$\dot{m}_e u_e + \dot{m}_w u_w - \left[ \left( \mu \frac{\partial u}{\partial x} \Delta y \right)_e - \left( \mu \frac{\partial u}{\partial x} \Delta y \right)_w \right] = - \iiint_{V_c} \frac{\partial p}{\partial x} dV \quad (2.23)$$

where the subscripts  $w$  and  $e$  indicate the cell faces on the left side and on the right side respectively. If we were to discretize the Navier-Stokes equations instead of using the simplified 1D momentum equation mentioned above, the resulting equation would take the following form:

$$\mathbf{M}\mathbf{U} = -\nabla p \quad (2.24)$$

where  $\mathbf{M}$  is a matrix where all the coefficients are stored after discretizing Equation 2.17 and  $\mathbf{U}$  stores the velocity at every cell center of the mesh [74].

### 2.2.3. SOLUTION ALGORITHM AND PRESSURE-VELOCITY COUPLING

In Equation 2.24 derived before there are four unknowns ( $u_x$ ,  $u_y$ ,  $u_z$  and  $p$ ). The discretized velocity field derived from Equation 2.24 must satisfy the continuity equation, leading to a system of four unknowns and four equations. Consequently, this configuration represents a well-posed problem. In the case of a compressible flow, the four equations consist of mass conservation, momentum conservation, energy conservation, and an equation of state that establishes the relationship between pressure and temperature. In the case of an incompressible flow, the pressure ceases to be an independent variable and becomes instead determined by the Poisson equation. This equation is derived directly from the Navier-Stokes equation, accounting for the incompressibility constraint Equation 2.17.

The discretization of the pressure term can be accomplished by adopting either of the following two approaches. In the first approach, the volume integral is computed via

a single Gaussian integration point using a central difference scheme. In the second approach, the volume integral of the pressure gradient term is transformed into a surface integral using Gauss' theorem. Then by using linear interpolation for the variation of the pressure, it is possible to rewrite the surface integral as a summation of fluxes over the faces of the element. Thus either approach leads to the same expression involving the pressure difference between the alternating points E and W (cell centers of the cell on the left and on the right side). Both the velocity and the pressure values at point C depend on the values at the two alternating, not consecutive, grid points. This implies that non-physical (or checkerboard) pressure and velocity fields are seen by the Numerical scheme as uniforms [41].

There are two different ways to solve the velocity-pressure coupling problem. The first one is to use a staggered grid, in which the variables are stored in staggered grid locations such that no interpolation is needed. The second method, which is the one available in OpenFOAM, is based on the work of Patankar and Spalding [72]. They developed the **SIMPLE** (Simple Implicit Method for Pressure Linked Equations) algorithm based on the momentum predictor stage. Its main steps can be summarized as follows:

1. Start with a guessed pressure and velocity fields  $p(n)$  and  $u(n)$ , respectively.
2. Solve the momentum equation to obtain a new velocity field  $u_f^*$ .
3. Update the mass flow rates using the momentum satisfying velocity field to obtain the  $\dot{m}_f^*$  field.
4. Using the new mass flow rates solve the pressure correction equation to obtain a pressure correction field  $p'$ .
5. Update the pressure and velocity fields to obtain continuity-satisfying fields.
6. Iterate again from step 2 until convergence is reached.

In OpenFOAM, apart from the SIMPLE algorithm, the **PISO** (Pressure Implicit with Splitting Operations) and **PIMPLE** algorithm are also available. PISO is very similar to SIMPLE, the only difference is that in SIMPLE at each "outer iteration", the loop includes the momentum predictor step, and the volume fraction  $\alpha$  is recalculated, while in PISO this does not happen. PIMPLE algorithm is a hybrid version of the previous two using both the inner and outer iteration steps [69] and it is the algorithm applied in this work. The number of Outer correctors of the PIMPLE algorithm, as above mentioned, defines how many outer iterations to perform. The system will iterate until time step convergence is reached, or the max number of iterations is reached, and then move to the subsequent time step [83].

For each variable being solved by the discretized equations, a linear solver is defined. In the present cases, equations are solved for the dynamic pressure **p\_rgh**, the velocity **u**, the volume fraction  $\alpha$ , and the **cell displacement** [11]. In this work, for p\_rghFinal and for the cell displacement pcorr.\* the **Preconditioned Conjugate** solver (PCG) is used together with the preconditioner **GAMG**, as suggested in the OpenFOAM user guide and

tutorials [69]. For `p_rgh` the **GAMG** solver is applied, and finally for the volume fraction  $\alpha$  the **smoothSolver** is used in concomitance with the **symGaussSeidel** smoother.

#### 2.2.4. WAVES2FOAM TOOLBOX

In the following chapters of this thesis work, **waves2Foam** toolbox is used: developed by Niels Gjøel Jacobsen and released in 2012 [51], it enables the generation of different wave theories, together with relaxation zones. This useful toolbox was originally developed in C++ with the aim of being coupled to OpenFOAM. The wave theories already available in the toolbox are: streamline function, Stokes first-order, second-order, fifth-order, cnoidal first-order, first and second-order bichromatic waves, and first-order irregular waves with the pre-defined JONSWAP and Pierson-Moskowitz spectra. However, it is possible to couple waves2Foam to an external source that provides information on the velocity field and the surface elevation, giving the possibility to implement user-defined theories.

As previously indicated, waves2Foam facilitates the incorporation of relaxation zones within the Numerical Wave Tank (NWT), which effectively dampens wave amplitudes to prevent undesired reflections. The toolbox employs an explicit relaxation zone technique that involves a weighting scheme between the computed solution and the desired solution. The mathematical expression representing this technique is as follows:

$$\phi = (1 - \omega_R)\phi_{target} + \omega_R\phi_{computed}. \quad (2.25)$$

In Equation 2.25  $\omega_R$  is the weight and it must be bounded between 0 and 1  $\omega_R \in [0, 1]$ . As stated in the manual guide [51], this explicit method corrects the field  $\alpha$  and  $\underline{u}$  following Equation 2.25 each time step before solving the pressure-velocity coupling method. The weight factor  $\omega_R$  can be defined in multiple ways, as well as the shape and size of the relaxation zones. For the relaxation weight, effectively there are three possible ways of determining it: exponential weight (default choice), free polynomial weight, and third-order polynomial weight. In this work, the exponential weight type is used and is defined by Equation 2.26 [32]

$$\omega_R = 1 - \left( \frac{\exp \sigma^p - 1}{\exp 1 - 1} \right). \quad (2.26)$$

The exponential weight  $p$  can assume different values defined by the user, by default it has a value of 3.5.  $\sigma$  is the local coordinate inside the relaxation zone  $\sigma \in [0, 1]$  where  $\sigma = 0$  indicates the beginning of the relaxation zone while  $\sigma = 1$  indicates the end of it.

#### 2.2.5. DYNAMIC SOLVER FOR 6-DOF RIGID BODY MOTIONS

For the following study, the dynamic mesh version of the interFoam solver, developed in OpenFOAM-v2012 (interDyMFoam for previous versions), is coupled with the wave generation and absorption toolbox waves2Foam. The resulting solver is named **wavesDyM-Foam**, and its implementation was carried out successfully by following the guidelines provided in Section 5.3 of the waves2Foam manual [51].

As briefly introduced in subsection 2.1.2, the main difference between bottom-fixed and floating offshore wind turbines is the additional 6-DoFs that the latter brings. Hence,

the only possible way to numerically simulate this kind of system is to apply a dynamic mesh solver to OpenFOAM together with a rigid body solver to simulate the 6 motions. In

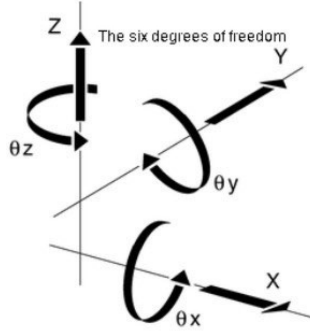


Figure 2.8: 6 DOFs represented, with 3 translations (surge, sway, heave) and 3 rotations (roll, pitch, yaw)

OpenFOAM environment, the native rigid body motion solver is the **sixDoFRigidBodyMotion**. It approximates the system of second-order differential equations derived in Equation 2.6 by numerical integration. Known as the mass-spring-damper rigid body motion equation, it is formulated based on the linear and angular momentum conservation [12]. The external forces and moments are then determined from pressure values and viscous forces calculated at the body surface at every time step, as shown below.

$$\mathbf{F} = \iint_S (p\mathbf{I} + \boldsymbol{\tau}) \cdot d\mathbf{S} + \mathbf{F}_{mooring} + m_f \mathbf{g} \quad (2.27)$$

$$\mathbf{M} = \iint_S \mathbf{r}_{cs} \times (p\mathbf{I} + \boldsymbol{\tau}) \cdot d\mathbf{S} + \mathbf{r}_{cm} \times \mathbf{F}_{mooring} + \mathbf{r}_{cg} \times m_f \mathbf{g} \quad (2.28)$$

where  $\mathbf{I}$  is the identity matrix (normal vector),  $\boldsymbol{\tau}$  is the viscous stress tensor and  $\mathbf{S}$  denotes the surface of the boundary patch for the rigid floating body.  $\mathbf{F}_{mooring}$  is the tensor for the external mooring (restraint) forces, and  $\mathbf{r}_{cm}$ ,  $\mathbf{r}_{cs}$ , and  $\mathbf{r}_{cg}$  are the arms of mooring force, hydrodynamic force, and gravity force respectively. Note that when the center of mass and the center of rotation are identical,  $\mathbf{r}_{cg} = 0$ .

Once the two external forces are calculated using the sixDoFRigidBodyMotion solver, they are incorporated into Equation 2.6. OpenFOAM is a solver that operates with a spatial discretization and computes the pressure and viscous forces at each cell center  $c$  at the interface between the rigid body and the fluid.

$$\mathbf{F}_p = \sum_c p_c S_c \mathbf{I}_c \quad (2.29)$$

$$\sum_c \mathbf{F}_v = S_c \mathbf{I}_c \boldsymbol{\tau} \quad (2.30)$$

The completed rigid-body motion equation is then solved as a second-order ODE, considering the displacement  $x$ , velocity  $\dot{x}$ , and acceleration  $\ddot{x}$  as unknowns. This equation governs the translational motion of the rigid body.

## DYNAMIC MESH

After calculating the motion of the rigid body, the next step requires updating the boundary and surrounding mesh to maintain a high-quality mesh for the subsequent time step in the solution. OpenFOAM provides various methods to incorporate a dynamic mesh into the simulation. Two fundamental types of dynamic mesh actions can be distinguished: **mesh deformation** and **topological changes** [52]. In the case of **mesh deformation**, the boundary motion is accommodated by simply moving the points that support the mesh. This approach ensures that the mesh remains continuous and does not require changes in the number of points, faces, or cells within a time step. Mesh deformation techniques introduce no additional discretization errors compared to static mesh techniques. These methods are relatively straightforward to implement and offer numerically superior results. On the other hand, **topological changes** alter the mesh structure, such as adding or removing mesh elements (points, faces, or cells) between time steps. However, these changes necessarily involve data mapping, which can introduce distribution and conservation errors. Topological changes are more complex to implement and may result in additional numerical errors compared to deforming mesh techniques.

As stated by Davidson in [20], three dynamic mesh motion techniques (DMM) can be identified in OpenFOAM environment: **mesh morphing**, **sliding interface**, and **overset** technique. On top of these three methods, according to [22], there are two more possibilities: **immersed boundary** and **topological changes methods**. All in all, Figure 2.9 summarizes all the possibilities that OpenFOAM offers to users: The algebraic mesh mo-

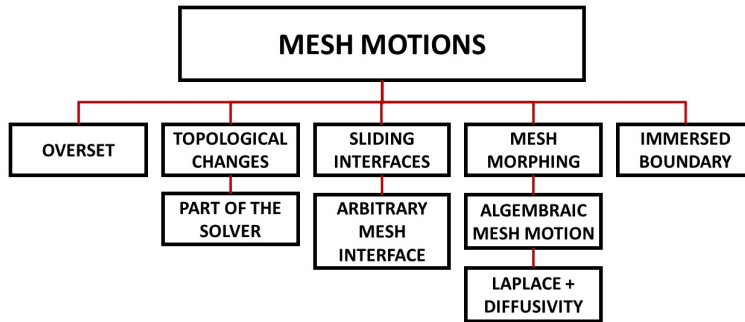


Figure 2.9: Dynamic Mesh Methods available in OpenFOAM environment

tion techniques adopt an Arbitrary Lagrangian-Eulerian (ALE) form of the conservation equations combined with a Space Conservation Law which prevents creating an extra source term and thus generating large errors. ALE necessitates an automatic mesh displacement prescription algorithm to be supplied to adapt the (fluid) velocities to the problem under consideration. In this case, a Laplacian is solved with a certain diffusivity, to accommodate the mesh deformation over a certain distance from the moving boundary [22]. The morphing mesh technique is by far the most used method in FOWT numerical studies. It falls under the category of mesh deformation without topological changes, hence a relatively straightforward method to implement. The body displace-

ment is diffused into the domain by solving the Laplacian equation:

$$\nabla \cdot (k \nabla \underline{u}) \quad (2.31)$$

where  $k$  describes the diffusivity and  $\underline{u}$  the velocity of the moving boundary. The displacement of the body leads to a deformation of single control volumes, while the total volume of all control volumes in the domain remains constant throughout the simulation. In OpenFOAM environment, distance-based diffusivity is employed, with user-specified inner and outer distance, between which mesh deformation is allowed and prohibited elsewhere.

OpenFOAM implementation of moving mesh solver can be tricky. In this thesis, the **mesh morphing** technique is applied, which is the simplest type of mesh motion. The dynamicFvMesh library was used, together with the dynamicMotionSolverFvMesh solver for mesh motion. This solver is used in cases where the motion of internal mesh points is solved using boundary conditions and diffusivity models. Few changes are required to successfully allow the mesh to enable motions. First, the boundary type for the floating object should be set as "patch" in blockMeshDict directory. Then, a dynamicMeshDict file needs to be added in the "constant" folder, where several inputs needed for the moving mesh are specified: mesh manipulation dictionary **dynamicMotionSolverFvMesh**, motion solver (**rigidBodyMotion** to simulate articulated bodies or **sixDoFRigidBodyMotion**), classes, diffusivity (quality-based or distance-based), and coefficients. In the case of the dynamicMotionSolverFvMesh, a choice between **DisplacementLaplacian** and **sixDoFMotionSolver** solvers is needed for resolving the Laplacian equation with diffusivity, Equation 2.31. Extra care must be given to the choice of the diffusivity model. This model implies a redistribution of the boundary motions through the mesh volume, and can consequently influence the correct or incorrect convergence of the solution. The mesh motion can indeed deform the mesh and create skewed cells, which could then make the domain mesh non-uniform and non-smooth and ultimately increasing the required computational time, [33].

### MOORING LINE RESTRAINTS

A wide variety of platform and mooring concepts exist for floating wind turbines, previously described in chapter 1. In addition to the general description of the different FOWT topologies, Figure 2.2 is a great representation of the stability requirements for different floater concepts applied to floating wind. Combining the two, it results that in floating offshore structures, mooring modeling plays an essential role in predicting the global response of the platform and predicting the global restoring forces. Moreover, since mooring systems are sized based on the extreme and fatigue loadings expected over their lifetime, accurate prediction of the MPM load is of obvious interest [37]. Traditionally mathematical models of mooring lines can be split into 4 main categories.

**Static Model** considers constant loads only, such as gravity, buoyancy, non-time varying current and wind, and mean wave-drift forces. Static analysis determines the equilibrium between the constant or mean environmental loads and the restoring force of the mooring lines.

**Quasi-Static Model** approach assumes that the motion of the system is uniform and linear between two static positions during a given time step for which the loads on the systems are assumed constant. Quasi-static models derive the mooring line shape and tension from the catenary formulations, based on the assumptions that the line is in static equilibrium in each time step, that the inertia effects can be neglected and that the line profile is reasonably well described by the catenary equations. However, as the name quasi-steady implies, these models do not consider in their formulation the motion dependency of mass, damping, and fluid acceleration on the system. Hence, the main disadvantage of quasi-static models is that they neglect hydrodynamic and inertial forces on the line, which can affect the structural response and are especially important for predicting the mooring loads [19]. Often, indeed, the primary effect of the mooring line dynamics on the overall system is an increase in the stiffness on the platform, which benefits platform stability. For that reason, it has been argued that using a quasi-static model over-predicts the stabilizing effect of the mooring lines and is therefore a conservative modelling approach. On the other hand, these approaches have the advantage of computational efficiency, which is desirable since the structural, hydrodynamic and aerodynamic models also tend to run quickly. For cases where waves are small, and support platform and mooring line velocities are minimal, quasi-static models can provide a good approximation to the true system dynamics [36].

**Dynamic Models** are the most accurate one and are described by Newton's second law. The main advantage of this approach compared to the previous ones is that it can accurately predict mooring tensions and loads, and also the so-called snapped loads, which are extreme loads given by the additional inertia and hydrodynamic loads. However, solving the system might be complicated, since it involves either linearising the model or employing numerical techniques to approximate the governing nonlinear differential equations. The numerical approximations are obtained via a spatial discretization of the mooring line to form a set of ODEs, which are then discretized in time and solved by an integration algorithm. Dynamic models are classified depending on which spatial discretization is employed: lumped-mass, finite difference (FDM), and finite element (FEM). The lumped mass method involves lumping all the effects of mass, external forces, and internal reactions at a finite number of nodes,  $N$ , along the line. This procedure implies that the behavior of the continuous line is modeled as a set of concentrated masses connected by massless springs. The finite difference approach differs from lumped mass methods by using an infinitesimally small differential element, rather than a finite discrete element. Forward, backward, or centered finite difference methods can be applied respectively. Lastly, FEM also discretizes the mooring line into small differential elements; however, while the finite differences method uses the differential form of the governing equations, the FEM uses its integral counterpart form [70].

For simulating floating offshore wind turbines, several studies have been conducted to show the difference between using a quasi-steady mooring model or a FEM one. Matha et al. in [65] compared the motions and loads of OC3-Hywind design using a quasi-steady and a FEM model. The outcome showed that the dynamic model predicts reduced platform motions and much larger mooring line fatigue loads than a quasi-static

model. Masciola et al. in 2013 [64] and Hall et al. in 2014 [36] drew the same conclusions that Matha et al. reached in 2011. By analyzing the response of DeepCwind and the other 3 designs respectively by using quasi-steady and dynamic mooring lines modeling, they noticed that mooring dynamics have an influence on platform motions only when those motions are large, and also that mooring dynamic response is always important for the prediction of mooring line loads. In conclusion from these studies, for a platform with small motion response a CFD software coupled with a quasi-static mooring model correctly predicts the motions of the structure, but not the mooring loads. While, for a platform with high motion response, a dynamic mooring model is needed.



# 3

## CONVERGENCE STUDY OF A NUMERICAL WAVE TANK

### 3.1. CONVERGENCE STUDY BY GRID REFINEMENT ON AN INFINITE DOMAIN

In this section the convergence of a 2D rectangular numerical wave tank is analysed. In this regard, the ability of the Navier-Stokes/VOF fluid solver is studied with the simulation of second-order Stokes waves. Following the work of [3], and [74], the main focus of this study is on the relative phase and amplitude error of the simulated second-order Stokes waves compared to the analytical solution. This is shown below in Figure 3.1 where the phase error is denoted with  $\delta p$  and the amplitude error with  $\delta a$ .

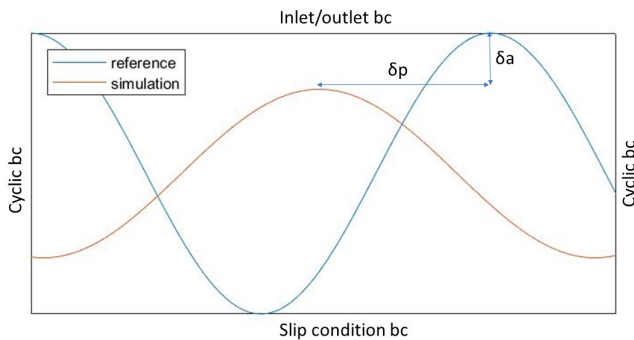


Figure 3.1: error between wave simulated and second order stokes wave analytical solution.  $\delta p$  is the phase error and  $\delta a$  is the amplitude error

### 3.1.1. MODEL SET-UP

The scope of the section is to create the most simple numerical set-up, so that the least amount of parameters can influence the surface elevation besides the mesh size. Hence, the numerical set-up of the simulation is a 2D rectangular box, with cyclic boundaries at the inlet and outlet, with respect to the propagation direction of the waves, from left to right. In this way, generation and dissipation relaxation zones are not needed, avoiding the effect of the length and of the damping coefficient of the relaxation zones. In addition to that, the computational time is kept as low as possible, so that more cases can be evaluated. The amplitude and the phase of the waves simulated in OpenFOAM with the Navier-Stokes/VOF solver are compared with the respective amplitude and phase of the analytical solution of the second-order Stokes waves. The length of the computational domain is exactly one wavelength, as described in the work of [3]. The water depth of the tank instead, is defined as 0.4 times the wavelength, while the height above the mean water level, to contain the simulation of the waves, is defined as 2 times the wave height. The numerical domain is discretized in space by  $n \times n$  cells, with an aspect ratio of 1 along the whole length and height of it. By changing the number of cells per wave height ( $cph$ ), the dimension of each square cell can be determined as follows:

$$\Delta = \frac{H}{cph} \quad (3.1)$$

where  $H$  is the wave height. The most relevant parameters of the numerical domain and wave setup are listed in [Table 3.1](#).

wave parameters	values
cell aspect ratio [-]	1
$cph$ [-]	5, 10, 15, 20
$\lambda$ [m]	98.6211
real time simulated [s]	64
wave steepness $H/\lambda$ [-]	0.05
relative water depth $h/\lambda$ [-]	0.2
$T$ [s]	8
number of wave gauges [-]	200

Table 3.1: parameters for numerical wave and domain setup

After having established the geometrical parameters of the simulation (which are mainly the input inside the constant folder in the OpenFOAM case), the computational parameters are discussed below (input parameters in the system folder). First, the timestep of the simulation, which is a critical value for having a stable simulation, was chosen to be dependent on the maximum Courant number of 0.2. The choice was mainly driven by the fact of having a fast convergence, but also stable solution. In this regard, the Courant-Friedrichs-Lewy number is defined as

$$CFL = \Delta t \frac{U}{\Delta x}. \quad (3.2)$$

This non-dimensional number has two constraints that must be fulfilled throughout the whole simulation: (1)  $CFL > 0$  and (2)  $CFL < CFL_{max}$ . Consequently, the maximum

achievable time step becomes equal to

$$\Delta t \leq 0.2 \frac{\Delta x}{U}, \quad (3.3)$$

where  $U$  is the local flow velocity and  $\Delta x$  is the local mesh size. Indeed, the time step and the simulation convergence become dependent on the mesh quality and the fluid speed. If  $\Delta x \rightarrow 0$  then the time step will also decrease  $\Delta t \rightarrow 0$ , as well as if  $U \rightarrow +\infty$  then again  $\Delta x \rightarrow 0$ . Important to note is that if  $\Delta t$  becomes too small or too large, then the simulation either crashes or gives an unrealistic divergent solution. The time scheme chosen to solve the first-order partial derivative  $\frac{\partial}{\partial t}$  is the Euler scheme, which is an implicit first-order time scheme:

$$\frac{\partial(\phi)}{\partial t} = \frac{\phi - \phi^0}{\Delta t}. \quad (3.4)$$

Finally, the boundary conditions chosen are summarized in [Table 3.2](#).

	<b>alpha</b>	<b>pressure</b>	<b>velocity</b>
<b>bottom</b>	slip	slip	slip
<b>atmosphere</b>	inlet/outlet	totalPressure	zeroGradient
<b>inlet</b>	cyclic	cyclic	cyclic
<b>outlet</b>	cyclic	cyclic	cyclic
<b>sides</b>	empty (2D)	empty (2D)	empty (2D)

Table 3.2: Boundary conditions for velocity, alpha, and pressure

### 3.1.2. MODEL RESULTS

In the NWT 200 wave gauges have been positioned to determine in each location the exact surface elevation. The **amplitude error** has been determined at the first wave gauge, so at the beginning of the NWT, and the relative amplitude error is determined using the following equation:

$$\delta\mu = \sqrt{\langle(\mu')^2\rangle} \quad (3.5)$$

where  $\langle\mu'\rangle$  is the mean of the difference between the numerically computed surface elevation and the value obtained analytically. [Figure 3.2](#) shows the amplitude error normalized by the wave height value on the y-axis, and on the x-axis, the time normalized by the wave period. After the 5th wave period, so after 40 seconds of simulation, the solution has reached convergence. As expected, the simulation with 5 cph (blue line) is the one with the highest relative amplitude error with a converged value of 0.0101. The error significantly drops with 10 cph (orange line) reaching a converged value of 0.0041. For the last two simulations of 15 and 20 cph (yellow and purple lines) the solution is more accurate compared to the 10 cph, however, between the two there is a minor difference, which does not justify the increase in computational time. More precisely for 15 and 20 cph, the converged amplitude error stabilizes at a value of respectively 0.0014 and 0.0011.

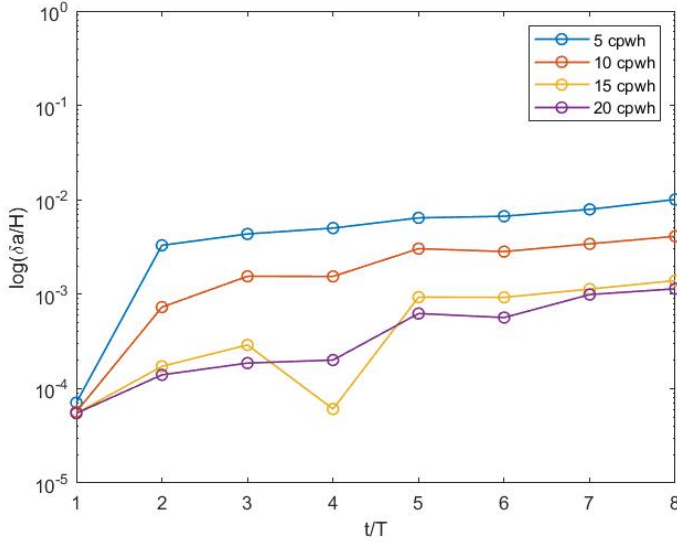


Figure 3.2: graph plotting in logarithmic scale the relative amplitude error at the first wave gauge normalized by the wave height  $H$  for each of the 8 wave periods

The second result obtained is the **phase error**. The phase error is determined at the position of the first wave gauge in accordance with the previously determined amplitude error, and again by Equation 3.5. This time, however, the phase difference is calculated over 400 time samples, which is the mean number of samples per period ( $3200/8$ ). This is performed because the phase difference at the peak of each wave period is the same, no matter how many cells per wave height are chosen. The reason for this problem lies in the fact that the phase error is smaller than the  $\Delta t$  of the simulation, hence it results zero at each wave period. For this reason, a Matlab function is created to sample and discretize the signal, and the resulting phase difference between the analytical and numerical solutions over the 400 samples shown in Figure 3.3. Important to note that in Figure 3.3 the x-axis just represents a nondimensional value of 400-time samples per wave period normalized by 8 seconds. Moreover, the negative starting and ending values for  $\delta p/H$  indicate that the numerical solution is lagging behind, while the positive values between 3 and 6.5  $t/T$  indicate that the numerical surface elevation is leading over the analytical one.

It is possible to recreate a similar plot for the phase error as the one presented in Figure 3.2. This is done by first splitting the signal into 8 periods and excluding the first one for transient purposes. Then interpolating the data points for each period in order to have 400 data points for each of them. After that, the phase average of the signal is determined by summing the phase of each period and dividing it by the total number of periods considered for averaging. At this point Equation 3.5 is used to determine the relative phase error between numerical and analytical solution, and the average of the

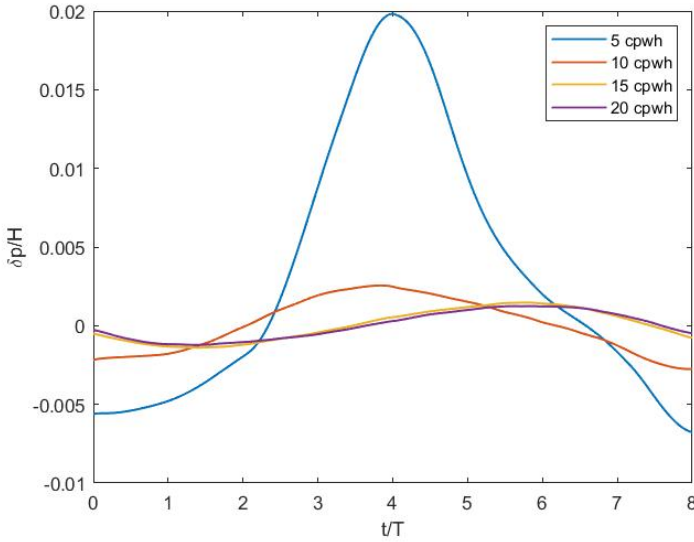


Figure 3.3: graph plotting the amplitude error at each 400 time step of the first wave period normalized by the wave height  $H$

400 errors is plotted in Figure 3.4.

In concordance with the analysis of the amplitude error, 15 cph simulation results as the most accurate one. Once again, the difference between 15 and 20 cph in both Figure 3.3 and Figure 3.4 is negligible. In the semilogarithmic graph, represented in Figure 3.4, the converged phase error value for 15 and 20 cph, respectively corresponds to 0.0015 and 0.0012. While for 5 and 10 cph, the corresponding values are 0.0198 and 0.0026. Similar conclusions are easily obtained by analyzing Figure 3.3. In this regard, the maximum absolute difference between the relative maximum and minimum phase difference for 5,10,15, and 20 cph are respectively 0.0266, 0.0053, 0.0025, and 0.0023.

In conclusion, the choice of 10 cells per wave height seems the most suitable choice considering both accuracy of the results and the required computational time and resources. However, the choice of points per wave height is a parameter that greatly influences the solution. For this reason, each particular simulation requires a grid convergence study on its own, and consequently, a fixed value of 10 cph must be taken consciously.

### 3.2. CONVERGENCE OF KEY NUMERICAL PARAMETERS

In this section, convergence analysis of key parameters for the modeling of the wave propagation in the NWT is presented. After finalizing the mesh convergence in section 3.1, the next step is the convergence study of other simulation input parameters.

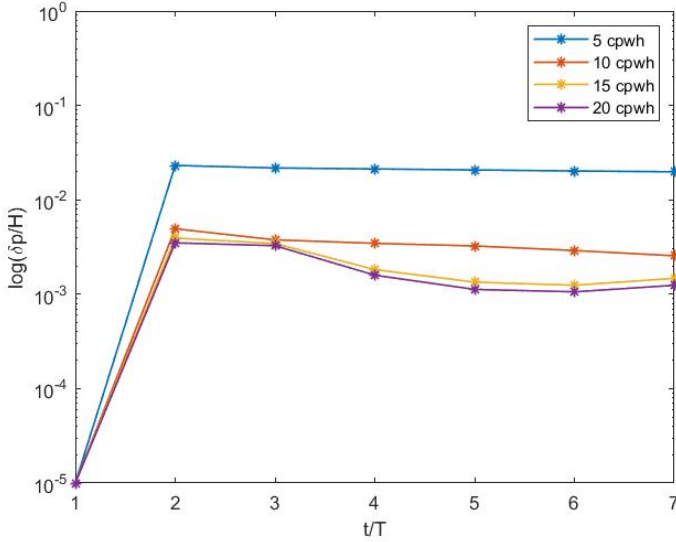


Figure 3.4: graph plotting in logarithmic scale the relative phase error at the position of the first wave gauge normalized by the wave height  $H$  for 7 wave periods

Following the work of [74] and [89], 3 parameters are studied: **relaxation zones cells expansion ratio**, **inlet/outlet relaxation length**, and **maximum residual in the Poisson iterative solution for pressure**. These values were chosen after carefully analyzing the most influential ones, both for time and results accuracy constraints.

For each parameter, two graphs are presented. The first one shows the amplitude of the simulated wave compared to the analytical wave amplitude of the reference wave. The amplitude value is measured at wave gauge number 250 (in the middle of the propagation zone, where the floating structure would be placed), and the error is averaged over all 8 simulated wave periods. The second plot, instead, shows the execution time needed against the parameters simulated. In this regard, for each of the simulations, only the time needed to run the solver **waveFoam** is compared between the various parameters, the meshing time and reconstruction time are not taken into account. Moreover, for consistency, 1 node with 16 processors on the HPC has been used to simulate the convergence of all the 4 aforementioned parameters.

The wave conditions simulated are the same as the ones described in [section 3.1](#) for consistency, the only difference is in the number of wave gauges applied in the wave tank, from 200 to 500. In this convergence study, compared to what was performed in [section 3.1](#), the NWT is a waveFlume. This means that the periodic boundary conditions at the inlet/outlet of the tank are replaced with relaxation zones. These relaxation zones are responsible for damping the waves to avoid reflection at the inlet/outlet. The inlet relaxation is called the generation zone, while the outlet one is called the absorption zone.

As shown in Figure 3.5, and theoretically introduced in subsection 2.2.4, the relaxation

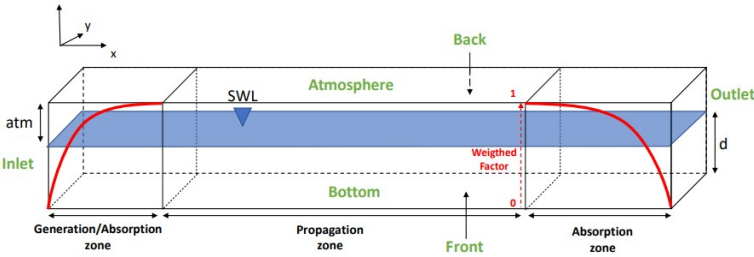


Figure 3.5: Representation of the simulated NWT

zones are characterized by a length, and by a relaxation coefficient (or damping coefficient). The damping coefficient  $p$  is a user-defined input, which influences the weight  $\omega_R$ , represented in Figure 3.5 by the red exponential red line. The zone between the generation and absorption region is called the propagation zone. In the following convergence study, the length of the propagation zone is twice the wavelength, so 197.2422 meters. The water depth and atmosphere height above SWL are determined by the values in Table 3.1. Respectively they assume the following values: 39.4484 meters and 9.8612 meters (2 times the wave height).

### 3.2.1. EXPANSION RATIO

The expansion ratio enables to decrease the total number of cells for the simulation. However, the risk of introducing an expansion ratio at the generation and absorption zones is to reduce the accuracy of the wave amplitude and phase, and, consequently reducing the overall simulation results reliability. This convergence study aims to find a reference value (or range of values) for the inlet and outlet expansion ratios which decreases the number of cells and also the computational time but at the same time does not affect the quality of the results. 5 values of the expansion ratio are examined, together with preliminary values of the other 3 key parameters, shown in Table 3.3. The initial values for the other 3 parameters are taken from reference, hence they should not influence the convergence study. Moreover, the value of the expansion ratio is considered to be the same for both the generation and absorption zone lengths, even though they could have different lengths and impact on the results. The value shown in Table 3.3 is, for reference, in concordance with the generation zone, since the cells decrease in their size by a value of 0.5 from left to right. For the absorption zone is the opposite, so the cells grow in size by 2 times from left to right.

Figure 3.6 shows that the more the cells are expanded in the relaxation zones, the worse the accuracy of the results becomes. At a value of 0.5, the ratio between simulated wave amplitude and analytical wave amplitude assumes the worse value of 0.9814, while at a value of 0.1 the amplitude ratio goes up to 0.9962. Even though the error at an expansion of 0.5 is less than 2%, it is most probable that for more complicated wave-structure interaction simulations, this error would grow larger. However, the simulation time is

Case	Expansion Ratio	Generation & Absorption Length	Free Surface Refinement	Max Initial & Final Pressure Residuals
1.1	0.1	2 & 2	3	1e-5 & 1e-6
1.2	0.2	2 & 2	3	1e-5 & 1e-6
1.3	0.3	2 & 2	3	1e-5 & 1e-6
1.4	0.4	2 & 2	3	1e-5 & 1e-6
1.5	0.5	2 & 2	3	1e-5 & 1e-6

Table 3.3: Parameter values for the expansion ratio convergence study

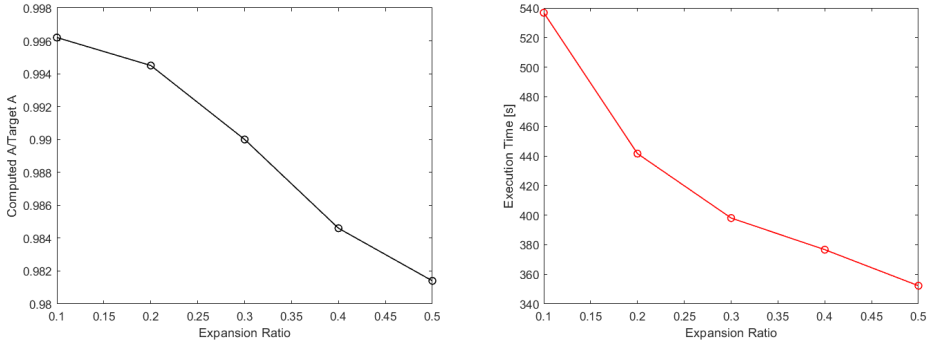


Figure 3.6: Expansion ratio value effect on the accuracy of the resulting wave amplitude (left figure), and on the execution time of the simulation (right figure)

the driving parameter for the expansion ratio choice. The execution time decreases as expected as the cell expansion ratio increases. This is because the total cell count decreases significantly when the cell size increases close to the borders of the numerical domain. The execution time goes from 536.2 seconds for 0.1, to 441.6 for 0.2 and down to 352.3 for 0.5. Hence, the time difference is quite significant, with the biggest drop of 51.6% between 0.1 and 0.2, while the steep reduction decreases to 23.6% between 0.2 and 0.3. In this thesis, a value of 0.2 is used.

### 3.2.2. RELAXATION ZONES LENGTH

The second studied parameter is the length of the two relaxation zones. As stated before, the purpose of the relaxation zones is to dampen the waves, to avoid unwanted reflection effects at the outlet boundary of the domain. For this reason, it is considered to be a critical parameter, which could easily affect the accuracy of the results. In Table 3.4 the third column shows the 5 different combinations for the generation and absorption zone lengths. The first digit is the generation length while the second is for absorption length, both are related to the wavelength. Hence, a value of 1 means that the relaxation zone is one wavelength, while 2 means it is twice the length of the waves. In the left graph of Figure 3.7 it is clear that the absorption zone length greatly influences the accuracy of the resulting wave amplitude. By looking at the values of the amplitude ratio, the 1 & 1 case is the worst with a very low result accuracy of 0.9434, together with the 2 & 1

Case	Expansion Ratio	Generation & Absorption Length	Free Surface Refinement	Max Initial & Final Pressure Residuals
2.1	0.2	1 & 1	3	1e-5 & 1e-6
2.2	0.2	2 & 1	3	1e-5 & 1e-6
2.3	0.2	1 & 2	3	1e-5 & 1e-6
2.4	0.2	2 & 2	3	1e-5 & 1e-6

Table 3.4: Parameter values for the relaxation zones length convergence study

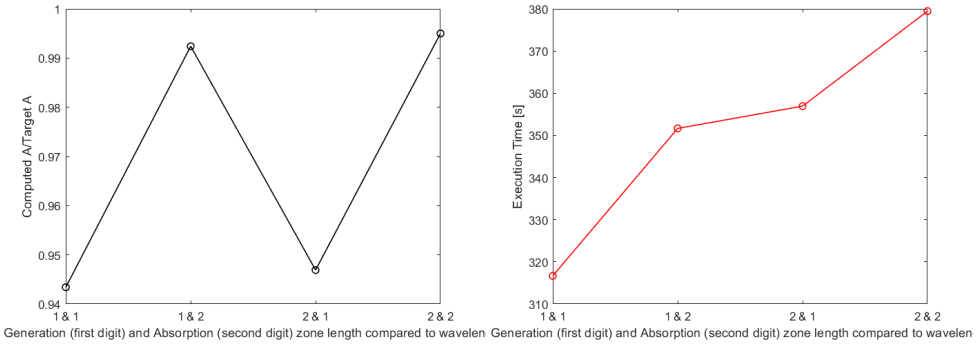


Figure 3.7: Relaxation zone length value effect on the accuracy of the resulting wave amplitude (left figure), and on the execution time of the simulation (right figure)

case of 0.9469. The reason for this high inaccuracy is the reflection of the waves at the outlet since they do not have time and space to dissipate enough. On the other hand, in the cases where the absorption zone is set to 2 times the wavelength, the precision rises up to 0.9924 and 0.995 respectively for 1 & 2 and 2 & 2. Hence, it is obvious that the absorption length should be 2 wavelengths, while the generation length impact was undoubtedly lower. The choice between 1 & 2 and 2 & 2 relies solely on the execution time difference, which was once again a significant parameter for the final choice. As a matter of fact, for 2 & 1 the time needed was slightly below 352 seconds, while for 2 & 2 was 380 seconds. As a result, case 1 & 2 is considered to be the best trade-off between affordable computational time and results reliability.

### 3.2.3. MAXIMUM RESIDUAL IN THE POISSON ITERATIVE SOLUTION FOR PRESSURE

The last studied convergence is the Poisson maximum residual for initial and final pressure values. By changing the maximum residual values it is possible to increase or decrease the accuracy of the last PIMPLE iteration. In OpenFOAM it is possible to change the residuals of other variables besides pressure, however, these are not as computationally expensive to solve as the ones of the pressure terms.

The difference of the amplitude ratio in the left plot of Figure 3.8 is almost none, therefore is a negligible parameter. On the other hand, the right plot showing the execu-

Case	Expansion Ratio	Generation & Absorption Length	Free Surface Refinement	Max Initial & Final Pressure Residuals
4.1	0.2	1 & 2	3	1e-4 & 1e-5
4.2	0.2	1 & 2	3	1e-5 & 1e-6
4.3	0.2	1 & 2	3	1e-6 & 1e-7
4.4	0.2	1 & 2	3	1e-7 & 1e-8
4.5	0.2	1 & 2	3	1e-5 & 1e-7

Table 3.5: Parameter values for the maximum pressure residual for the Poisson equation convergence study

3

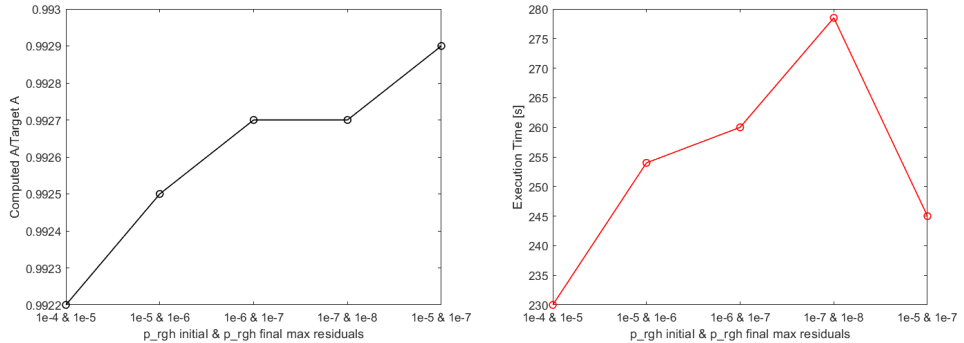


Figure 3.8: Pressure maximum residual value effect on the accuracy of the resulting wave amplitude (left figure), and on the execution time of the simulation (right figure)

tion time shows a considerable difference between the residual values. Since the accuracy of the results is almost not influenced at all by the Poisson residuals, the reference value of 1e-5 for the initial pressure maximum residual and 1e-6 for the maximum final residual are chosen to be the best values for the Poisson equation residuals.

# 4

## MOORING LINE MODEL STUDY

The aim of this chapter is to analyze the effect of different mooring line models applied to a floating structure in non-linear regular wave fields. The objective is to compare and validate the Navier-Stokes/VoF wavesDyMFoam OpenFOAM solver against experimental studies and state-of-the-art numerical models. Motions and line tensions are compared with benchmark results, to see which model is the most suitable for the aforementioned OpenFOAM solver. In total three numerical models for mooring lines **waves2FoamMooring**, **moorDyn** and **moody** are assessed and mathematically described in [section 4.2](#). Then the simulation setup is described in [section 4.3](#) and finally results are compared in [subsection 5.6.2](#).

### 4.1. MOORING LINE CONFIGURATIONS

Briefly introduced in [chapter 1](#) and in [subsection 2.2.5](#) of [chapter 2](#), the mooring line design is a crucial part of the floater type choice. The main purpose of mooring lines is the station-keeping of the floating structure and the ability to withstand a number of environmental and external forcing for a very long period of time. Especially for floating structures, mooring systems are of great importance for those three DOF motion responses (surge, sway, pitch, and yaw) where the hydrostatic restoring forces/moments are not present. Mooring lines can be classified for the material used and for the main directions of restoring forces.

At present there are three main materials that drive the mooring line manufacturing industry: chain, steel wire rope, and synthetic wire rope. Each of them is characterized by its own pros and cons. Chain is the most common component used for offshore operations. Similar to chains, also steel ropes are very durable against sea bed abrasion and saltwater corrosion [43]. On the other hand, synthetic ropes are cheaper, their price does not fluctuate in time as much as steel price, and they are durable against fatigue damage. Over the years, different types of materials have been tested, including nylon polyamide, polyester, etc. Among these, the polyester fiber rope is particularly suitable for deepwater mooring applications due to its lightweight, high strength, low elastic modulus, and

relatively low cost to manufacture. Synthetic ropes indeed, have a unique characteristic of nonlinear elastic modulus (AE) which increases with larger static load and higher cyclic loading frequencies [59].

Concerning the restoring force classification method, there are two main variations for the configuration, catenary line or taut-leg, as shown in Figure 4.1. In catenary configuration, the mooring line can be divided into two parts, the suspended line which is connected to the floating foundation, usually made out of a lighter material (nylon), and the segment that lies on the seabed, which applies horizontal loads on the anchor. Hence, a catenary line relies on the weight of chain links or clump weights to provide a horizontal restoring force to the FOWT. A taut-line system is composed of wire or synthetic ropes and is normally highly pre-tensioned. As a result, taut-line systems are usually quite stiff, both in horizontal and vertical directions, and can significantly reduce the vertical motions of the FOWT, while damping in the lines is negligible.

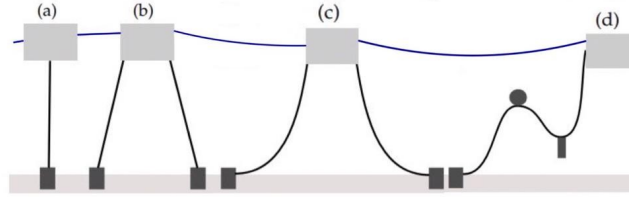


Figure 4.1: Different line configurations (a) single-point taut mooring, (b) multi-point taut spread, (c) multi catenary, (d) lazy-S configuration. Adjusted from [19]

## 4.2. MATHEMATICAL MOORING MODELS DESCRIPTION

External motion restraints such as mooring lines can be numerically coupled with OpenFOAM v2012 in the `dynamicMeshDict` file in the constant folder of the case. Inside the `dynamicMeshDict` file, the most important parameters are defined under the `sixDoFRigidBodyMotionCoeffs` (in the case where the solver `sixDoFRigidBodyMotion` was selected). Together with the parameters defining the moving body and the 6DOF solver, forces can be defined, such as constraint and restrain ones. Restraint forces indicate reaction forces given by e.g. the addition of mooring lines, while constraint forces imply that the floating object cannot move or rotate in certain directions, e.g. heave motion or pitch rotation.

### 4.2.1. LINEARSPRING

The built-in version of OpenFOAM allows the introduction of a simple spring-type mooring line model. The linear spring model, explained by Bruinsma in [7], is implemented without any damping and the input for the line are a constant stiffness  $k$  and a resting length  $l_r$ . The force that the line can exert from the floater can be defined as follows:

$$\mathbf{F} = -k \frac{\mathbf{r}}{\|\mathbf{r}\|} (\|\mathbf{r}\| - l_r) \quad (4.1)$$

where  $r$  is the distance between two connection points.

#### 4.2.2. WAVES2FOAMMOORING

A more advanced model has been developed by Jacobsen in the waves2Foam tool [51] named **waves2FoamMooring**, which enables the user to introduce catenary-type mooring lines and simple mooring lines. Even though this model is closer to reality compared to spring lines (steady-model), it is still a quasi-steady model, so no interaction between lines and fluid is detected, as well as no bending. There are three states in which the lines can be initialized: simple state, hanging state, and resting state. In the simple state, the touching point and the anchor point (where the spring is attached to an immovable object) coincide. The resting state instead is defined when the touching point and the anchor point are in two different positions. Finally, the hanging state is defined again when the anchor point and the touching point are separate, but the angle that the suspended line (between the touching point and the floater) makes with the seabed is  $\geq 88$  degrees. To implement this mooring line model in dynamicMeshDict, under restraints inside sixDoFRigidBodyMotionCoeffs, the following line has to be added: sixDoFRigidBodyMotionRestraint mooringLine. More information must be added regarding the anchors positions, fairleads positions, mass per unit length, total length of the line, nominal line diameter, and thickness (only for visualization purposes).

From the catenary configuration shown in Figure 4.2, the "catenary equations" can be retrieved (considering the catenary line inelastic  $AE = 0$ ):

$$l(x) = \frac{T_0}{P} \sinh\left(\frac{T_0}{P}x\right) \quad (4.2)$$

$$h(x) = \frac{T_0}{P} \cosh\left(\frac{T_0}{P}x\right) - \frac{T_0}{P} \quad (4.3)$$

where  $P$  is the weight per unit length and  $T_0$  is the tension at the fairlead point of the sum of all external forces (wind, current, waves). From Equation 4.2 and Equation 4.3 one can retrieve the tension along a suspended line section  $0 < l < ls$ :

$$T(l) = T_0 + Ph \quad (4.4)$$

The mooring line will exert a horizontal and vertical force,  $T_H$  and  $T_V$  respectively, on the floating structure. The larger the floating structure's offset from its equilibrium position, the larger the reaction force will be. Considering again the catenary line to be completely inelastic,  $K_{elastic} = 0$ , the geometric stiffness can be retrieved in the horizontal and vertical direction,  $K_{11}$  and  $K_{33}$  respectively. To obtain explicit expression of  $K_{11}$  and  $K_{33}$ , we need the relationship between a small change in  $dT$  resulting from small displacement change  $d\eta$  [62], [43].

$$L_T = l - ls + x = l - \sqrt{h\left(h + 2\frac{T_H}{P}\right)} + \frac{T_H}{P} \operatorname{arccosh}\left(\frac{Ph}{T_H} + 1\right) \quad (4.5)$$

Differentiating the above equation with respect to  $T_H$ , we obtain the following analytical

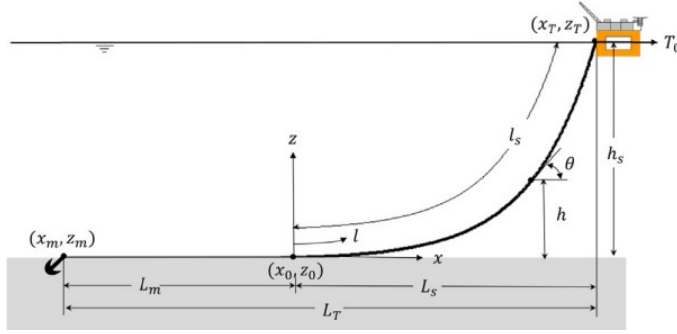


Figure 4.2: Geometry of catenary line, taken from [62].

expression of mooring line horizontal stiffness due to line overall geometric deformation:

$$K_{11} = \frac{P}{\left( \operatorname{arccosh} \left( \frac{Ph}{T_H} + 1 \right) \right) - \left( \frac{2}{\sqrt{1 + \left( 2 \frac{T_H}{Ph} \right)}} \right)} \quad (4.6)$$

The same can be repeated for the vertical direction with  $T_V(l)$  instead of  $T_H(l)$ , obtaining:

$$k_{33} = \frac{Ph + T_0}{\sqrt{h^2 + \left( 2 \left( \frac{T_0}{P} \right) h \right)}} \quad (4.7)$$

### 4.2.3. MOORDYN

An advanced dynamic mooring line model **moorDyn** has been investigated, developed, and implemented by Matthew Hall in 2017 [34]. MoorDyn is an open-source lumped-mass mooring line model that uses a second-order Runge-Kutta integration method. Described in subsection 2.2.5, lumped-mass is a type of spatial discretization of Newton's second law: the cable is broken up into  $N$  evenly-sized line segments connecting  $N+1$  node points. Each segment of the cable has identical properties of unstretched length, diameter, density, and Young's modulus. The tension due to axial stiffness is defined as follows

$$T_{i+\frac{1}{2}} = E \frac{\pi}{4} d^2 \varepsilon_{i+\frac{1}{2}} \hat{\mathbf{q}}_{i+\frac{1}{2}} \quad (4.8)$$

where  $E$  is Young's elastic modulus,  $d$  is the cable nominal diameter,  $\varepsilon$  is the strain and  $\hat{\mathbf{q}} = \frac{r_{i+1} - r_i}{|r_{i+1} - r_i|}$  is the tangent of the segment  $i + \frac{1}{2}$  connecting the nodes  $i$  and  $i + 1$ . The hydrodynamic forces, including the added mass and the cable drag, are calculated using Morrison's equation at each node  $i$ , and not at the segment centers, avoiding transverse vibrations of wavelength twice the cable length, and consequently possible instabilities [35]. First, the drag components (transverse and tangential) are defined

$$D = \frac{1}{2} \rho C_D dl |\dot{\mathbf{r}}_i \cdot \hat{\mathbf{q}}_i - \dot{\mathbf{r}}_i| ((\dot{\mathbf{r}}_i \cdot \hat{\mathbf{q}}_i) \hat{\mathbf{q}}_i - \dot{\mathbf{r}}_i) \quad (4.9)$$

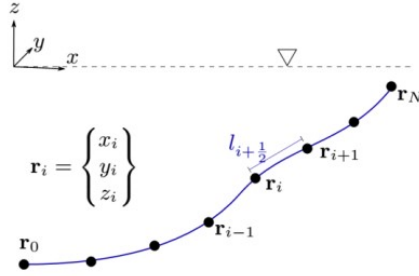


Figure 4.3: visualization of spatial discretization performed by moorDyn.  $r_i$  is the position vector at each node,  $l_{i+1/2}$  is the segment length between node  $i$  and node  $i+1$ . Taken from [35]

where  $C_D$  is the drag coefficient which assumes a different value for the transverse direction  $C_{ni}$  and for the tangential direction  $C_{ti}$ . Similarly to the drag force, the added mass can be defined in a transverse and tangential direction, which can be combined in a 3x3 matrix:

$$a_i = a_{ni} + a_{ti} = \rho \frac{\pi}{4} d^2 l [C_{ni}(\mathbf{I} - \hat{\mathbf{q}}_i \hat{\mathbf{q}}_i^T) + C_{ti}(\hat{\mathbf{q}}_i \hat{\mathbf{q}}_i^T)] \quad (4.10)$$

Combining Equation 4.9 and Equation 4.10, together with the submerged weight  $W_i$ , the complete equation of motion for each node  $i$  is

$$(m_i \mathbf{I} + \mathbf{a}_i) \ddot{\mathbf{r}}_i = \mathbf{T}_{i+\frac{1}{2}} - \mathbf{T}_{i-\frac{1}{2}} + \mathbf{C}_{i+\frac{1}{2}} - \mathbf{C}_{i-\frac{1}{2}} + \mathbf{W}_i + \mathbf{B}_i + \mathbf{D}_{ni} + \mathbf{D}_{yi} \quad (4.11)$$

where  $\mathbf{C}$  is the internal damping force in the segment and  $\mathbf{B}$  is the vertical reaction force applied to a node when it touches the ground [10]. MoorDyn model has the advantage that it includes the following parameters: axial stiffness, internal damping forces, bending stiffness, line weight, buoyancy, seabed contact, and drag and inertia forces from Morrison's equation. Since this is a dynamic model, the fluid forces (so waves and current) are implemented as well. However, torsion in the line is not taken into consideration.

#### 4.2.4. MOODY

An additional dynamic mooring model is **Moody**. Developed by Johannes Palm and Claes Eskilsson in 2017 [71], is a finite element mooring dynamics model developed with the special intent of capturing and resolving snap loads. The equation of motion for an elastic cable including the bending stiffness can be written as:

$$\gamma_0 \frac{\partial^2 \mathbf{r}}{\partial t^2} = \frac{d\mathbf{T}}{ds} + \mathbf{f} \quad (4.12)$$

where  $\gamma_0$  is the weight per unit length,  $\mathbf{f}$  is the sum of all external forces and  $\mathbf{T}$  is the axial tension, which can be defined as

$$\mathbf{T} = EA_0 \boldsymbol{\varepsilon} + \xi \dot{\boldsymbol{\varepsilon}} + \mathbf{T}_\perp \quad (4.13)$$

In Equation 4.13  $EA_0$  is the axial stiffness,  $\varepsilon$  and  $\dot{\varepsilon}$  are the strain and the strain-rate respectively,  $\xi$  is the internal damping coefficient, and  $\mathbf{T}_\perp$  is the shear force of the cable. Equation 4.12 is solved using a hp-adaptive discontinuous Galerkin method [25]. The high-order formulation makes engineering accuracy achievable using only a few high-order elements. The external forces  $\mathbf{f}$  acting on the cables include the added mass and Froude-Krylov forces, the drag force, the net force of gravity and buoyancy, and seabed contact forces. Cable bending stiffness is neglected. Compared to moorDyn, Moody's code itself is not open source, but a precompiled shared library has been provided that can be dynamically linked DLL with third-party OpenFOAM software [10].

### 4.3. MODEL SET-UP

4

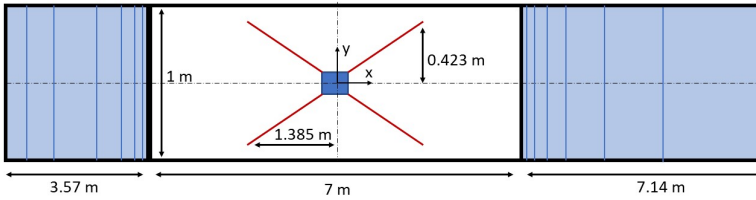


Figure 4.4: Top view of the numerical domain with generation, propagation, and absorption zones

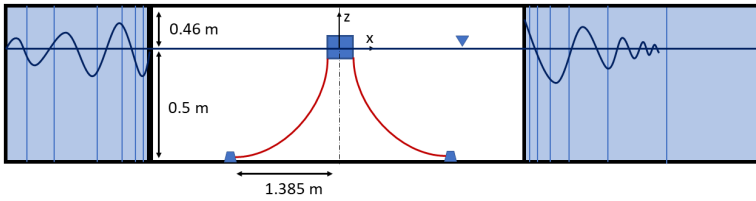


Figure 4.5: Side view of the numerical domain, with generation, propagation, and absorption zones

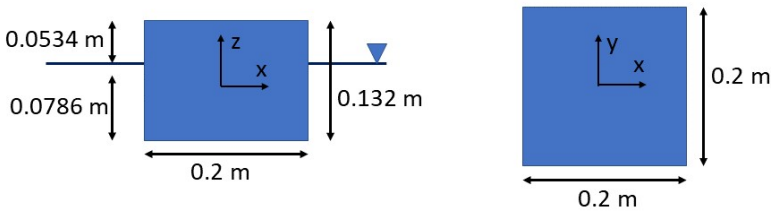


Figure 4.6: Floating box dimensions

The objective of the following model setup is to replicate the experimental results of Wu et al. in [90] and the numerical SPH approximation of the results performed by Dominguez in [24]. In the experiment, a box of dimensions  $0.2 \times 0.2 \times 0.132$ , moored to the bottom with 4 slack mooring lines, is left floating in nonlinear wave conditions in a

wave basin at Ghent University, Department of Civil Engineering. The experiments are performed in a 30.0 m long, 1.0 m wide, and 1.2 m high wave flume. OpenFOAM numerical setup dimensions of the NWT are shown in [Figure 4.4](#), and in [Figure 4.5](#). The dimensions slightly differ from the experimental setup due to a variety of reasons, but mostly due to the enormous computational cost that it would take to run the simulations with real domain lengths. In addition to that, in the experiments, the waves are generated from the right side and are absorbed at the left side. However, following the work of [24], in the CFD simulations waves travel from left to right.

The anchoring and mooring system can be visualized in [Figure 4.4](#), with the distance from the x-axis of the anchors, as well as the distance from the y-axis. The mooring line fairlead and anchor positions are listed in [Table 4.1](#). In the experiment, each slack

location	coordinates (x y z) [m]
fairlead 1	(-0.100 0.100 -0.0736)
fairlead 2	(-0.100 -0.100 -0.0736)
fairlead 3	(0.100 0.100 -0.0736)
fairlead 4	(0.100 -0.100 -0.0736)
anchor 1	(-1.385 0.423 -0.5)
anchor 2	(-1.385 -0.423 -0.5)
anchor 3	(1.385 0.423 -0.5)
anchor 4	(1.385 -0.423 -0.5)

Table 4.1: Position of anchors and fairlead attachments to the floating box. Fairlead 1 and anchor 1 define mooringLine 1, fairlead 2 and anchor 2 define mooringLine 2, etc

catenary mooring line was attached at the fairlead with an iron hook 0.005 m above the box bottom, and this is the reason why in z-direction the box bottom is at 0.0786 m below the free surface, while the fairlead points are at 0.0736 m. The input files for each of the three mooring line model is presented in [Appendix A](#). Other relevant parameters for a correct mooring line setup are derived from the work of Dominguez [24] and are listed in [Table 4.3](#). In the same table, other relevant input parameters for the floating box set up in the dynamicMeshDict directory are defined. Three fully nonlinear wave conditions are simulated in the experiment: H12T18, H12T20, and H15T18. Due to the high computational costs of the simulations, both time and memory required, only one of the three conditions is reproduced in this work: H12T18. In the waveParameters.input file needed by waves2Foam tool, the two wave cases are simulated using a second-order Stokes theory.

case	wave height [m]	wave period [s]	wave length [m]
H12T18	0.12	1.8	3.57

Table 4.2: Wave conditions simulated in OpenFOAM using waves2Foam

Following the results obtained in [chapter 3](#), the NWT mesh is divided accordingly with 10 cph (in the free surface region) and an aspect ratio of  $\sim 1$ . The cells in the

parameters	values
Cable diameter	0.003656 [m]
Cable mass per unit length	0.0607 [kg/m]
line length	1.455 [m]
Cable axial stiffness (EA)	29 [N]
Box mass	3.16 [kg]
Box second moment of inertia (Ixx Iyy Izz)	(0.015 0.015 0.021) [kg·m <sup>2</sup> ]
Box center of gravity (x y z)	(0.0000 0.000 -0.0126)

Table 4.3: Box and mooring lines relevant parameters

free surface region ( $-1.5 \cdot \text{wave height} \leq \text{free surface} \leq 1.5 \cdot \text{wave height}$ ) are refined using snappyHexMesh utility with a level 2, hence the volume is 4 times smaller than the base cells. Alongside the free surface region, also the region around the floating box is refined with level 2 close to the boundary layer and with level 1 in a broader area. The generation zone is 1 wavelength, the absorption zone is 2 wavelengths, and the propagation zone is 7 meters long (in accordance with the SPH simulation). The cell expansion ratio in the two relaxation zones is chosen to be 0.5 (2), in accordance with the convergence study performed in chapter 3. The initial mesh, after using both blockMesh for the base mesh (10 cph), and snappyHexMesh for the box creation (searchableBox function) is presented in Figure 4.7. The total number of cells after refinement adds up to a range

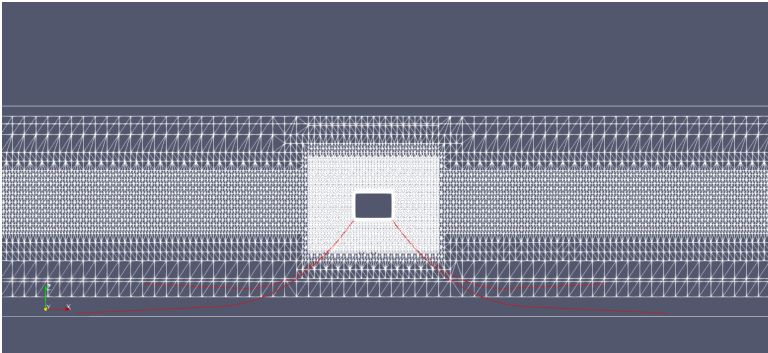


Figure 4.7: initial mesh set-up for the first wave case H12T18

of  $\sim 650k$  cells, depending on the height of the simulated waves. The solver waveDyM-Foam is used, introduced in chapter 2 (couple the wave generation toolbox waves2Foam with the interFoam OpenFOAM solver for the 6DOF motions), together with a morphing solver with dynamicMotionSolverFvMesh and sixDoFRigidBodyMotion solver. The cells are allowed to move in a region around the floater patch delimited by 0.05 and 0.35 meters. The simulation considers no turbulence effects, hence the flow is laminar, in accordance with [24]. For each of the three mooring line models studied, the simulation was performed in the HPC cluster in 1 node and subdivided with the decomposeParDict utility into 20 processors. The simulation was decided to run for 27 seconds (15 wave periods simulated).

## 4.4. SIMULATION RESULTS

Figure 4.8 and Figure 4.9 compare the linear motions in surge and heave direction. The motions of the floating box using moody, moorDyn, and waves2FoamMoorng mooring line models are validated against the experimental results obtained by Wu et al [90] and against the SPH results obtained by Dominguez in [24]. The SPH model uses a quasi-static mooring model with a piecewise extrapolating method (PEM) implemented to extrapolate the mooring forces. In addition to heave and surge linear motions, also pitch rotation is compared with benchmark results in Figure 4.10. The first thing that is

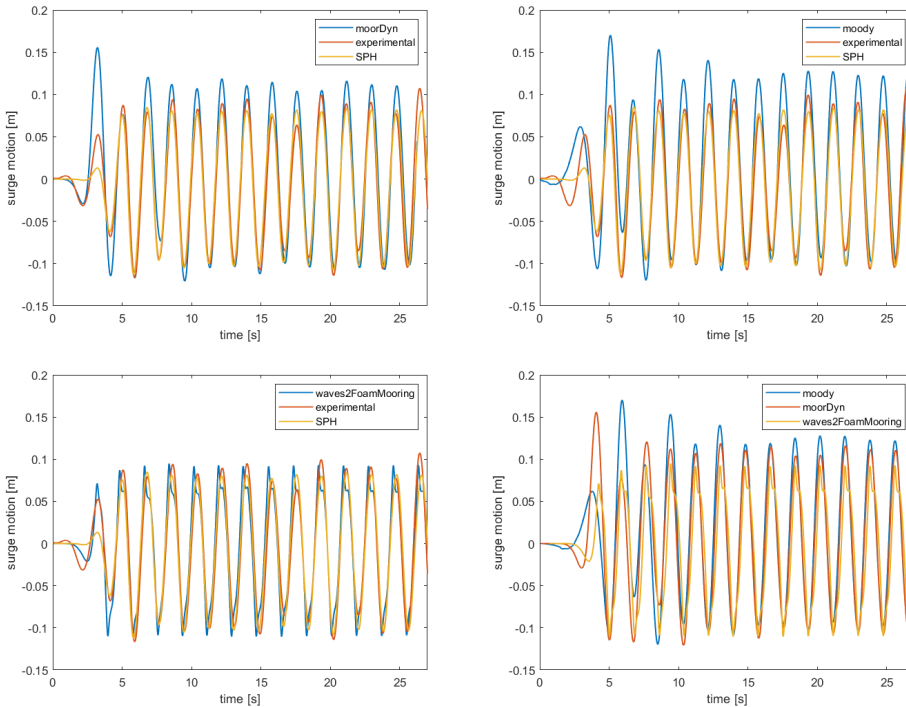


Figure 4.8: Comparing surge motion between experimental and SPH results with three mooring line models using Navier-Stokes/VoF waves2Foam solver. Case H12T18

noticed while comparing the box motions is that there is a very good concordance between the experimental results, SPH, moody, and moorDyn in heave direction. A good match is visible also in surge motion again for moody and moorDyn, even though the linear displacement is slightly overpredicted, especially during the first  $\sim 8$  wave periods, and moody is a little bit overpredicting the motion compared to moorDyn, visible in the bottom right plot of Figure 4.9. A different story is for pitch rotation, where moorDyn underpredicts the rotation amplitudes, while moody after the first  $\sim 4$  periods correctly replicate the experiment. Regarding waves2FoamMoorng quasi-steady model, a big discrepancy is found in all three displacements, especially in pitch motion. In Figure 4.10 the quasi-steady model highly overpredict the pitch rotation in such a way that

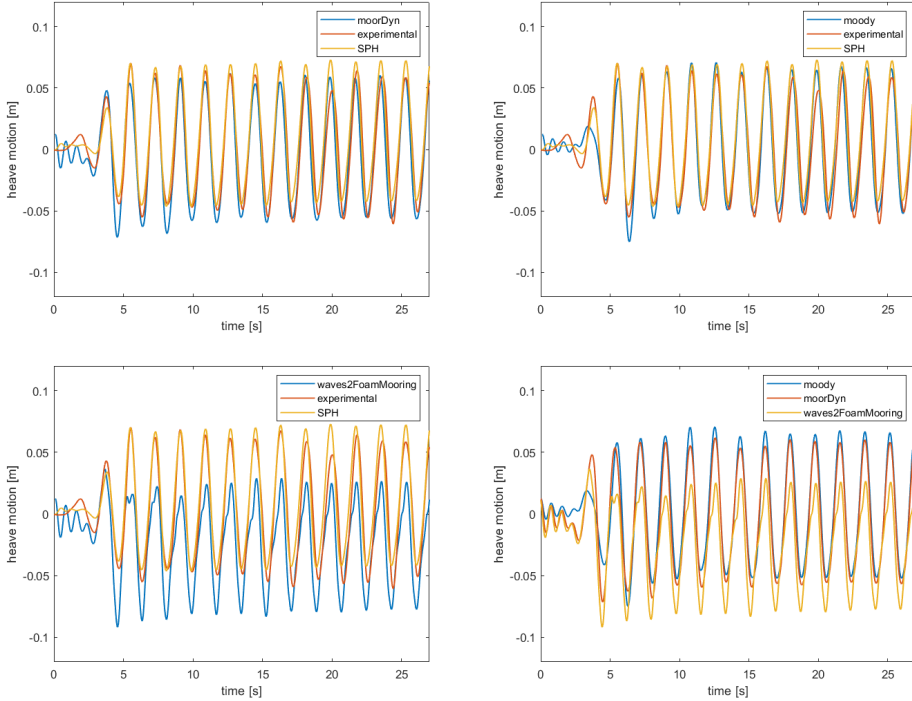


Figure 4.9: Comparing heave motion between experimental and SPH results with three mooring line models using Navier-Stokes/VoF waves2Foam solver. Case H12T18

the lines appear to be too short or too heavy for the simulation. Even though in the setup of all three mooring models, the length at rest and the mass per unit length are initialized as 1.455 meters and 0.0607 kg/m, in concordance with Table 4.1. Nonetheless, the problem is confirmed by the output file `log.waveDyMFOam` from OpenFOAM, where at the peak of surge displacement, the lines go from `restingState` to `simpleState`, meaning that the touching point coincides with the anchor point at max displacement. This problem is further confirmed by comparing the box position at times 9 and 20 seconds in Figure 4.11 and in Figure 4.12. The back and front mooring lines are respectively stretched due to the wave motion, and the box seems to be dragged under the water surface by the mooring lines in Figure 4.12 while in Figure 4.11 the floating box correctly follows the water surface. Furthermore, at the times where the heave and surge motions of waves2FoamMooring box are at a peak or thorough (which is also where it does not resemble anymore a sinusoidal shape) is also where the box sinks under the water surface of  $\alpha_{\text{water}}=0.5$ . The same discrepancy is visible in Figure 4.9, where in the bottom left plot the heave motion of the box with waves2FoamMooring is shifted below the experimental, meaning that the vertical motion is happening under the water surface.

The reason for the inaccuracy lies in the fact that waves2FoamMooring is a quasi-

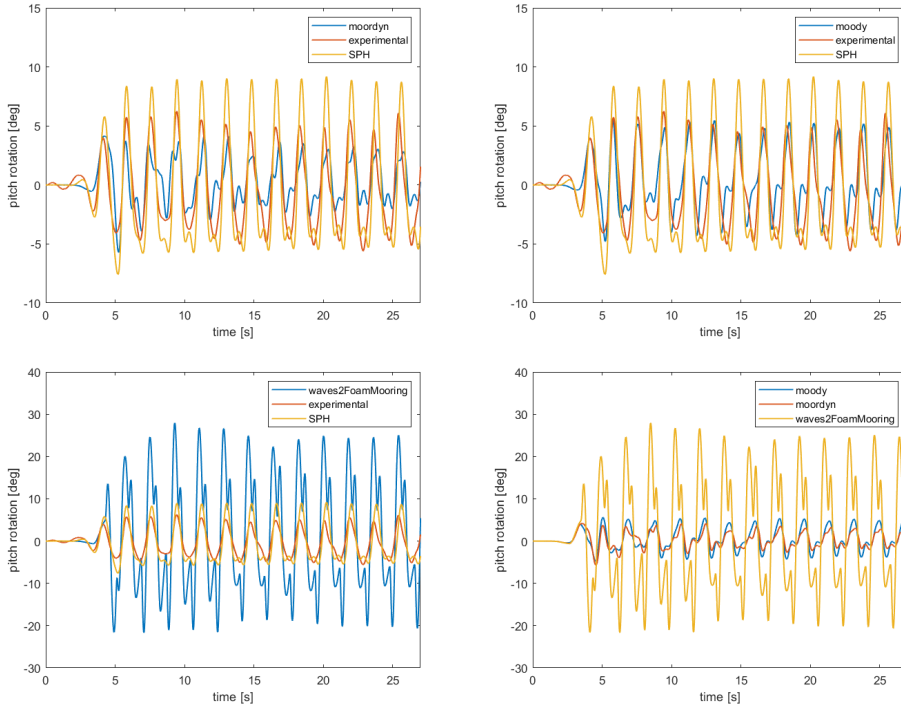


Figure 4.10: Comparing pitch rotation between experimental and SPH results with three mooring line models using Navier-Stokes/VoF waves2Foam solver. Case H12T18

steady model, and it captures neither the fluid-line interaction nor the line bending. This can lead to an unrealistic behavior of the lines, and consequently an unrealistic motion of the box, which results in a non-sinusoidal motion in heave and surge directions and in an overestimation of the pitch rotation amplitude. Another reason for the mismatch of waves2FoamMooring could be related to the fact that the available input for the lines is extremely limited compared to the two dynamic models. On top of the lineLength, anchor position and fairlead position, only the mass per unit length and the thickness can be defined. On the other hand, for moorDyn and especially moody, much more parameters defining the lines are user-defined variables, such as EA, axial and normal added mass coefficient, axial and normal drag coefficient, number of line segments, ground stiffness and damping coefficient, and the time step used in the mooring integration.

By slightly changing the lineLength input parameter for waves2FoamMooring in dynamicMeshDict, the problem previously faced is confirmed and partially solved. Indeed, if the length at rest is changed to a value of 1.6, it is clearly visible now that the floating box in heave and surge direction follows a sinusoidal motion. Obviously, the mass per unit length is changed accordingly, to keep the total mass of 0.08832 kg. Even though the results now resemble more the experimental and SPH ones, are still not enough accurate

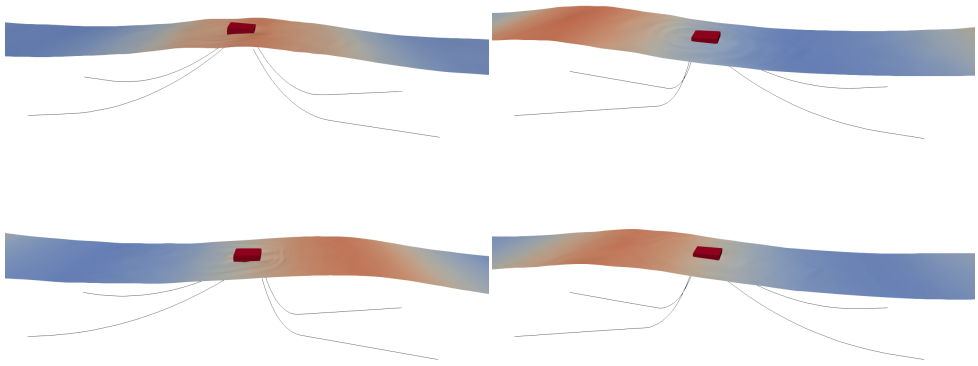


Figure 4.11: Box motion using moorDyn. From top left the time screenshot is taken after 9, 13, 20 and 23 seconds. The water surface is visualized with a contour line of  $\alpha.\text{water}$  equal to 0.5, and the color map is related to the water pressure. Case H12T18.

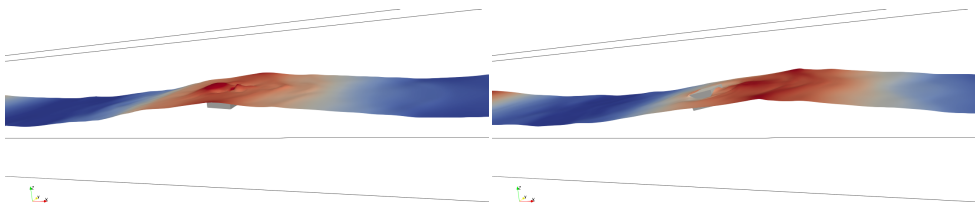


Figure 4.12: Box motion problem using waves2FoamMooring, at 9 and 20 seconds. water surface visualized with  $\alpha.\text{water}$  equal to 0.5.

compared to the ones obtained with moody and moordyn. Additional results of the adjusted line length of the quasi-steady model of surge, heave, pitch motions as well as for front and back line anchor tensions are shown in [Appendix B](#).

The next result analysed is the tension at the anchor point for the front and the back mooring lines. In the experiment, the anchor of each mooring line is connected to a loadcell fixed to the wave flume bottom. Each loadcell measures the horizontal component of the mooring-line tension ( $T$ ) and has a measurement range of 100 N and a sampling frequency of 1000 Hz. In the present study, since the lines are spatially discretized in  $N$  number of segments, the tension at the anchor point is simply the tension experienced by the first segment of each line. In [Figure 4.13](#) the anchor tension is plotted against time. While moody overpredicts the force, moorDyn perfectly matches the tension of the experiment and SPH results. The reason for moody's mismatch is that the model was intended and developed for detecting snap loads (a rapid increase in tension, which can place significant stress on the mooring line and potentially causing it to stretch, deform, or even break). As expected, the tension on the front line (line 1) is

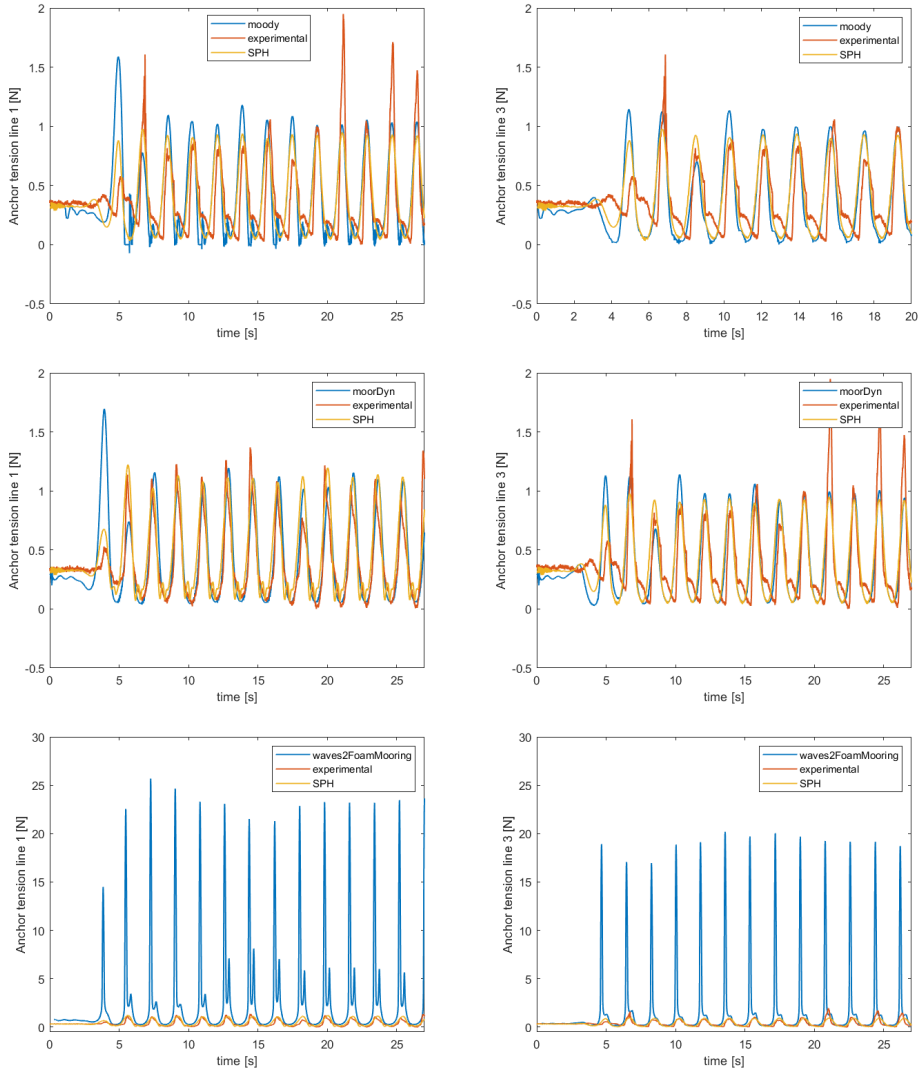


Figure 4.13: Tension at anchor point is shown, where line 1 is a front line, and line 3 is a back line.

higher than the tension experienced in the back line (line 2), respectively  $\sim 1.1$  N and  $\sim 0.8$  N. The quasi-steady model on the other hand overpredicts the tension by a factor of  $\sim 20$  for both the front and the back line. This confirms once more the hypothesis of bending absence causing the line to be "shorter" resulting in the tension spiking to extremely high values.

Apart from the motion results accuracy, another driver parameter for the choice of the optimal mooring line numerical model is the computational time needed for performing the simulations. Starting from the quasi-steady model, it required (133750.98 seconds)  $\sim 37$  hours of executionTime. Moody and moorDyn on the other hand respectively needed (125659 seconds)  $\sim 34.9$  hours and (126081.12 seconds)  $\sim 35$  hours. The results do not reflect the actual time needed, since for waves2FoamMooring the timestep decreased significantly every time the box sank, hence requiring much more time to resolve complex hydrodynamics phenomena (overtopping). However, the executionTime required to perform the 27 seconds simulation with the changed value of lineLength for waves2FoamMooring of  $\sim 35.4$  hours is still comparable with the two dynamic models. This consequently does not justify the poor results obtained with the low computational time expected.

# 5

## WIND/WAVES SIMULATION OF OC4 PHASE II SEMI-SUBMERSIBLE FLOATER

In the present chapter, the coupled aero-hydrodynamic responses of Phase II of OC4, (semisubmersible-supported wind turbine system) are investigated. The three dimensional Reynolds-Averaged Navier-Stokes (RANS) equations coupled with the  $k-\omega$ SST turbulence model are solved. First the model set up is described. Then the RAOs and damping ratios of the structure in 6 DOFs are determined by performing free decay tests. Then, the effect of turbine aerodynamics on floating platform response is investigated with proper comparison between the fully coupled wind/waves simulation and the FOWT only in wave conditions without wind.

### 5.1. OFFSHORE CODE COMPARISON COLLABORATION

The Offshore Code Comparison Collaboration Campaign is an initiative that aims to promote collaboration among researchers in the field of offshore wind. It focuses on the comparison of numerical simulations and experimental data to improve the understanding and modeling of offshore wind turbine behavior. Participants exchange and compare their numerical models, simulation methodologies, and experimental data sets to assess the accuracy and reliability of different approaches.

Other research projects have investigated modeling approaches for offshore wind systems, with specific focuses on wind turbine wakes **IEA Task 31-30** [47], **floating offshore wind systems (INNWIND)** [50], or **WaveLoads project** where extreme wave loading is studied [5]. The OC3 OC4, OC5, and OC6 projects are unique, however, in how they are run with a large number of participants ranging from research institutions and universities to and wind companies, using different modeling tools, theories, and approaches, with a concentrated effort to understand the drivers of modeling differences.

The work is analyzed collectively, and multiple iterations of the results are computed to better understand the reasons for the differences between participant results, thus allowing for a better understanding of the topic.

### 5.1.1. OC4

In OC4 project [77] the main goal was to verify offshore wind modeling tools by comparing simulated results of offshore wind systems from the various tools available (code-to-code comparisons). Once again different foundations were investigated.

- OC4 Phase I: jacket, 50m water depth.
- OC4 Phase II: floating semisubmersible, 200m water depth. Phase II involved the modeling of a semisubmersible floating offshore wind system developed for the DeepCwind project as shown in Figure 5.1. This concept was chosen for its increased hydrodynamic complexity compared to the floating system analyzed in OC3, the Hywind spar buoy. DeepCwind project aimed at generating field-test data for use in validating floating modeling tools. The turbine modeled in this project is the NREL 5MW Offshore Turbine [53], which differs slightly from the scaled one tested by DeepCwind and further simulated in phase II of OC5. 21 different load cases were performed in OC4 Phase II, considering varying levels of model complexity and a variety of ambient loading conditions. The load cases are ordered in increasing complexity, with three distinct groupings. The first group (1.X) is focused on static equilibrium simulation, modal analysis, and free-decay tests. These simulations are run with still water, and have the generator locked with a rotor brake. The second group (2.X) is focused on wave loading without wind and a locked rotor. The third and final group (3.X) examines combined wind and wave excitation, including regular and irregular waves, and steady and turbulent wind.

### 5.1.2. OC5

The Offshore Code Comparison Collaboration (OC3) and Offshore Code Comparison Collaboration Continuation (OC4), operated under IEA Wind Tasks 23 and 30 through code-to-code comparisons. Code-to-code comparisons, though, can only identify differences and they do not determine which solution is the most accurate. To address this limitation, the Offshore Code Comparison Collaboration, Continued, with Correlation (OC5) was published [79], with the objective of validating offshore wind modeling tools through the comparison of simulated responses to physical response data from actual experiments.

- Phase I of the OC5 project analyzes two different data sets, both focusing on the validation of hydrodynamic loads on cylinders, with no wind turbine present.
- Phase II of the project examines a more semisubmersible tested by DeepCwind in 2013 at MARIN test center. These tests, conducted at a 1/50th scale, investigated the response of the semi-submersible floater with a prototype turbine on top. The turbine is a scale reproduction of the NREL 5-MW reference wind turbine [54] with a flexible tower. The tower diameter was much smaller than it should have been, to ensure that the scaled version would match the first natural bending frequency.

### 5.1.3. OC6

During the OC5 campaign, it was discovered that most state-of-the-art mid-fidelity models based on the Morison equation and/or the potential-flow theory underpredicted the loads and motion of a semi-submersible offshore wind platform. The most significant one occurred at low frequencies, outside the range of linear wave excitation. This response underprediction can therefore be attributed to an underprediction of the non-linear wave excitation or overprediction of the hydrodynamic damping at the surge and pitch resonance frequencies. To better understand this issue, OC6 project was published.

- Phase Ia of OC6 [87] showed that although the inclusion of full quadratic transfer functions (QTFs) for the wave excitation from second-order potential-flow theory and the addition of Morison drag improved the results, the predicted low-frequency response was not close to that of the experimental measurements.
- Phase Ib [88] assessed the ability of higher-fidelity CFD simulation tools to accurately predict low-frequency hydrodynamic excitation and to overcome the issue.
- Phase III [2], under the IEA Task 30, focused on validating the aerodynamic loading on a wind turbine rotor undergoing large support structure motions. Numerical models of the Technical University of Denmark 10 MW reference wind turbine were validated using measurement data from a 1:75 scale test performed during the (UNAFLOW) project performed at the Politecnico di Milano wind tunnel.

## 5.2. SIMULATION BACKGROUND & MOTIVATION

During the OC4 phase II code-to-code comparison campaign, many mid-fidelity tools based on the potential flow panel approach were compared against each other. These models, even though they have the advantage of simple implementation and low computational time, have been shown multiple times to have theoretical and practical limits. Potential-based panel tools such as AQWA, ANSYS, Orcaflex, and FAST (developed by NREL), cannot directly incorporate the effect of fluid viscosity in roll direction so they do not calculate any roll damping. In FAST and AQWA, an additional damping coefficient based on experimental test data and implemented through the Morison strip-theory equation or through the Ikeda theory is usually applied. Thus, to correctly reproduce hydrodynamic loads with viscous roll damping, potential flow tools rely on experimental measurements. Moreover, as explained by Coulling et al in [16], to take into account flow-separation-induced drag, a quadratic drag model needs to be implemented in FAST, on top of the linear hydrodynamic forces. For OC4 semi-sub these coefficients are only applicable to the 4 big cylinder buoys and not to the cross braces, creating a big limitation, since for the DeepCWind semi-submersible a large component of the total hydrodynamic damping comes from flow-separation-induced drag. This also means that potential panel tools are not able to capture complex viscous interference effects for the motion of multi-structure platform geometries. Other theoretical limitations of potential panel approach besides fluid viscosity are the assumption of uniform flow acceleration and the inability of describing time-dependent force history correctly. Some physical phenomena, such as wave run-up against semi-submersible columns and viscous flow separation on the floaters, cannot be fully captured by the potential-based panel ap-

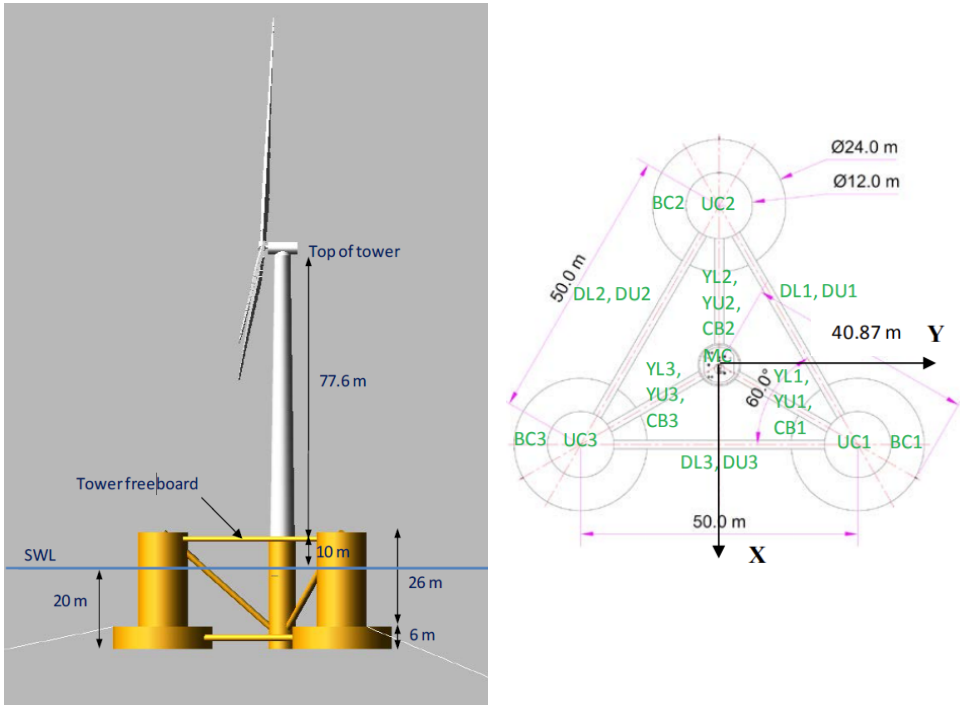


Figure 5.1: OC4-DeepCwind floating wind system design

proach and the Morison equation. Nonetheless, CFD approach can directly include all physical effects such as flow viscosity, hydrostatic stiffness, wave diffraction/radiation, wave run-up, and slamming of a floating platform.

Several FOWT CFD simulations have been performed focusing on the coupled hydrodynamics/aerodynamics analysis of floating platforms. Cheng and Wan [13] used the naoe-FOAM-SJTU solver with overset grid technique to simulate how the equilibrium position in surge and pitch changed while varying aerodynamic forces. Huang et al. in [42] performed hydrodynamic simulations of the OC4-DeepCWind floater in free decay tests, in regular waves, and in a survival condition with one mooring line broken. Tran and Kim in 2015 [85] used an unsteady hydrodynamic simulation using CFD method with dynamic mesh and overset grid to study the hydrodynamic responses of the DeepCWind semi-submersible floater under regular waves and compare it with a potential-based panel software. Zhao and Wan in 2015 [91] studied the interaction between the wind turbine and its semi-submersible floating system for OC4-phase II by comparing the floater RAOs and motions in wave and wind conditions first with a parked rotor and then with an operating wind turbine. Liu et al [61] examined the effects of the dynamic motions of the floating platform on the wind turbine aerodynamic performance and the impact of the wind turbine aerodynamics on the behavior of the floating platform and on the mooring system responses. Cheng et al. in 2019 [13] investigated

the impact of unsteady aerodynamics on the hydrodynamics and rigid body dynamics of the OC4 semi-submersible substructure. They additionally studied the influence of 6 DOFs on the inflow aerodynamics and wake characteristics using an in-house CFD software based on OpenFOAM. A second paper from Tran and Kim in 2016 [84] compared various computational results for unsteady aerodynamics, hydrodynamics, and fully coupled aero hydrodynamics including mooring line loads with test data of OC5-phase II and numerical results calculated by the NREL FAST code.

### 5.3. MODEL SET UP

The objective of this simulation set-up is to reproduce with OpenFOAM the phase II of the OC4 campaign. The whole system consists of the NREL 5-MW baseline wind turbine designed for offshore applications, the OC4 tower, the OC4 DeepCWind semi-submersible supporting the tower and the mooring system. The platform is composed of three offset columns with larger diameter heave plates, one center support column for the wind turbine and a series of horizontal and diagonal cross-bracings. It is noted that the diagonal cross-bracings have little influence on the platform motions, and the platform is regarded as rigid body, hence to balance the computational accuracy and computational time, they are not taken into account. Gross properties of the full-scale semi-submersible platform are defined in Table 5.1. The characteristics of the NREL-

parameter	unit	value
Depth of platform base below SWL (total draft)	m	20
Elevation of main column (tower base) above SWL	m	10
Platform mass, including ballast	kg	13,473,000
CM location below SWL along platform centreline	m	13.46
Platform roll inertia about CM	$kg \cdot m^2$	6.827E+9
Platform roll inertia about CM	$kg \cdot m^2$	6.827E+9
Platform yaw inertia about platform centreline	$kg \cdot m^2$	1.226E+10

Table 5.1: Platform gross properties

5MW offshore turbine and the tower are listed in Table 5.2. The system is attached to

parameter	unit	value
Rated power	MW	5
Hub height	m	90
Rotor mass	kg	110,000
Nacelle mass	kg	240,000
Tower mass	kg	347,460
Coordinate location of RNT CM	m	(-0.2 0.0 64.0)

Table 5.2: Turbine gross properties

the ground with three slack catenary mooring lines, which provide restoring forces for those degrees of freedom that are not damped by hydrostatics or hydrodynamics (yaw, sway, surge). The mooring lines characteristics are listed in Table 5.3. By performing

parameter	unit	value
Number of mooring lines	-	3
Angle between adjacent lines	deg	120
Depth to anchors below SWL	m	200
Depth to fairleads below SWL	m	14
Radius to fairleads from platform centerline	m	4.0868
Radius to anchors from platform centerline	m	837.6
Equivalent mooring line mass in water - air	kg/m	108.63 - 113.35

Table 5.3: Mooring lines gross properties

some simple calculations to combine the properties of the turbine with the floater, the characteristics of the full FOWT system are derived and listed in [Table 5.4](#).

## 5

parameter	unit	value
Structural mass	kg	1.407E+7
CM location below SWL	m	9.6475
CM location along x-axis	m	-9.844E-3
Total structure roll inertia about CM	$kg \cdot m^2$	1.1E+10
Total structure pitch inertia about CM	$kg \cdot m^2$	1.1E+10
Total structure yaw inertia about CM	$kg \cdot m^2$	1.226E+10

Table 5.4: FOWT full system main properties

The hexahedral computational domain is generated using blockMesh utility. Its dimensions change depending on the wavelength generated by waves. As studied in the convergence study in [chapter 3](#) for x-direction, the inlet generation zone is 1 wavelength, the absorption zone is 2 times the wavelength, and the propagation zone is as well 2 wavelengths. In y-direction, the width of the NWT is equal to the propagation zone length, so twice the wavelength simulated. In z-direction, the height of air is chosen to be 1.5 times the height of the OC4-NREL-5MW turbine tower, so  $2 \cdot 90$ , while the water depth is 200 m according to the simulation set-up specifications of OC4 phase II. Following again the results of the convergence study chapter, the size of the cells in the free surface region is 10 cph, meaning that the total number of cells varies with the type of generated waves. The geometry of the OC4 semi-submersible is created using the open-source CAD software SALOME [81] and then exported as an stl file. It is then imported in openFOAM through snappyHexMeshDict, and it is snapped, castellated, and refined with cells for the boundary layer, to capture the flow separation and viscous drag at the fluid-structure interface. The momentum equation for the fluid flow [Equation 2.17](#) is closed using the  $k-\omega$ SST turbulence model, to capture the vortices and turbulence flow around the edges of the structure.

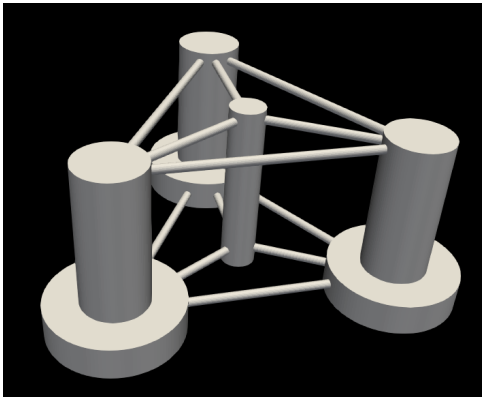


Figure 5.2: (a) side view

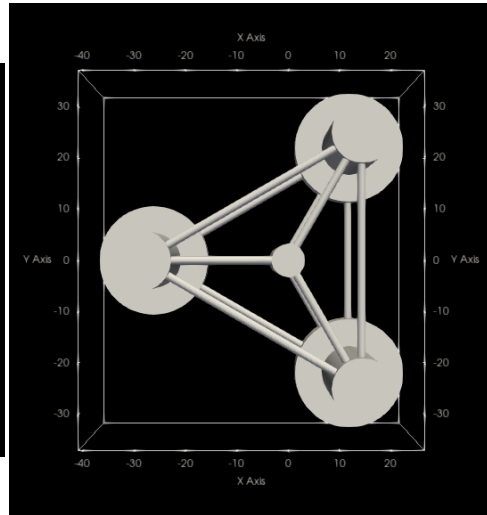


Figure 5.3: (b) top view

### 5.3.1. MESH CONVERGENCE

In order to perform the simulations and to avoid the mesh having any influence, a grid-convergence study is performed. Four different mesh configurations with slightly different geometries, with different levels of refinement, different expansion ratios, and different boundary layer thicknesses and numbers of cells are generated and compared. The number of cells per mesh is shown in [Table 5.5](#). They are compared by performing a surge free decay test: the OC4-phase II semi-submersible is initially displaced 10 meters in the positive x direction and is left free. These free decay simulations are performed with no wind, no waves, and no current. The density of air is  $1.225 \text{ kg/m}^3$  and the water density is considered to be  $1025 \text{ kg/m}^3$  (as salty water). The static pressure at the far-field boundary is assumed as 101,325 Pa. The effect of eddy viscosity and flow turbulence is captured with the turbulence model  $k-\omega$ SST since the results obtained by Tran and Kim in [85] clearly showed that in free-decay tests, the best viscosity models are either laminar flow,  $k-\omega$ SST, or Spalart-Allmaras models. Only one DOF is allowed, which is the linear displacement along the x-axis. The floater is supposed to oscillate for a period of transient time until it finds its equilibrium position and reaches a steady state solution. For this reason, the simulations are run for a very long time, 600 seconds, to let the solution reach a steady-state. The mooring line model used for this study is moody. Moody has been chosen over moorDyn, since this FEM model is especially accurate in capturing snap loads [section 4.2](#). Hence for large free decay motions, it must be more accurate, especially for surge, sway, and yaw directions in which there are no hydrodynamic restoring forces.

The results of the surge free-decay tests are presented in [Figure 5.4](#) and in [Appendix C](#) all four meshes are displayed both from a yz plane (front view) and from a xz plane (side view). From the results of the surge free decay, the most damped simulation is the fine

mesh	coarse	medium-coarse	medium-fine	fine
# cells	1.138 M	1.657 M	2.246 M	2.532 M

Table 5.5: Mesh convergence study

mesh, while the less damped one is the coarse mesh. This is due to the absence of viscous damping due to an accurate representation of the surface and of the water/air interface. For this reason, the coarse mesh is excluded a priori. The medium-coarse, medium-fine, and fine meshes all show very similar results in the decay test, with an error that is less than 1%, meaning that the mesh has zero influence on the accuracy and precision of the results obtained. As a consequence, the medium-coarse mesh, with 1.657 million cells is chosen for the next simulations.

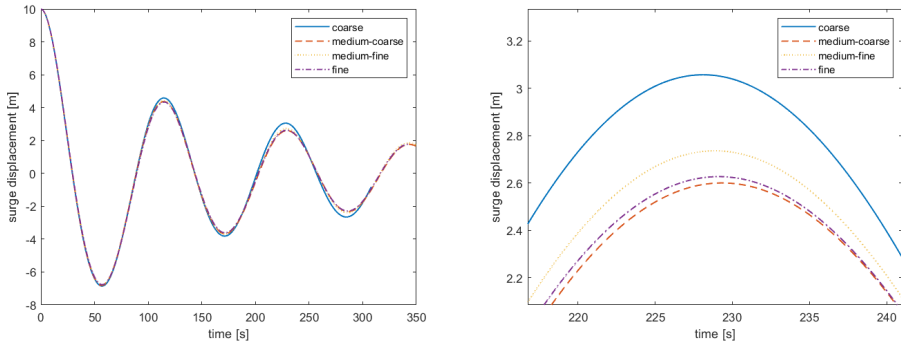


Figure 5.4: Results of mesh convergence study

#### 5.4. OC4/OC5 FREE DECAY TESTS

In this section, free decay in 4 DOFs is simulated: surge, sway, heave, and pitch. This is done to make sure that all the models and assumptions of the setup are correctly tuned. These include the mesh motion model, the boundaries, the mooring line dynamic model, the turbulence model, and the approximation schemes for the solution. The results obtained with the present study are compared with the experimental ones obtained by [16], and other studies, both low fidelity (FAST, AQWA, Simo/Riflex) and high fidelity (unsteady CFD, OpenFOAM). It was chosen to analyze the free decay test response in 4 DOFs and not in all 6 for time constraints. Hence, it was considered enough for validation purposes to only analyze the responses for surge, sway, heave, and pitch. This is because, in heave and pitch, the influence of mooring line model choice and setup has little to no influence. On the other hand, hydrostatic stiffness and viscous flow phenomena such as viscous damping, vortex shedding, viscous drag, and skin friction are the main contributors to the stiffness matrix  $K$  of Equation 2.6, which brings the system back to its original state. On the other hand, surge and sway tests are highly dependent on the parameter setup and choice of the mooring line model, since mooring stiffness is the only active force bringing the system back to its equilibrium state,

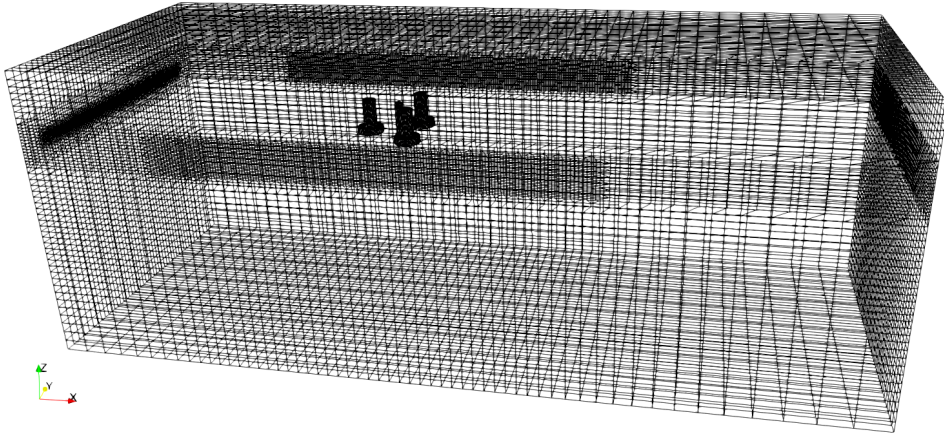


Figure 5.5: representation of the full meshed domain with ParaView. To notice the different cell size in the FOWT boundary layer and in the free surface region

DOF	exp	FAST	AQWA	unsteady CFD	OpenFOAM	Present
Surge	107.0	107.0	112.5	108.1	107.2	109.6
Sway	112.0	113.0	112.5	114.5	-	110.3
Heave	17.5	17.3	17.4	17.8	17.5	17.9
Roll	26.9	26.7	24.7	25.3	-	-
Pitch	26.8	26.8	25.8	25.2	27.4	25.7
Yaw	82.3	82.7	80.2	83.3	-	-

Table 5.6: Natural periods for 6 DOFs

and without them, the floater would find a new equilibrium position. In surge and sway, however, fluid damping as viscous drag or is important to dampen the oscillations, hence are contributions to the damping matrix  $B$  of Equation 2.6 but have no influence on the stiffness  $K$ . The initial displacements for the free decay tests are presented in Table 5.7.

DOF	displacement
Surge	22 m
Sway	20 m
Heave	6 m
Pitch	8 deg

Table 5.7: Initial displacement free decay tests

The two main results from free decay tests studied to validate the setup of the OC4 DeepCWind semi-submersible are the **natural periods** and the **damping ratios**. First, in Figure 5.6 the free decay motions in the time-domain are compared with benchmark results from literature: OrcaFlex diffraction model (low-fidelity model for RAOs calcula-

tions from OC4 phase II code comparison), and unsteady CFD from Tran & Kim [85].

To initialize the free decay test in surge, sway, and heave it is straightforward since the translations are linear. The fairlead points were just translated by the same amount stated in Table 5.7. For the pitch free-decay test the initial set-up is a bit more complicated. To determine the new fairlead attachment points for the three mooring lines, rotational matrices had to be used. By performing a matrix product between the pitch rotational matrix  $R_y(\beta)$  (where  $\beta$  is the pitch angle in radians) and the initial fairlead position matrix, the rotated position is retrieved.

$$\begin{bmatrix} \cos(\beta) & 0 & \sin(\beta) \\ 0 & 1 & 0 \\ \sin(\beta) & 0 & \cos(\beta) \end{bmatrix} \cdot \begin{bmatrix} x \\ y \\ z \end{bmatrix} = \begin{bmatrix} x' \\ y' \\ z' \end{bmatrix} \quad (5.1)$$

In order to retrieve the correct rotation angles as a result, the same rotational matrix needs to be applied to change the orientation of the axis for the floating system in the simulation. This, in fact, is not any more consistent with the "fixed" earth coordinate system but is rotated around the y-axis by the angle  $\beta$ . In case one wanted to analyze the yaw or roll-free decay, the same procedure described above can be followed, but replacing the pitch rotational matrix, with the roll  $R_x(\theta)$  or the yaw  $R_z(\gamma)$  one.

From Table 5.6, where the natural periods results are shown, the values corresponding to sway, heave, and pitch free-decay tests are totally in accordance with the unsteady CFD and OpenFOAM benchmark results. Compared to experimental values, there is a little more difference of 1.7 s, 0.4 s, and 0.7 s respectively. However, these errors in percentage do not rise above 2.6% meaning that the results can be considered correct. A slightly higher difference of 2.7 seconds is found in the surge decay, and to detect the reason for this discrepancy more studies need to be conducted. The difference, however, is less than 2.5%, making the results accurate enough to overlook this deviation. As pointed out by [44], although both the model tests and the simulation were based on exactly the same design and specifications, differences existed between the simulation model and the physical scale model. These are the mass distribution, and the structural flexibility of the turbine rotor and tower, and the parameters for the mooring line setup. Hochkirch in [39] added that the differences between model-scale flows and full-scale flows can have significant effects due to the relatively different boundary layer and wave breaking, which are concerned primarily with the changes between model-scale and full-scale model.

To validate the model, besides the natural periods' comparison, the damping ratios must also be determined and investigated. The damping  $\zeta$  describes how oscillations and vibrations in the system decay after an initial perturbation from the equilibrium state. Since the whole floating system is considered to be underdamped (damping ratio  $< 0.5$ ), and the only damping comes from viscosity, hydrodynamic, and mooring lines, the damping ratio is determined through the logarithmic decrement method. The logarithmic decrement is defined as the natural logarithm of the amplitude ratio of any two

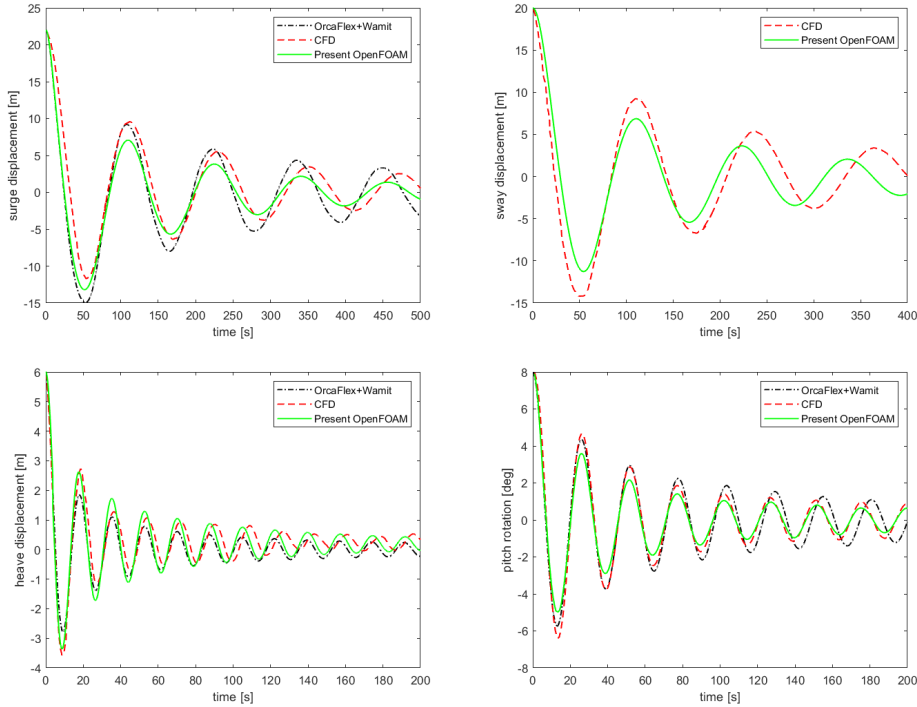


Figure 5.6: Results of free decay motions in time domain in order from top left to bottom right: surge, sway, heave, pitch.

successive peaks:

$$\delta = \frac{1}{n} \ln \frac{x(t)}{x(t+nT)} = \ln \frac{x(1)}{x(3)} \quad (5.2)$$

where  $x(t)$  is the overshoot (amplitude - final value) at time  $t$  and  $x(t+nT)$  is the overshoot of the peak  $n$  periods away, where  $n$  is any integer number of successive, positive peaks. The damping ratio is then found from the logarithmic decrement by:

$$\zeta = \frac{\delta}{\sqrt{4\pi^2 + \delta^2}}. \quad (5.3)$$

To determine the damping ratio  $\zeta$ , the logarithmic decrement  $\delta$  is determined between each consecutive peak. Figure 5.7 shows the damping ratios for surge, heave, and pitch over the initial cycle amplitude in the free decay test. The results indicate that some discrepancies are found also in the damping, but the overall trend is in accordance with both experimental and unsteady CFD benchmark results. This means that overall the present results are in good agreement with the high-fidelity and experimental model results.

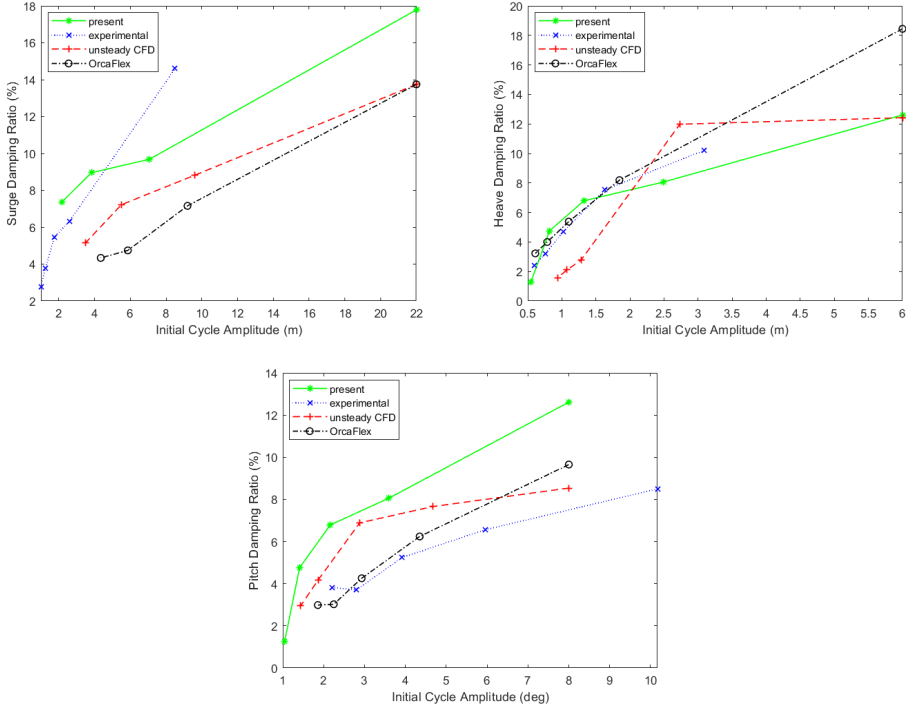


Figure 5.7: Damping ratios determined with the logarithmic decrement. From top left: surge, heave, pitch.

## 5.5. OC6 FREE DECAY TESTS

In order to finalize the validation in free decay tests, the present OpenFoam model is compared with OC6 phase I results [87]. This is done to confirm whether the current OpenFOAM model is correctly initialized or not. This comparison serves as proof to check if the discrepancies between the present model and the OC4/OC5 can be reduced or are intrinsic uncertainties between experimental results, potential flow solvers, and the fully non-linear viscous solver.

The OC6 phase I campaign was undertaken to investigate the underprediction of low-frequency hydrodynamic loads and responses in surge and pitch obtained during OC4 and OC5. During this campaign, different software and tools are validated against new experimental results obtained from wave basin testing. The experiments performed for OC6 phase I use the same semi-submersible floater as used in OC5, with slight differences in the draft, mass, and mass moments of inertia which will not be mentioned here, but are explained in detail in [78]. The main differences in the testing are made to the mooring lines. The mooring system is in fact replaced by a linear spring and wire mooring system that reproduces the angle at the fairlead and the linear response behavior of the original catenary system. The OpenFOAM required inputs for initializing a linear-spring restraint are minimal: fairlead and anchor points, length at rest (m), stiffness EA

(N), and linear damping (N.s/m). The only value not explicitly given in the OC6 NREL reference paper [78] was the damping, which is assumed to be 0 since the lines are taut.

The focus of this campaign was indeed on pitch, heave, and surge DOFs, and in [Figure 5.8](#) the free decay tests in those DOFs are presented. At first glance, the results seem

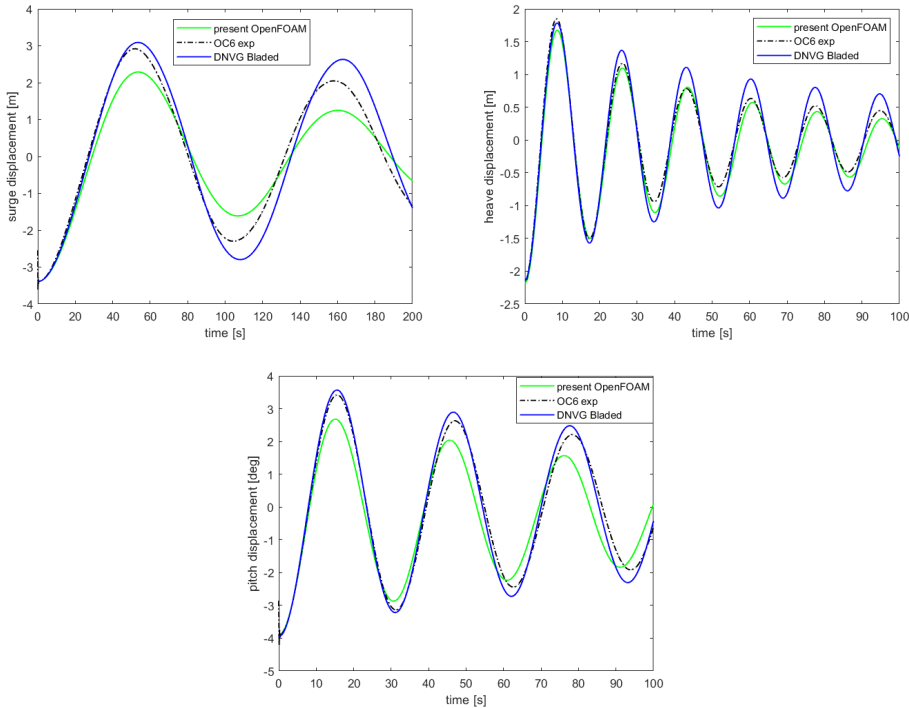


Figure 5.8: Comparison of free decay test in surge, heave, and pitch direction between the present OpenFOAM results, experimental results, and DNVG results using potential flow solver Bladed

to confirm the small discrepancies found during the OC4/OC5 comparison. However, since for this campaign, the data given was more accurate and more complete, the errors both in phase and in the natural period in all the 3 DOFs do not exceed 1.5%, meaning that the accuracy of the present CFD model is increased. However, the main difference is in the amplitude of the oscillations, which in the present study are more damped. This is explained by the fact that OpenFOAM is a high-fidelity CFD software, which includes non-linear viscous effects: viscous drag, skin friction, and vortex-induced drag.

After completing the thorough study comparison to validate the present hydrodynamic model, the next step is to simulate the floating system in non-linear regular wave trains and under a constant thrust force reproducing the presence of the rotor in a wind field.

## 5.6. EFFECT OF AERODYNAMICS ON HYDRODYNAMICS

In this section, the effect of rotor thrust force on the hydrodynamics of the floater is going to be analyzed. Different conditions are examined, in order to have a complete overview of the effects and discrepancies. Several wave trains with different intensities will be simulated, each one accordingly associated with a wind speed and a thrust force. Each condition is characterized by waves with varying wave height  $H$ , wave period  $T$ , wave length  $\lambda$  and by a wind speed and the associated thrust force. Table 5.8 shows the 3 cases examined. Each wave type has been selected so that "all" sea states are tested, from calm (**case 1**), mild (**case 2**), to rough (**case 3**). Each of these cases has been carefully selected from literature and experimental campaigns. Specifically, case 1 is taken from the OC4 code-to-code comparison campaign [45], case 2 is taken from Zhao and Wan [91], and case 3 is taken from Cheng and Wan [13].

case	height (m)	period (s)	wavelength (m)	wind speed (m/s)	thrust (kN)
Case 1	6	10	156.13	0	0
Case 2	3.66	9.7	146.90	5	268.9
Case 3	4	10.0	156.13	11	790.615

Table 5.8: non-linear periodic regular wave and wind field with associated thrust force analyzed cases

### 5.6.1. MODEL SETUP AND ASSUMPTIONS

In every case, non-linear regular second-order Stokes waves are numerically simulated with the waves2Foam toolbox. The mesh morphing technique solving the Laplace + diffusivity equation to accommodate the 6DOFs of the floating system is performed in OpenFOAM with the use of the 2-phase dynamic mesh solver waveDyMFoam. The wind field will be simulated by assuming a constant thrust force at the hub height (90m above MWL). The application point of this constant load is rigidly connected to the COG of the floating system, hence it moves accordingly to the motions of the semi-submersible. This strong assumption is justified in the subsection 5.6.2, where a comparison between all the forces at the floater boundaries is made and it is further explained and justified. The thrust values shown in Table 5.8 are directly determined from the official thrust curve of the NREL 5MW reference turbine for offshore applications Figure 5.9, given the correspondent wind speed. Besides the thrust load, an additional important input value for regular wave simulations is  $\lambda$ . This parameter is often not provided in the literature, since it is dependent on the wave period and water depth, values which are usually given. For this reason,  $\lambda$  is defined through the non-linear dispersion relation (Equation 5.4); and with the help of Matlab native function fsolve it can be solved as a system of non-linear system equations.

$$\lambda = 2T \frac{g}{2\pi} \tanh \frac{2\pi D}{\lambda} \quad (5.4)$$

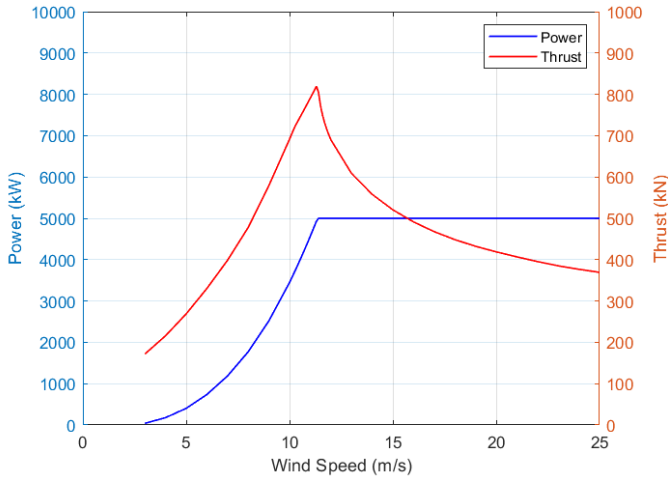


Figure 5.9: Thrust curve of 5MW NREL reference offshore turbine [54].

### 5.6.2. RESULTS

All the results obtained with OpenFOAM are compared with benchmark results taken from the literature. Additionally, the most relevant outputs are also compared with **OpenFAST** results. OpenFAST is a mid-fidelity open-source software developed by NREL to simulate onshore and offshore turbine behaviors. OpenFAST is coupled with the external hydrodynamic solver **HydroDyn**, a software based on the second-order potential theory to analyze wave structure interactions. The Boundary Element Method (BEM) is used to solve for the velocity potential and fluid pressure on the submerged surfaces of the bodies to solve the diffraction and radiation problems. These solutions are then used to obtain the relevant hydrodynamic parameters including added-mass matrix  $A$ , damping coefficients matrix  $B$ , hydrostatic stiffness coefficients matrix  $C$ , exciting forces  $F_{hydro}$ , response-amplitude operators (RAOs), pressure, fluid velocity, and the mean drift forces and moments. These parameters are all required inputs in OpenFAST to solve the equation of motion Equation 2.6. The mooring stiffness matrix  $K$  is obtained by coupling OpenFAST with an external mooring line solvers (MAP, FeamMooring, moorDyn). Whereas, the aerodynamic external forces  $F_{aero}$  are solved by **AeroDyn**, a time-domain wind turbine aerodynamics module, that enables aero-elastic simulation to calculate all the forces on the rotor by applying the actuator line theory [75].

### CASE1

The results for **case1** show the behavior of the FOWT under regular waves. The present OpenFOAM results are compared with present OpenFAST and benchmark OrcaFlex values. The simulations in OpenFAST and OpenFOAM are run for a total of 600s and 300s, while the OrcaFlex time-domain results are only given for 60s. For completeness, for each DOF analyzed (surge, heave and pitch), on the left, the response of the full time-

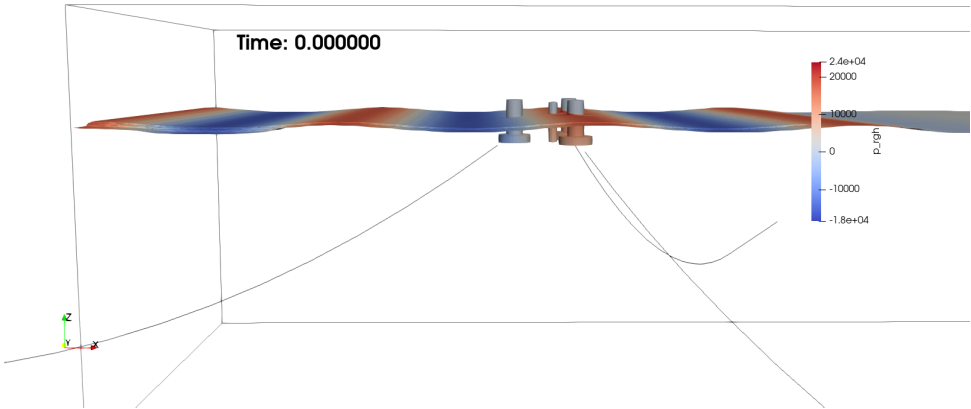


Figure 5.10: Snapshot of the FOWT at  $t=0.0s$  (start of the simulation) using ParaView postProcessing for case 3. Contour surface at  $0.95 \alpha_{water}$  for capturing the surface elevation. Color grid representing the fluid dynamic pressure

5

domain simulation is shown and on the right, a zoom on the time window between 200s and 250s is displayed. The full-time-domain outcomes on the left are represented to spotlight the shift between transient phase and steady state solutions. For each of the three DOFs the transient has a slightly different duration, which is driven by the natural period length and by the overall amplitude. The larger these two values are the longer the transient will last. However, a similar trend can be noticed, because after  $\sim 150s$  all three have reached a somewhat converged solution. The entire time result plot also shows a first approximation of the amplitude and phase accuracy of the results. Indeed, surge and heave seem to overlap reasonably well with the OrcaFlex and OpenFAST outcomes. On the other hand, OpenFOAM pitch displacement appears to be overdamped, resulting in a lower amplitude range. These preliminary conclusions are further confirmed by the zoomed plots on the right-hand side. Once again, for surge and heave the mismatch in phase and amplitude is negligible, while for pitch the discrepancy is highlighted in [Figure 5.14](#). In order to identify the reason for this mismatch, it is useful to remember that case1 simulation involves only non-linear regular waves, wind forcing is not considered yet. This might allow viscous damping to play a more important role than in case2 and case3, leading to slightly more damped results than in potential-flow solvers. Similar outcomes were however obtained in [section 5.4](#) and [section 5.5](#) for the free decay tests: the results in heave and pitch resulted in a shorter natural period, with a higher critical damping ratio.

The mooring line tension comparison is a more sensible value to compare since the mooring model used could be substantially different. Figure in the left of [Figure 5.15](#) shows the fairlead point tension variation in time of the front central line. This value is important because it is the mooring line aligned with the wave direction, generating the

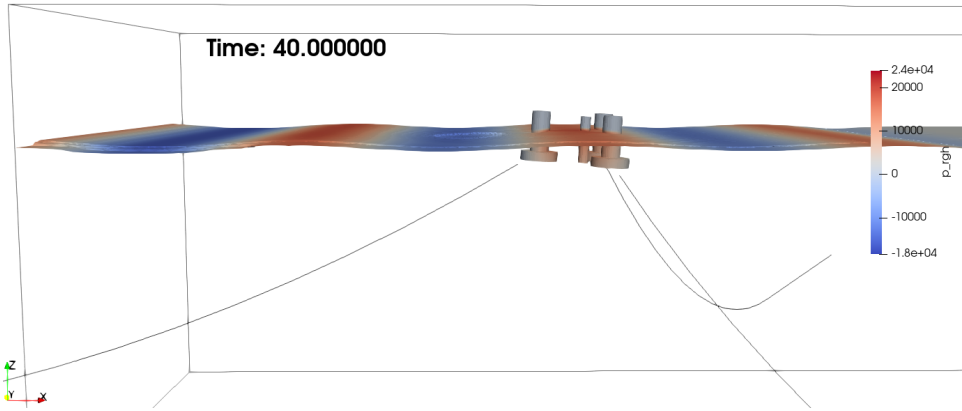


Figure 5.11: Snapshot of the FOWT at  $t=40.0s$  using ParaView postProcessing for case 3. Contour surface at 0.95  $\alpha_{water}$  for capturing the surface elevation. Color grid representing the fluid dynamic pressure

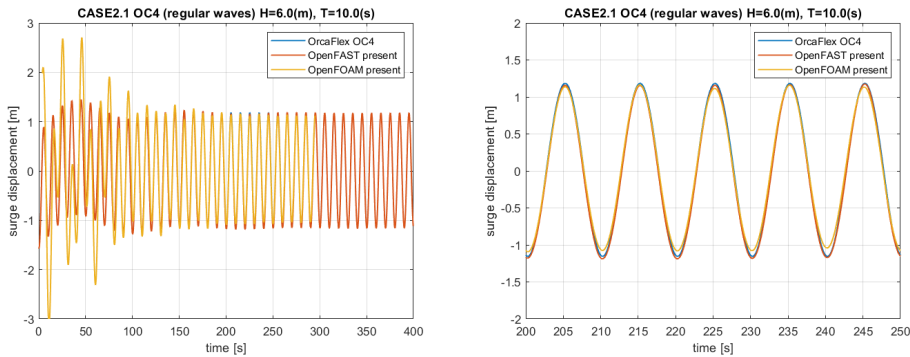


Figure 5.12: CASE1 surge time-domain floater displacement

highest forces in the lines. On the right, the anchor tension of the mooring line on the right-hand side (facing the waves) is plotted. Surprisingly, for the center line a very good match is found with OrcaFlex mooring results, especially for the amplitude range, where both results perfectly overlap. A substantial deviation resulted for the anchor tensions of line 1, in which the present OpenFOAM values outcomes ranged between 700.5kN and 711kN, while OrcaFlex ones oscillate between larger amplitudes of 697.5kN and 714kN. This discrepancy is not negligible, and deeper studies need to be performed to accurately address the problem, which could be related to a different mooring initial setup, or to an intrinsic diversity in the numerical mooring models.

## CASE2

Case2 (from Table 5.8) represent mild environmental conditions. In addition to case1, case2 also simulates the forces of a uniform 5m/s wind field on the FOWT. This is accomplished by simulation in OpenFOAM a constant thrust force applied at a point at hub height (90m above SWL), mimicking the real behavior of aerodynamic forces on

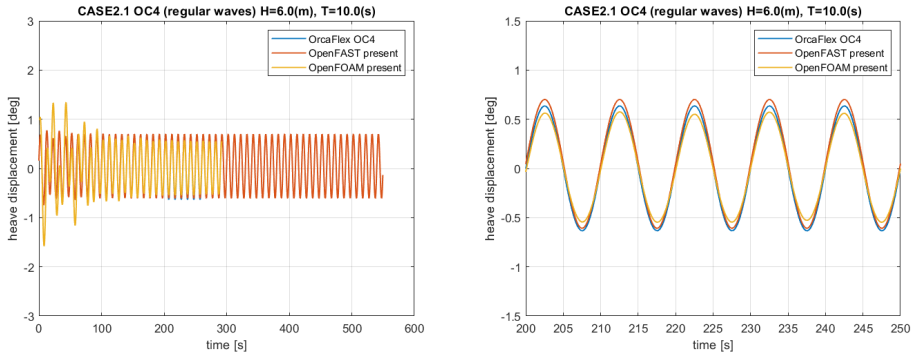


Figure 5.13: CASE1 heave time-domain floater displacement

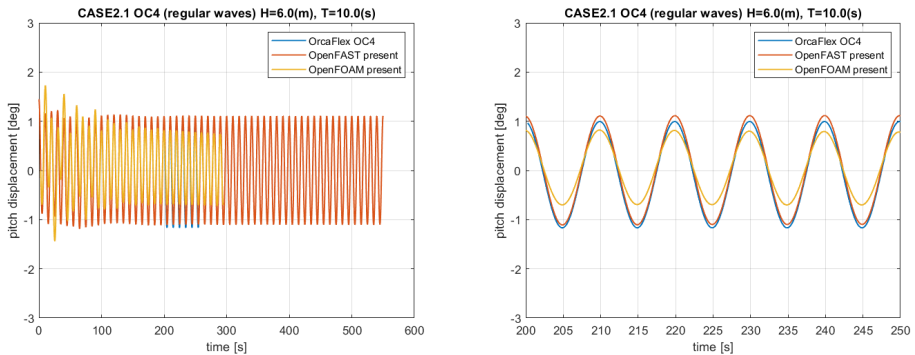


Figure 5.14: CASE1 pitch time-domain floater displacement

5

FOWT. The assumption of constant thrust force is justified in the following results. Once again, as it was done for case1, the results are confronted and validated against potential-flow results obtained with OpenFAST, and this time with literature CFD results taken from [91]. First, the displacement motions are shown in surge and pitch direction, together with the surface elevation profile. Then, additional results on the forces acting on the floater body are shown. The interface height is captured through the usage of wave gauges in OpenFOAM, with the postProcessing function object `interfaceHeight` available for OpenFOAMv-2012. The time surface elevation is an extremely important parameter to check, since all the simulation outcomes are affected by it. For this reason, the wave gauge position must be carefully chosen, to find a location in the refined mesh region that resents the influence of neither the generation relaxation zone nor the semi-submersible reflected and radiated waves. The interface height of Figure 5.16 shows that a perfect match is obtained between the analytical solution of second-order Stokes waves and the numerical simulated one. The only little differences visible are in the periods around 60s but those discrepancies are encountered in the transient solution (before 150s) and consequently can be safely ignored.

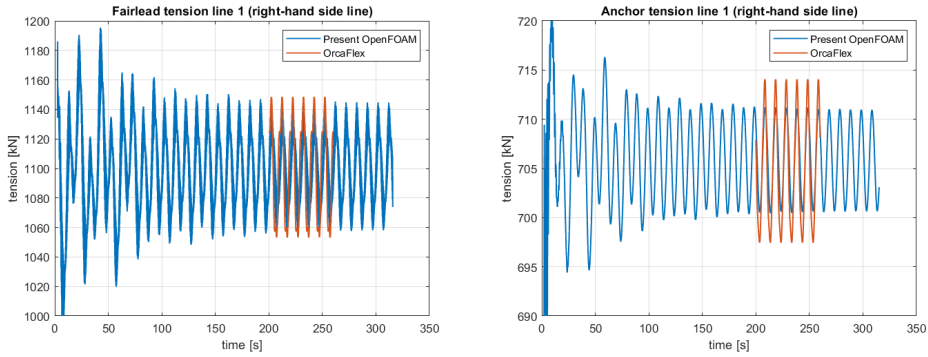


Figure 5.15: CASE1 mooring tensions in kN

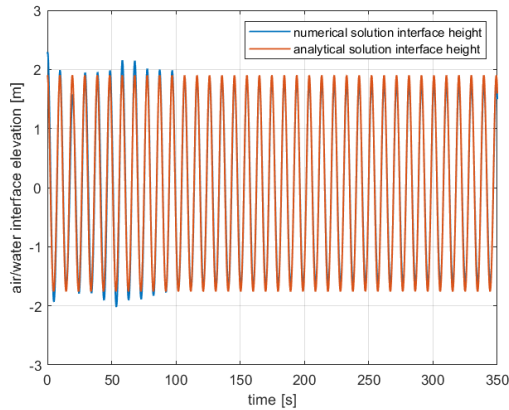


Figure 5.16: water/air interface elevation in time. Comparison between numerical and analytical solutions

After performing a brief mesh sanity check, the floater displacements can be presented. Both pitch and surge time displacements show a good agreement with potential flow and CFD results. However, some important facts must be noted. Starting with surge displacement (left plot of Figure 5.17), it is interesting to see that even though the transient of OpenFOAM and OpenFAST seem to be exactly opposite one another with respect to phase, the steady-state solution is in good accordance between the two, with OpenFOAM new surge equilibrium position being located in slightly more positive  $x$  direction. Nonetheless, the "opposite" transient behavior is mainly driven by a different initial setup of the numerical simulations. In this regard, in OpenFOAM the floater is first moved in the negative  $x$  direction (in the numerical domain this means that the floater is moved towards the generation zone of the waves) because the overall COG of the FOWT is shifted due to the overhang of the rotor nacelle assembly. Then the FOWT oscillates between positive and negative values until it reaches a stable position at a value of  $x = +5.5\text{m}$ . In OpenFAST, the overhang of the RNA is not possible to capture, and this

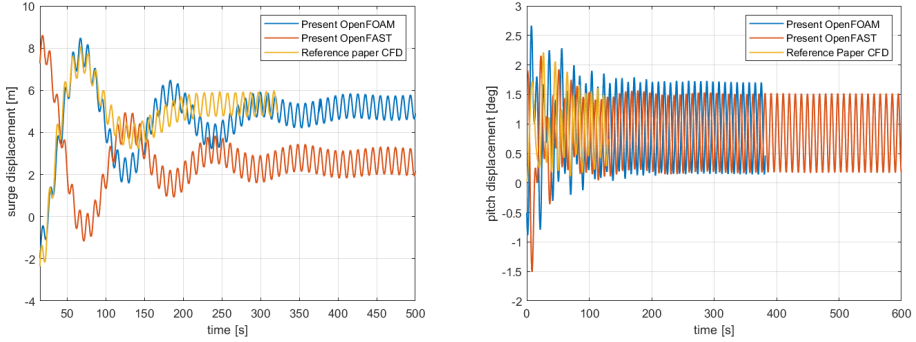


Figure 5.17: CASE2 surge and pitch time-domain FOWT displacements

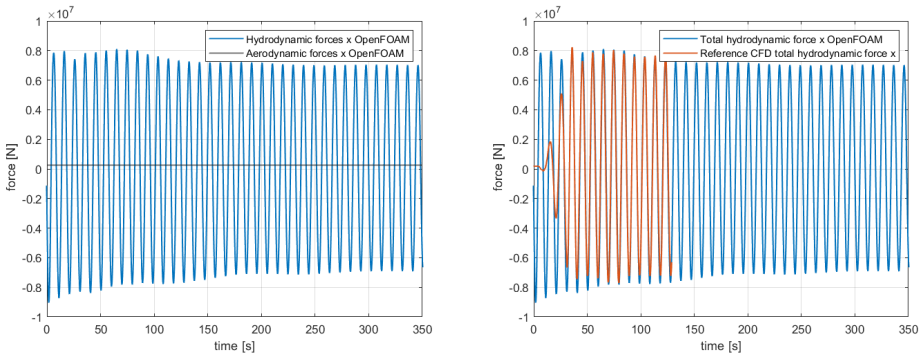


Figure 5.18: CASE2: on the left comparison between aerodynamic and hydrodynamic forces, on the right hydrodynamic forces from reference paper CFD [91] and present OpenFOAM.

explains why the transient behavior is symmetrical to the OpenFOAM one since the first FOWT motion in negative  $x$  direction is not captured. Pitch motion, presented on the right plot of Figure 5.17, is compared with OpenFAST and CFD results from [91]. The higher pitch amplitude seen in OpenFOAM could be explained by the assumption of constant thrust force. This indeed could lead to higher mean aerodynamic force seen by the turbine rotor. Moreover, due to the uncoupled behavior of hydrodynamic-induced motions and aerodynamic forces, some damping effects such as aerodynamic damping are not captured, resulting in an unrealistic overestimation of the motions.

As previously anticipated, the assumption of constant thrust force to resemble the rotor aerodynamic forces in a 5m/s uniform wind field needs to be supported. This is done by plotting in the same graph the total hydrodynamics forces in the  $x$  direction on the floater boundary and the aerodynamics ones. The comparison showed in Figure 5.18 highlights the different magnitudes of the two forces. Hence, the hydrodynamic forces oscillate with the wave period in a range between 8MN and  $-8$ MN, while the aerodynamic force is constant at a value of 0.268MN. This means that there are almost two or-

ders of magnitude of difference between the hydrodynamic and the aerodynamic forces applied to the FOWT. This argument supports the choice of simulating a constant aerodynamic force when the main focus of the simulation is the hydrodynamics, such as this thesis. This strong choice helped significantly reduce the overall mesh count that would have been needed if the rotor was also represented. However, all the aerodynamic effects, such as wake rotor interaction, aerodynamic damping, unsteady aerodynamics, laminar/turbulent boundary layer transition in the airfoil, and overall rotor efficiency and power production cannot be studied with this kind of setup.

By using "libforces.so" library as functionObject in OpenFOAM, it is possible to retrieve many more output values that can be used for further validation of the model. These are in fact all the forces and moments applied to the floater boundary, with distinctions between viscous and pressure ones. Once all the force and moments applied

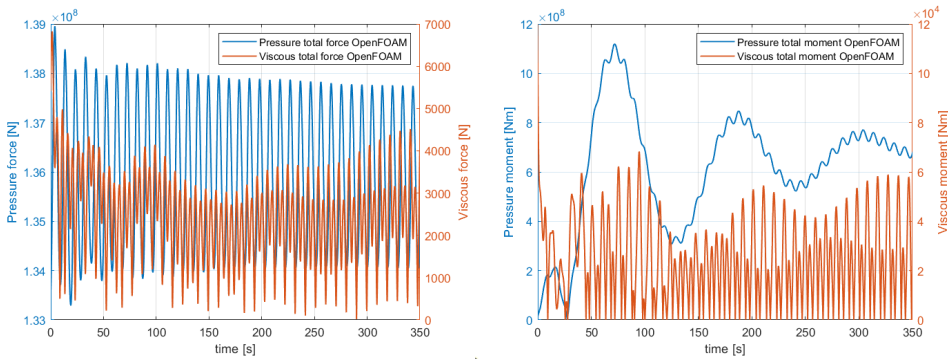


Figure 5.19: CASE2 comparison between viscous and pressure total forces and moments on the floater boundary.

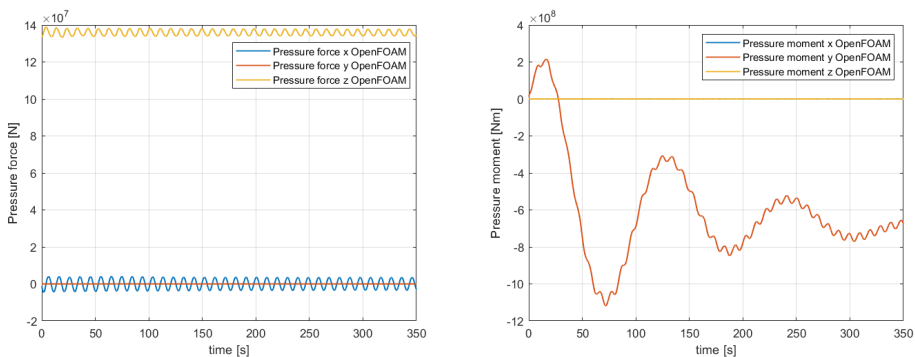


Figure 5.20: In the left figure, pressure force against time in x, y, and z direction. In the right graph, pressure moment against time around x, y, and z axis. Case 2

to the different cylinders of the semi-submersible are obtained from a CFD software,

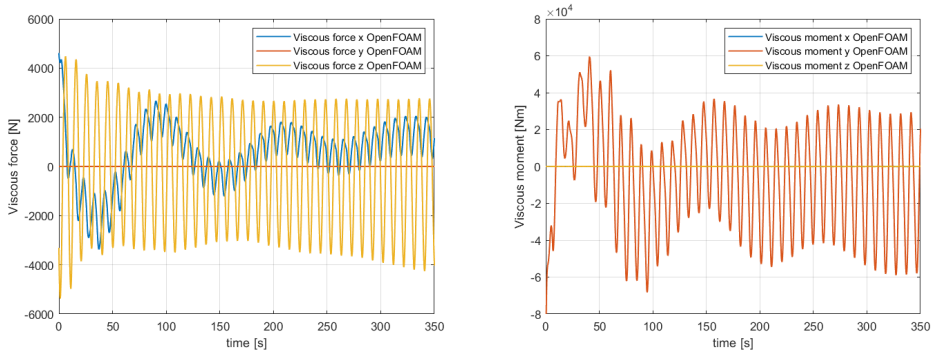


Figure 5.21: In the left figure, viscous force against time in x, y, and z direction. In the right graph, viscous moment against time around x, y, and z axis. Case 2

## 5

one can easily determine the added mass and drag coefficients which in turn can be used for potential-flow and panel-based solvers, such as OpenFAST and OrcaFlex. Indeed, for slender structure members  $\lambda > 5D$  (wavelength  $>$  5 times the member diameter), sufficiently small to allow the gradients of fluid particle velocities and accelerations to be neglected, wave loads may be calculated using Morison formulation for forces. Consequently, in these conditions, with the coefficients tuned from high-fidelity tools, potential-flow solvers can be safely used instead of CFD ones, saving precious computational time.

### CASE3

Case3 represents "survival" environmental conditions, with 4m wave height, 10s wave period, and 11m/s wind speed, which from [Figure 5.9](#) corresponds to almost the rated wind speed and therefore to the highest thrust force applied to the turbine rotor. The main purpose of simulating such conditions is to prove that the model works well even in such a scenario. Considering indeed that most of turbines nowadays are built and designed to be operational for 25-30 years, it is not unlikely that conditions like case3 or worse are encountered throughout the FOWT lifespan. These types of simulations, with even stronger winds and higher waves, are called survival simulations, and have the objective of verifying whether or not the FOWT is able to withstand such harsh conditions. If the design is not optimized enough, then the whole process of modeling the FOWT must iterate until such certification of survival is obtained. Usually for survival conditions, the 30 or 50-year most probable extreme (MPM) for wind speed and wave height is calculated from the metocean data, and the hydrodynamic survival conditions simulation is performed based on those values. In this case, since the goal of this chapter is validation and not proof of concept or design process of FOWT, the rated wind speed with 4m waves is considered to be a strong enough case with sufficient accessible data to compare the outcomes. Additionally, in strong environmental conditions, the stability of the OpenFOAM model is also checked: strong and sudden accelerations caused by the intense thrust force cause high moments on the floater and snapping loads on the mooring lines, testing the quality and stability of the model.

Case3 OpenFOAM results are compared with the results obtained by Cheng and Wan in [14]. First, the FOWT waves induced motions in surge and pitch are presented. Sim-

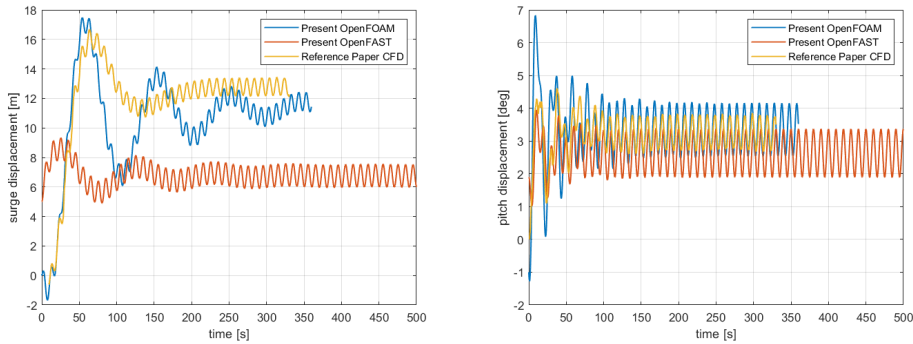


Figure 5.22: CASE3 FOWT motions. Left graph surge, right graph pitch.

ilar conclusions to case2 for the motions can be drawn as well for case3. Figure 5.22 compares FOWT motions between present OpenFOAM, OpenFAST, and [14]. Surge (left graph) shows that acceptable agreement is found between CFD results and OpenFOAM ones, with the CFD surge equilibrium position slightly more downwind than OpenFOAM, respectively  $\sim 12.5\text{m}$  versus  $\sim 12\text{m}$ . Nonetheless, the amplitude motions have comparable values, meaning that the RAOs are similar. OpenFAST result is in accordance with the amplitudes, but with a significantly different equilibrium drifted position in the x direction, of roughly 7 meters in positive (downwind) direction. More accordance is found in pitch motion, shown in the right graph of Figure 5.22. Similar mean pitch inclinations are obtained between OpenFOAM and CFD reference results. More discrepancy is seen between the amplitudes (as it was for case2), where OpenFOAM overpredicts maximum and minimum pitch displacement. OpenFAST pitch results have a lower mean equilibrium position and an analogous amplitude range, similar to the trend found in surge.

To more precisely compare the motion response of the FOWT, **motion RAOs** for the three software are further evaluated. The motion (surge, pitch, and heave for case1) amplitudes are estimated by averaging the amplitudes within the steady-state results, that is the converged section from 200s onwards. For each motion amplitude, the local maxima and minima are extrapolated from the dataset. An example of this process for case3 is shown in Figure 5.23. These values are then normalized with the amplitude of the non-linear regular wave to obtain the response amplitude operator (RAO). The motion RAOs are determined for case 2 and case 3 for surge and pitch, while for case 1 for surge, pitch, and heave Figure 5.24. Employing motion RAOs is a smart and simple way to non-dimensionally compare the responses of the FOWT due to environmental forces. As explained in the background theory chapter (chapter 2, motion RAOs represents the response amplitude of the FOWT related to the external motion amplitude that caused the motion. The higher the motion RAOs are, the more extreme the FOWT motions are in relation to the external force, and consequently the FOWT gets closer to the resonance

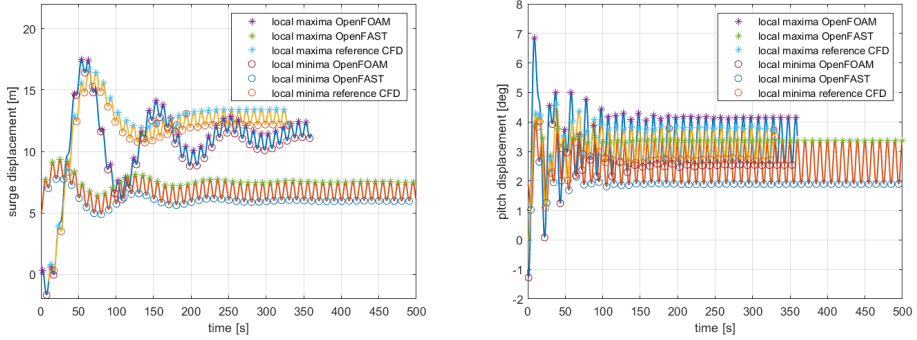


Figure 5.23: CASE3 FOWT motions extrapolation of local maxima and minima to determine motions RAOs

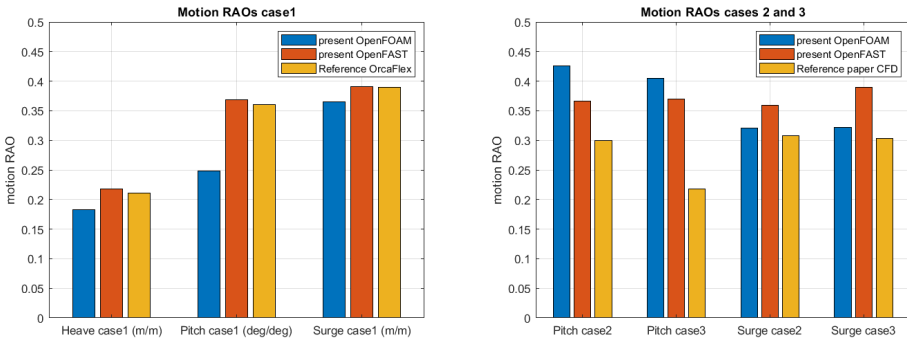


Figure 5.24: CASE3 FOWT motion RAOs. Left graph RAOs for case1. Right graph RAOs for cases2 and 3.

region of Figure 2.3. Indeed, surge and pitch RAOs for case1 are significantly lower than the RAOs of cases 2 and 3, even though the environmental conditions for case 1 are more extreme ( $H_s=6\text{m}$ ) than those of cases 2 and 3 (respectively  $H_s=3.66\text{m}$ ,  $H_s=4\text{m}$ ). This means that the design of OC4 FOWT has natural periods closer to the wave period of the case in which the motion RAO is the highest. From motion RAOs one can also extrapolate in which direction the FOWT is going to experience the highest responses, and consequently increase the damping or the stiffness in that translation/rotation direction avoiding materials from reaching the Ultimate Limit State ULS or incurring fatigue issues.

The same logical reasoning could also be applied to forces and moments, hence obtaining **load RAOs** for surge, sway, heave and **moment RAOs** for roll, pitch, and yaw. Also the mooring line tension can be visualised in terms of load RAOs, simplifying the comparison between different possible configurations. Load RAOs have  $kN/m$  as the unit of measurement (while motion RAOs have  $m/m$ ) since the load amplitude response of the FOWT ( $kN$ ) is normalized by the wave amplitude ( $m$ ). Comparing the load forces and moments RAOs for the three cases, in surge and heave direction for forces and in roll and

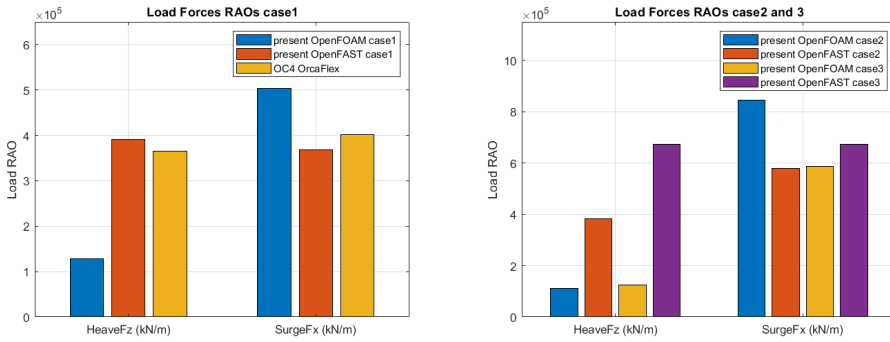


Figure 5.25: CASE3 FOWT load RAOs. The left graph force RAOs for case1. Right graph force RAOs for cases 2 and 3.

pitch direction for moments, the results presented in Figure 5.26 are obtained.

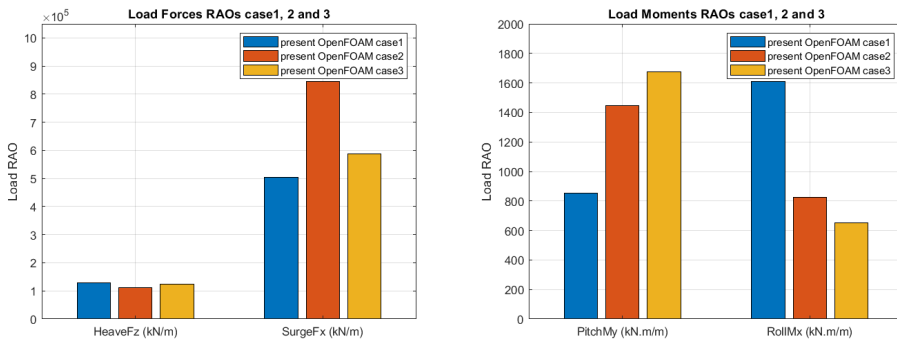


Figure 5.26: CASE3 FOWT load RAOs. The left graph force RAOs Fx and Fz for cases 1, 2, and 3. Right graph moments RAOs Mx and My for cases 1, 2, and 3.

As a conclusion from the motion and load RAOs comparison between the present study and reference results, good accordance as expected resulted between OrcaFlex and OpenFAST since both of them are mid-fidelity potential flow software. The differences instead with OpenFOAM results are the same as the ones highlighted for the time-domain graphs, but easier to interpret if represented in the form of RAOs. Good accordance is however found in motion RAOs (Figure 5.24) for case1 excluding pitch motion. For cases 2 and 3 pitch motion is overestimated, while surge motion RAO matches with reference CFD but slightly underpredicts OpenFAST outcomes. Considering load RAOs instead (Figure 5.25), all three cases behaved similarly by strongly underpredicting Fz and marginally overestimating Fx.



# 6

## CONCLUSIONS

This chapter marks the conclusion of the thesis. First, a recap of the work performed is presented, followed by a discussion of the research questions presented in Chapter 1. The chapter then concludes the work by presenting bits of advice and suggestions for future improvements and research projects.

### 6.1. THESIS SUMMARY

This thesis work has served to provide a high-fidelity CFD model for the simulation of FOWT. The project's main focus was the validation of the hydrodynamic part against benchmark results, leading to the creation of a reliable CFD model suitable for trustworthy future research studies. The model for FOWT simulations was developed in the free open-source software OpenFOAM. OpenFOAM is a C++ toolbox for the development of customized numerical solvers for the solution of continuum mechanics problems, most prominently including computational fluid dynamics (CFD). The wave generation/absorption is based on the waves2Foam library developed by Jacobsen [51]. The mooring line numerical modeling for giving additional stiffness to the FOWT is based on the DLL moorDyn and moody developed by Matthew Hall and Joannes Palm respectively.

The workflow of this thesis followed a sequential approach. First, in [chapter 2](#) a thorough study of the topic of floating offshore wind is performed. This initial background study is divided into two main sections: analytical theory and numerical theory. These include the theory of 6DOF rigid body motion and the theory of non-linear regular ocean waves, the numerical theory behind CFD, and state-of-the-art simulations of FOWT with detailed emphasis about OpenFOAM dynamic turbulent incompressible flow simulations. openFOAM numerical theory includes FVM for fluid spatial discretization, FEM for mooring spatial discretization, mesh morphing techniques for accommodating the motions of the FOWT in the FVM mesh, and mooring line modeling approaches.

After having acquired enough analytical and numerical background knowledge on FOWT topic, [chapter 3](#) presents some essential convergence studies results for key numerical parameters influencing the CFD simulations. The first parameter studied is the mesh size influence on a 2D symmetric numerical domain with a standing wave. Then 3 more parameters are studied in a 2D domain with relaxation zones for second-order Stokes waves: cell expansion ratio in the edges of the domain, relaxation zones length used by waves2Foam library for wave generation, and maximum pressure residuals for the PIMPLE iterations in OpenFOAM convergence. The choice of the "best" value for each of the parameters analyzed is based on both accuracy of the result generated compared to analytical results, and on the numerical resources (time and space) needed for completing the simulation.

On the basis of the results obtained in [chapter 3](#), in [chapter 4](#) a comparison of different numerical mooring line models is performed. Three different models are dynamically linked to OpenFOAM-v2012 and studied: quasi-static waves2FoamMooring model part of waves2Foam toolbox, lumped-mass spatially-discretized dynamic moor-Dyn model developed by Matthew Hall, and FEM spatially-discretized dynamic model moody developed by Joannes Palm. These three mooring models are applied to a floating box in a 3D numerical domain with second-order wave flume. The results obtained (anchor tension, fairlead tension, heave motion, and pitch motion) are compared with overset results and experimental results, giving some insight to the main differences between the three models.

Finally, in [chapter 5](#), all the lessons learned from the previous three chapters are applied to complete the FOWT system subjected to coupled wind and wave fields. The floater simulated is the OC4 semi-submersible with on top the 5MW NREL reference turbine for offshore applications. At first, free decay tests are performed and compared with the results obtained during the OC4 and OC5 campaigns. Natural periods and damping ratios in surge, sway, heave, and pitch are compared, giving preliminary results on the accuracy of the simulation setup, including platform values (COG, moments of inertia, mass, etc) and numerical domain parameters (mesh size, boundary conditions, etc). Additionally, in order to confirm the reason for some small discrepancies in the comparison with OC4 and OC5, free-decay tests in surge, heave, and pitch are performed and compared this time with OC6 high-fidelity results. Once the platform and the turbine are correctly tuned, the full dynamic simulations are performed. Three environmental cases for the waves and wind are chosen and the motions, line tensions, moments, and forces are compared and validated with literature high-fidelity and OpenFAST mid-fidelity results. This final chapter gives the overall results and validation of the developed high-fidelity CFD OpenFOAM model for fully coupled hydrodynamic simulations for FOWT.

## 6.2. ANSWER TO RESEARCH QUESTION

**Is it possible to reduce the computational time while keeping the accuracy of the simulations of a 2D Numerical Wave Tank (NWT) by performing convergence studies of some key numerical parameters?**

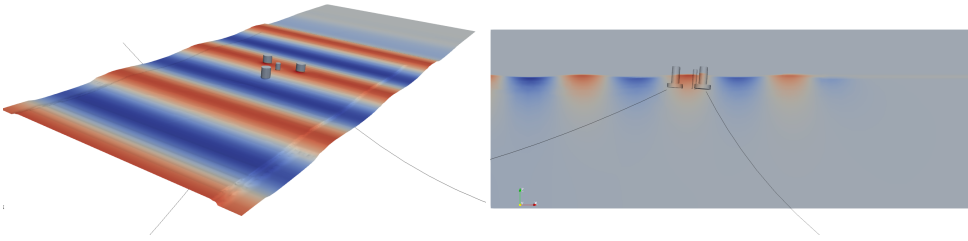


Figure 6.1: Case 3 flow dynamic pressure at  $t=60.0s$  side view and top view.

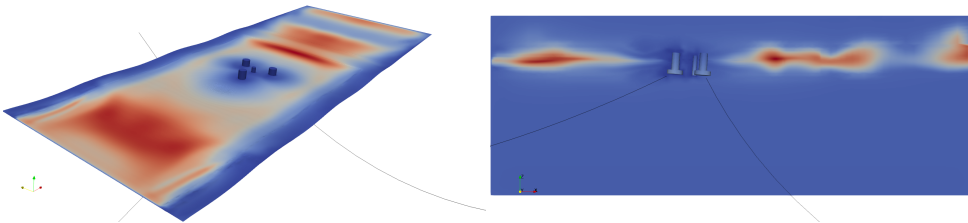


Figure 6.2: Case 3 turbulent eddy viscosity at  $t=60.0s$  side view and top view.

The first sub-research question is answered in [chapter 3](#) where a sensitivity study is performed on several parameters. The real answer lies in the following chapters [chapter 4](#) and [chapter 5](#), but it is noticed that through a convergence analysis some parameters showed more influence than others in the simulation results accuracy and time. The most influencing one was found to be the mesh size. The user in fact, through the usage of `blockMesh` and `snappyHexMesh` OpenFOAM utilities, can easily manipulate the accuracy of the simulation by simply changing the number of cells. By doing so, both the accuracy and computational time needed are strongly affected. Indeed, an optimal range of cells is found to be around 10 cph, with a correct spatial arrangement.

An additional parameter that is found to greatly influence the simulation of waves is the relaxation zone lengths. Indeed, `waves2Foam` toolbox effectiveness is dependent on the generation and even more on the absorption zone sizes. If the latter is too short (compared to the wavelength) then the waves are not properly damped, and some of the wave energy is reflected at the outlet boundary which consequently affects the wave height and period in the propagation zone. The optimal values considering time and accuracy are found to be one wavelength for the generation zone and two wavelengths for the absorption zone. On the other hand, other parameters turned out to have less influence on the overall simulation performance. The residuals for pressure values in the PIMPLE loop, even though from the theory of PIMPLE iterations they appear to play a critical role, in practice they do not influence time or accuracy.

**Can a lumped-mass and FEM dynamic numerical model for mooring lines be dynamically coupled with the two-phase OpenFOAM solver for hydrodynamic simulations?**

### **How does it compare with less accurate quasi-static mooring models in terms of accuracy of results and computational time and resources?**

The second sub-question is answered thoroughly in [chapter 4](#). An exhaustive comparison of three mooring lines is made by reproducing an experiment performed by Wu [90] and subsequent numerical simulations performed by Hall [10] in 2022 and by Dominguez [24] in 2019. A floating rectangular box is left floating, attached with four mooring lines to the bottom, under the influence of regular waves.

The answer to the first question is positive. Two dynamic mooring line models have been successfully dynamically linked to OpenFOAM, meaning that at each PIMPLE time step, the OpenFOAM simulation calls the external mooring library, performs the required calculations, and goes back to C++ OpenFOAM with the new calculated mooring values of tension and position. MoorDyn, a lumped-mass dynamic mooring model, is successfully dynamically coupled to OpenFOAM-v2012. The C++ library in which MoorDyn is coded is first compiled and then a dynamic link between the OpenFOAM solver `interDyMFoam` is generated to couple the two. Moody instead, a FEM dynamic mooring model, comes already precompiled and originally prototyped in Matlab, which then needs to be correctly copied from GitHub to OpenFOAM and linked with OpenFOAM-v2012. In addition, Moody comes with an API (Automated Program Interface) that can make the user capable of using the `postProcessing` utility, very useful for handling and filtering all the mooring results.

The comparison of Moody and MoorDyn was primarily meant to detect the differences between a dynamic model and a quasi-static one. Indeed, `waves2FoamMooring`, a quasi-static mooring model of `waves2Foam`, is employed as well and the results are compared with the two dynamic models. After performing the simulations, the box motions and mooring tensions were compared between the three models. The main outcome of this comparison is that while the two dynamic models behaved similarly, with barely any noticeable difference, the quasi-static model responded differently, and the time results of both box position and line tensions truly deviated from the experimental values. The reason for this large discrepancy was found to be the lower accuracy of the mooring model and the inability of the lines to take any bending or line-waves interaction into account using catenary equations.

As a result, the quasi-static `waves2FoamMooring` model was excluded from the following simulations while `moody` and `moorDyn` proved to be accurate enough. Additionally, the computational time needed for running the same simulation with a dynamic model did not increase at all, further supporting the choice of Moody and MoorDyn for successive numerical simulations. A concluding remark: the choice between Moody and MoorDyn is left to the user since the decision needs to be taken by carefully analyzing each case by case.

**How does the dynamically coupled OpenFOAM model behave when simulating full wind/wave simulations of FOWT? How do the CFD results obtained with OpenFOAM**

### compare with experimental, high-fidelity, and mid-fidelity potential-flow solvers results?

The last sub-question is concerned in [chapter 5](#). A complete analysis of the performance of the OpenFOAM model is accomplished by comparing several results between high-fidelity CFD software and mid-fidelity potential-flow software. Some discrepancies are spotted between all the outcomes and the possible reasons and improvements are investigated. Additionally, by simulating the FOWT response in varied environmental conditions, the model has been tested for both calm, mild, and rough conditions.

In conclusion of [chapter 5](#), because of the good overall agreement with the other solvers, the OpenFOAM model is successfully validated, considering it accurate enough and able to deliver reliable hydrodynamic results.

## 6.3. FINAL CONCLUSIONS AND FURTHER RESEARCH

This thesis provides validation against numerical and experimental results of a high-fidelity model developed in OpenFOAM-v2012. The research focussed on the validation of the hydrodynamics, mooring line, and aerodynamic effects on the FOWT. Validating the model involved the following steps: performing sensitivity studies on numerical parameters on which the simulation accuracy and convergence depend; improving the FOWT motion response by increasing the stiffness quality of the mooring line model from quasi-static to dynamic; conducting free-decay tests in static conditions (no wind, no waves, no current) to determine damping ratios and natural periods, useful parameters for design optimization; simulating the effects of aerodynamics on hydrodynamic motion and load responses of the FOWT by means of time-domain and RAOs results analysis.

This model is developed to perform fully coupled simulations of FOWT, and it serves as a starting point for further studies on the complex physical aerodynamics and hydrodynamics behavior of the floater substructure of a floating offshore turbine. The validation process can be now considered successfully concluded and the findings of [chapter 3](#), [chapter 4](#), and [chapter 5](#) give the reader a comprehensive understanding of the main limitations and the usefulness of the current model.

Given the lack of available open-source research regarding FOWT numerical simulations due to the fierce competition between few companies in the industry, some aspects have not been tested and compared yet. However, due to the fast developments and high investments in the floating sector coming from influential companies and research institutions, it is highly probable that in the coming years, much more data will be freely available in the literature, giving the possibility for further development and improvement of this OpenFOAM model. According to the author, some of the most important aspects on which future studies on the topic should be focussed include additional validation, framework optimization, design optimization, and model improvement.

- **Real-world environmental hydrodynamic simulations.** Even though extensive

validation against numerical and experimental results has been already performed in this thesis, several additional cases can be evaluated. For example simulate FOWT response under irregular waves following JONSWAP (Joint North Sea Wave Project) or Pierson-Moskowitz spectra, to analyze real-world environmental conditions. By performing 3h time-domain simulations, one can then focus on determining the standard statistical MPE values for motions and loads following Rayleigh distribution, which could then lead to some structural consideration regarding ULS analysis of critical parts.

- **Hydroelastic simulations.** A further step could include coupling the fluid dynamics model with computational structural mechanics software for structural analysis. Traditionally CSM software apply FEM discretization taking advantage of the complete framework, while CFD commonly use FVM technique. FEM-CFD coupling for partitioned high-fidelity fluid-structure interaction problems can be investigated, where the flow and structure are solved independently on two separate meshes with coupling achieved through communication on the shared boundaries. This method benefits from allowing for specialist fluid and solid codes to be exploited for the hydrodynamics and structural mechanics, respectively, but is solved sequentially at each time step. Hence, in principle, the partitioned approach is more computationally efficient than a monolithic approach, where the flow and structure are solved simultaneously within a single solver [58]. However, more recent monolithic approaches that use FVM in OpenFOAM for both the structural and fluid dynamics parts have been investigated by Cardiff et al in [8]. In this paper, Cardiff mentions that the official version of OpenFOAM already comes with the most basic solid mechanics solver tool `solidDisplacementFoam` which solves solids undergoing small strains and rotations. A new OpenFOAM FSI toolbox for large deformations has been developed by Cardiff in [8], Martinez in [63], Huang in [42], and Brown in [6]. This open-source toolbox for OpenFOAM called **solids4Foam** could be used for high-fidelity monolithic FSI hydroelastic problems involving FOWT.
- **Design optimization.** Since the main goal of this work was to prove that the model can give reliable, results, further studies could then focus on the next step, which is the optimization of the FOWT design. This can involve the comparison of different floater concepts and their effectiveness in limiting wind turbine motions and consequently optimizing the power output.
- **Overset mesh motion technique.** In this thesis mesh morphing technique for mesh motion is applied. This method is relatively simple to implement, and extremely efficient for small motion amplitudes. However, when the environmental conditions get too rough, and the FOWT motions increase, the morphing technique deforms the cells in such a way that the simulation fails due to time step divergence. In these cases, applying the overset meshing technique can improve the simulation stability and accuracy. [73] explains the prerequisites for coupling overset mesh with OpenFOAM and its characteristics. The overset motion technique indeed uses two overlaying meshes, one for the background (usually simple and a relatively linear and coarse mesh) and one for the moving body boundary (usually

more complex geometry and a very refined mesh to capture the non-linearities, such as high gradients). These two grids are overlapped, and they create the over-set mesh grid, an extremely useful way to resolve complex FSI phenomena in a more computationally efficient manner.



# BIBLIOGRAPHY

- [1] Andreas Bauer and Volker Springel. “Subsonic turbulence in smoothed particle hydrodynamics and moving-mesh simulations”. In: (Sept. 2011). DOI: [10.1111/j.1365-2966.2012.21058.x](https://doi.org/10.1111/j.1365-2966.2012.21058.x). URL: <http://arxiv.org/abs/1109.4413v2><http://dx.doi.org/10.1111/j.1365-2966.2012.21058.x>.
- [2] Roger Bergua et al. “OC6 project Phase III: validation of the aerodynamic loading on a wind turbine rotor undergoing large motion caused by a floating support structure”. In: *Wind Energy Science* 8.4 (Apr. 2023), pp. 465–485. ISSN: 2366-7451. DOI: [10.5194/wes-8-465-2023](https://doi.org/10.5194/wes-8-465-2023). URL: <https://wes.copernicus.org/articles/8/465/2023/>.
- [3] Bo Terp Paulsen. “Efficient computations of wave loads on offshore structures”. PhD thesis. Copenhagen: DTU, Aug. 2013, pp. 1–127.
- [4] M. Borg and M. Collu. “A comparison between the dynamics of horizontal and vertical axis offshore floating wind turbines”. In: *Philosophical Transactions of the Royal Society A: Mathematical, Physical and Engineering Sciences* 373.2035 (Feb. 2015). ISSN: 1364503X. DOI: [10.1098/rsta.2014.0076](https://doi.org/10.1098/rsta.2014.0076).
- [5] Henrik Bredmose. *General rights Ringing and impulsive excitation from steep and breaking waves Results from the Wave Loads project*. Tech. rep.
- [6] S. A. Brown et al. “Investigation of wave-driven hydroelastic interactions using numerical and physical modelling approaches”. In: *Applied Ocean Research* 129 (Dec. 2022). ISSN: 01411187. DOI: [10.1016/j.apor.2022.103363](https://doi.org/10.1016/j.apor.2022.103363).
- [7] Thesis N Bruinsma. *Validation and Application of a Fully Nonlinear Numerical Wave Tank*. Tech. rep. 2016.
- [8] P. Cardiff et al. “An open-source finite volume toolbox for solid mechanics and fluid-solid interaction simulations”. In: (Aug. 2018). URL: <http://arxiv.org/abs/1808.10736>.
- [9] S.K. Chakrabarti. *Hydrodynamics of Offshore Structures*. Offshore Structure Analysis Inc, USA, 1994.
- [10] Haifei Chen and Matthew Hall. “CFD simulation of floating body motion with mooring dynamics: Coupling MoorDyn with OpenFOAM”. In: *Applied Ocean Research* 124 (July 2022). ISSN: 01411187. DOI: [10.1016/j.apor.2022.103210](https://doi.org/10.1016/j.apor.2022.103210).
- [11] Hao Chen et al. “Application of an overset mesh based numerical wave tank for modelling realistic free-surface hydrodynamic problems”. In: *Ocean Engineering* 176 (Mar. 2019), pp. 97–117. ISSN: 00298018. DOI: [10.1016/j.oceaneng.2019.02.001](https://doi.org/10.1016/j.oceaneng.2019.02.001).

- [12] Hao Chen et al. “Application of an overset mesh based numerical wave tank for modelling realistic free-surface hydrodynamic problems”. In: *Ocean Engineering* 176 (Mar. 2019), pp. 97–117. ISSN: 00298018. DOI: [10.1016/j.oceaneng.2019.02.001](https://doi.org/10.1016/j.oceaneng.2019.02.001).
- [13] Ping Cheng, Yang Huang, and Decheng Wan. “A numerical model for fully coupled aero-hydrodynamic analysis of floating offshore wind turbine”. In: *Ocean Engineering* 173 (Feb. 2019), pp. 183–196. ISSN: 00298018. DOI: [10.1016/j.oceaneng.2018.12.021](https://doi.org/10.1016/j.oceaneng.2018.12.021).
- [14] Ping Cheng, Yang Huang, and Decheng Wan. “A numerical model for fully coupled aero-hydrodynamic analysis of floating offshore wind turbine”. In: *Ocean Engineering* 173 (Feb. 2019), pp. 183–196. ISSN: 00298018. DOI: [10.1016/j.oceaneng.2018.12.021](https://doi.org/10.1016/j.oceaneng.2018.12.021).
- [15] Günther Clauss, Eike Lehmann, and Carsten Östergaard. *Offshore Structures*. London: Springer London, 1992. ISBN: 978-1-4471-3195-3. DOI: [10.1007/978-1-4471-3193-9](https://doi.org/10.1007/978-1-4471-3193-9). URL: <http://link.springer.com/10.1007/978-1-4471-3193-9>.
- [16] Alexander J. Coulling et al. “Validation of a FAST semi-submersible floating wind turbine numerical model with DeepCwind test data”. In: *Journal of Renewable and Sustainable Energy*. Vol. 5. 2. Mar. 2013. DOI: [10.1063/1.4796197](https://doi.org/10.1063/1.4796197).
- [17] Global Wind Energy Council. “GWEC | GLOBAL WIND REPORT 2022”. In: (Apr. 2022). URL: [https://gwec.net/wp-content/uploads/2022/04/Annual-Wind-Report-2022\\_screen\\_final\\_April.pdf](https://gwec.net/wp-content/uploads/2022/04/Annual-Wind-Report-2022_screen_final_April.pdf).
- [18] Global Wind Energy Council. *GWEC|GLOBAL OFFSHORE WIND REPORT 2022*. Tech. rep. Apr. 2022. URL: [https://gwec.net/wp-content/uploads/2022/06/GWEC-Offshore-2022\\_update.pdf](https://gwec.net/wp-content/uploads/2022/06/GWEC-Offshore-2022_update.pdf).
- [19] Josh Davidson and John V. Ringwood. *Mathematical modelling of mooring systems for wave energy converters - A review*. May 2017. DOI: [10.3390/en10050666](https://doi.org/10.3390/en10050666).
- [20] Josh Davidson et al. *Dynamic mesh motion in OpenFOAM for wave energy converter simulation Neural control of blood pressure using nonlinear feedback models View project NumSiSSI View project Dynamic mesh motion in OpenFOAM for wave energy converter simulation*. Tech. rep. 2019. URL: <https://www.researchgate.net/publication/334615556>.
- [21] R. G. Dean. “Stream function representation of nonlinear ocean waves”. In: *Journal of Geophysical Research* 70.18 (Sept. 1965), pp. 4561–4572. DOI: [10.1029/jz070i018p04561](https://doi.org/10.1029/jz070i018p04561).
- [22] G Decorte et al. *Waves-Structure Interaction A first Assessment of the Interdependency of Mesh Motion and Free Surface Models in Open-FOAM Regarding Wave-Structure Interaction A FIRST ASSESSMENT OF THE INTERDEPENDENCY OF MESH MOTION AND FREE SURFACE MODELS IN OPENFOAM REGARDING WAVE-STRUCTURE INTERACTION*. Tech. rep. 2019. URL: <http://bwk.kuleuven.be/hydr>.
- [23] DNV AS. *RECOMMENDED PRACTICE Environmental conditions and environmental loads*. Tech. rep. 2019.

- [24] José M. Domínguez et al. “SPH simulation of floating structures with moorings”. In: *Coastal Engineering* 153 (Nov. 2019). ISSN: 03783839. DOI: [10.1016/j.coastaleng.2019.103560](https://doi.org/10.1016/j.coastaleng.2019.103560).
- [25] Claes Eskilsson and Johannes Palm. “High-fidelity modelling of moored marine structures: multi-component simulations and fluid-mooring coupling”. In: *Journal of Ocean Engineering and Marine Energy* 8.4 (Nov. 2022), pp. 513–526. ISSN: 21986452. DOI: [10.1007/s40722-022-00263-w](https://doi.org/10.1007/s40722-022-00263-w).
- [26] Green Giraffe EU. *The energy transition financial advisors*. URL: <https://green-giraffe.eu/>.
- [27] Wind Europe. “FLOATING OFFSHORE WIND ENERGY A POLICY BLUEPRINT FOR EUROPE”. In: (Oct. 2018). URL: <https://windeurope.org/policy/position-papers/floating-offshore-wind-energy-a-policy-blueprint-for-europe/#:~:text=Floating%20offshore%20wind%20energy:%20a%20policy%20blueprint%20for,projects%20at%20different%20stages%20of%20development%20worldwide%20today..>
- [28] Wind Europe. *Floating Offshore Wind Vision Statement*. Tech. rep. June 2017. URL: <https://windeurope.org/about-wind/reports/floating-vision-statement/#:~:text=Floating%20offshore%20Wind%20Vision%20Statement%20Floating%20offshore%20Wind,seas,%20where%20traditional%20BFOW%20is%20not%20economically%20attractive..>
- [29] Wind Europe. *Offshore Wind in Europe, Key trends and statistics 2019*. Tech. rep. Feb. 2020. URL: <https://windeurope.org/wp-content/uploads/files/about-wind/statistics/WindEurope-Annual-Offshore-Statistics-2019.pdf>.
- [30] Wind Europe. “Wind energy in Europe 2021 Statistics and the outlook for 2022–2026”. In: (Feb. 2022). URL: <https://windeurope.org/intelligence-platform/product/wind-energy-in-europe-2021-statistics-and-the-outlook-for-2022-2026/>.
- [31] O Faltinsen. *Sea Loads on Ships and Offshore Structures*. Cambridge, 1993.
- [32] David R. Fuhrman, Per A. Madsen, and Harry B. Bingham. “Numerical simulation of lowest-order short-crested wave instabilities”. In: *Journal of Fluid Mechanics* 563 (Sept. 2006), pp. 415–441. ISSN: 14697645. DOI: [10.1017/S0022112006001236](https://doi.org/10.1017/S0022112006001236).
- [33] Andreu Oliver González et al. *Mesh motion alternatives in OpenFOAM CFD with OpenSource Software, Assignment 3*. Tech. rep. 2009.
- [34] Matthew Hall. *MoorDyn User’s Guide*. Tech. rep. 2017. URL: <https://nwtc.nrel.gov/FAST8>.
- [35] Matthew Hall. *MoorDyn User’s Guide*. Tech. rep. 2017. URL: <https://nwtc.nrel.gov/FAST8>.
- [36] Matthew Hall, Brad Buckham, and Curran Crawford. “Evaluating the importance of mooring line model fidelity in floating offshore wind turbine simulations”. In: *Wind Energy* 17.12 (Dec. 2014), pp. 1835–1853. ISSN: 10991824. DOI: [10.1002/we.1669](https://doi.org/10.1002/we.1669).

- [37] Matthew Hall and Andrew Goupee. “Validation of a lumped-mass mooring line model with DeepCwind semisubmersible model test data”. In: *Ocean Engineering* 104 (June 2015), pp. 590–603. ISSN: 00298018. DOI: [10.1016/j.oceaneng.2015.05.035](https://doi.org/10.1016/j.oceaneng.2015.05.035).
- [38] C W Hirt and B D Nichols. *Volume of Fluid (VOF) Method for the Dynamics of Free Boundaries\**. Tech. rep. 1981, pp. 201–225.
- [39] Karsten Hochkirch. *On the Importance of Full-Scale CFD Simulations for Ships*. Tech. rep.
- [40] Leo H Holthuijsen. *Wave in oceanic and coastal waters*. Cambridge, 2007.
- [41] Tobias Holzmann. “NumericsAndOpenFOAMv7\_limited”. In: (2019).
- [42] Luofeng Huang et al. “CFD with OpenSource software An opensource solver for wave-induced FSI problems”. In: (). DOI: [10.17196/OS\\_{\\\_}CFD{\\\_}#\\_{\\\_}YEAR{\\\_}2017](https://doi.org/10.17196/OS_{\_}CFD{\_}#_{\_}YEAR{\_}2017). URL: [http://dx.doi.org/10.17196/OS\\_CFD#YEAR\\_2017](http://dx.doi.org/10.17196/OS_CFD#YEAR_2017).
- [43] Wei Hua Huang and Ray Yeng Yang. “Water depth variation influence on the mooring line design for fowt within shallow water region”. In: *Journal of Marine Science and Engineering* 9.4 (Apr. 2021). ISSN: 20771312. DOI: [10.3390/jmse9040409](https://doi.org/10.3390/jmse9040409).
- [44] Fons Huijs, Rogier De Bruijn, and Feike Savenije. “Concept design verification of a semi-submersible floating wind turbine using coupled simulations”. In: *Energy Procedia*. Vol. 53. C. Elsevier Ltd, 2014, pp. 2–12. DOI: [10.1016/j.egypro.2014.07.210](https://doi.org/10.1016/j.egypro.2014.07.210).
- [45] Fons Huijs, Erik-Jan De Ridder, and Feike Savenije. *COMPARISON OF MODEL TESTS AND COUPLED SIMULATIONS FOR A SEMI-SUBMERSIBLE FLOATING WIND TURBINE*. Tech. rep. 2014. URL: <http://www.asme.org/about-asme/terms-of-use>.
- [46] IEA. “Global Energy and Climate Model”. In: (Dec. 2022). URL: <https://iea.blob.core.windows.net/assets/2db1f4ab-85c0-4dd0-9a57-32e542556a49/GlobalEnergyandClimateModelDocumentation2022.pdf>.
- [47] IEA. *IEA Wind TCP Task 31*. URL: <https://iea-wind.org/task31/>.
- [48] IEA. *Offshore Wind Outlook 2019*. Tech. rep. Nov. 2019. URL: [https://iea.blob.core.windows.net/assets/495ab264-4ddf-4b68-b9c0-514295ff40a7/Offshore\\_Wind\\_Outlook\\_2019.pdf](https://iea.blob.core.windows.net/assets/495ab264-4ddf-4b68-b9c0-514295ff40a7/Offshore_Wind_Outlook_2019.pdf).
- [49] IEA. “World Energy Outlook 2022”. In: (2022). URL: <https://www.iea.org/reports/world-energy-outlook-2022>.
- [50] *INWIND.EU*. 2013. URL: <http://www.innwind.eu/>.
- [51] Niels Gjøel Jacobsen. *waves2Foam Manual Generating waves for OpenFoam: waves2Foam View project JIP WiFi View project*. Tech. rep. 2012. URL: [www.openfoam.com](http://www.openfoam.com),.
- [52] Hrvoje Jasak. “Dynamic mesh handling in OpenFOAM”. In: *47th AIAA Aerospace Sciences Meeting including the New Horizons Forum and Aerospace Exposition*. American Institute of Aeronautics and Astronautics Inc., 2009. ISBN: 9781563479694. DOI: [10.2514/6.2009-341](https://doi.org/10.2514/6.2009-341).

- [53] J Jonkman et al. *Definition of a 5-MW Reference Wind Turbine for Offshore System Development*. Tech. rep. 2009. URL: <http://www.osti.gov/bridge>.
- [54] J Jonkman et al. *Definition of a 5-MW Reference Wind Turbine for Offshore System Development*. Tech. rep. 2009. URL: <http://www.osti.gov/bridge>.
- [55] J M J Journée, W W Massie, and R H M Huijsmans. *OFFSHORE HYDROMECHANICS Third Edition (2015) Based on Original Lecture Notes (2000) by*. Tech. rep.
- [56] Madjid Karimirad. *Madjid Karimirad Stochastic Dynamic Response Analysis of Spar-Type Wind Turbines with Catenary or Taut Mooring Systems Stochastic Dynamic Response Analysis of Spar-Type Wind Turbines with Catenary or Taut Mooring Systems Stochastic Dynamic Response Analysis of Spar-Type Wind Turbines with Catenary or Taut Mooring Systems Stochastic Dynamic Response Analysis of Spar-Type Wind Turbines with Catenary or Taut Mooring Systems*. 2011. ISBN: 9788247125267.
- [57] Madjid Karimirad. *Offshore Energy Structures*. Springer International Publishing, 2014. DOI: [10.1007/978-3-319-12175-8](https://doi.org/10.1007/978-3-319-12175-8).
- [58] C. Kassiotis, A. Ibrahimbegovic, and H. Matthies. “Partitioned solution to fluid-structure interaction problem in application to free-surface flows”. In: *European Journal of Mechanics, B/Fluids* 29.6 (Nov. 2010), pp. 510–521. ISSN: 09977546. DOI: [10.1016/j.euromechflu.2010.07.003](https://doi.org/10.1016/j.euromechflu.2010.07.003).
- [59] by Ken Huang and Ming-Yao Lee. *OTC 8770 Experiences in Classification of Deep-water Mooring Systems for Floating Installations*. Tech. rep. 1998, pp. 4–7. URL: <http://onepetro.org/OTCONF/proceedings-pdf/980TC/A11-980TC/OTC-8770-MS/1935035/otc-8770-ms.pdf/1>.
- [60] B Le Mehaute. *An introduction to hydrodynamics and water waves*. New York: Springer, 1976.
- [61] Yuanchuan Liu et al. “Establishing a fully coupled CFD analysis tool for floating offshore wind turbines”. In: *Renewable Energy* 112 (2017), pp. 280–301. ISSN: 18790682. DOI: [10.1016/j.renene.2017.04.052](https://doi.org/10.1016/j.renene.2017.04.052).
- [62] Kai-Tung Ma et al. “Mooring analysis”. In: *Mooring System Engineering for Offshore Structures*. Elsevier, 2019, pp. 85–114. DOI: [10.1016/b978-0-12-818551-3.00005-3](https://doi.org/10.1016/b978-0-12-818551-3.00005-3).
- [63] Pedro J. Martínez-Ferrer et al. “An efficient finite-volume method to study the interaction of two-phase fluid flows with elastic structures”. In: *Journal of Fluids and Structures* 83 (Nov. 2018), pp. 54–71. ISSN: 10958622. DOI: [10.1016/j.jfluidstructs.2018.08.019](https://doi.org/10.1016/j.jfluidstructs.2018.08.019).
- [64] M Masciola et al. “Assessment of the Importance of Mooring Dynamics on the Global Response of the DeepCwind Floating Semisubmersible Offshore Wind Turbine”. In: (Jan. 2013).
- [65] Denis Matha, Uwe Fechter, and Martin Kuhn. “Non-Linear Multi-Body mooring system model for floating offshore wind turbines”. In: *EWEA Offshore* (2011).
- [66] F Moukalled, L Mangani, and M Darwish. *Fluid Mechanics and Its Applications The Finite Volume Method in Computational Fluid Dynamics*. Tech. rep. 2016. URL: <http://www.springer.com/series/5980>.

- [67] NREL. *2022 Standard Scenarios Report: A U.S. Electricity Sector Outlook*. Tech. rep. 2022. URL: <https://www.nrel.gov/docs/fy23osti/84327.pdf>.
- [68] OpenFOAM. 2022. URL: <https://www.openfoam.com/>.
- [69] “OpenFOAM user-guide”. In: (). URL: <https://www.openfoam.com/documentation/user-guide/6-solving/6.3-solution-and-algorithm-control>.
- [70] Bruno Paduano et al. “Experimental validation and comparison of numerical models for the mooring system of a floating wave energy converter”. In: *Journal of Marine Science and Engineering* 8.8 (Aug. 2020). ISSN: 20771312. DOI: [10.3390/JMSE8080565](https://doi.org/10.3390/JMSE8080565).
- [71] Johannes Palm and Claes Eskilsson. *USER MANUAL version 2.0.1*. Tech. rep. 2019.
- [72] S V Patankar and D B Spalding. *A CALCULATION PROCEDURE FOR HEAT, MASS AND MOMENTUM TRANSFER IN THREE-DIMENSIONAL PARABOLIC FLOWS*. Tech. rep. 1972, pp. 1787–1806.
- [73] Tisovska Petra and Constantin Sula Muye Ge. “CFD with OpenSource software Description of the overset mesh approach in ESI version of OpenFOAM”. In: (). DOI: [10.17196/OS\\_CFD\\_YEAR\\_2019](https://doi.org/10.17196/OS_CFD_YEAR_2019). URL: [http://dx.doi.org/10.17196/OS\\_CFD\\_YEAR\\_2019](http://dx.doi.org/10.17196/OS_CFD_YEAR_2019).
- [74] Romain Pinguet. “Hydrodynamics of semi-submersible floater for offshore wind turbines in highly nonlinear waves using Computational Fluid Dynamics (CFD), and validation of overset meshing technique in a numerical wave tank”. PhD thesis. Marseille: ECOLE CENTRALE de MARSEILLE, 2021.
- [75] National Renewable Energy Laboratory. *OpenFAST Documentation Release v2.5.0 National Renewable Energy Laboratory*. Tech. rep. 2021.
- [76] Marc Costa Ros Rhodri James. *Floating Offshore Wind: Market and Technology Review*. Tech. rep. Carbon Trust, 2015. URL: <https://ctprodstorageaccount.blob.core.windows.net/prod-drupal-files/documents/resource/public/Floating%20offshore%20Wind%20Market%20Technology%20Review%20-%20REPORT.pdf>.
- [77] A Robertson et al. *Offshore Code Comparison Collaboration, Continuation: Phase II Results of a Floating Semisubmersible Wind System: Preprint*. Tech. rep. 2013. URL: [www.nrel.gov/publications](http://www.nrel.gov/publications).
- [78] Amy Robertson et al. *OC6 Phase Ia Definition Document: Validation of Nonlinear Hydrodynamic Loading on the DeepCwind Semisubmersible*. Tech. rep. 2017. URL: <https://www.nrel.gov/docs/fy22osti/80803.pdf>.
- [79] Amy N. Robertson et al. “OC5 Project Phase II: Validation of Global Loads of the DeepCwind Floating Semisubmersible Wind Turbine”. In: *Energy Procedia*. Vol. 137. Elsevier Ltd, 2017, pp. 38–57. DOI: [10.1016/j.egypro.2017.10.333](https://doi.org/10.1016/j.egypro.2017.10.333).
- [80] Henrick Rusche. “Henrik\_Rusche-2003-PhD-Thesis”. In: ().
- [81] SALOME. URL: <https://www.salome-platform.org/>.
- [82] Turgut Sarpkaya. *Mechanics of Wave Forces on Offshore Structures*. 2010.

- [83] SIMSCALE CAE Forum. 2018. URL: <https://www.simscale.com/forum/t/cfd-pimple-algorithm/81418>.
- [84] Thanh Toan Tran and Dong Hyun Kim. “Fully coupled aero-hydrodynamic analysis of a semi-submersible FOWT using a dynamic fluid body interaction approach”. In: *Renewable Energy* 92 (July 2016), pp. 244–261. ISSN: 18790682. DOI: [10.1016/j.renene.2016.02.021](https://doi.org/10.1016/j.renene.2016.02.021).
- [85] Thanh Toan Tran and Dong Hyun Kim. “The coupled dynamic response computation for a semi-submersible platform of floating offshore wind turbine”. In: *Journal of Wind Engineering and Industrial Aerodynamics* 147 (Dec. 2015), pp. 104–119. ISSN: 01676105. DOI: [10.1016/j.jweia.2015.09.016](https://doi.org/10.1016/j.jweia.2015.09.016).
- [86] UNFCCC. *The Paris Agreement*. URL: <https://unfccc.int/process-and-meetings/the-paris-agreement/the-paris-agreement>.
- [87] Lu Wang et al. “OC6 phase I: Improvements to the OpenFAST predictions of non-linear, low-frequency responses of a floating offshore wind turbine platform”. In: *Renewable Energy* 187 (Mar. 2022), pp. 282–301. ISSN: 18790682. DOI: [10.1016/j.renene.2022.01.053](https://doi.org/10.1016/j.renene.2022.01.053).
- [88] Lu Wang et al. “OC6 Phase Ib: Validation of the CFD predictions of difference-frequency wave excitation on a FOWT semisubmersible”. In: *Ocean Engineering* 241 (Dec. 2021). ISSN: 00298018. DOI: [10.1016/j.oceaneng.2021.110026](https://doi.org/10.1016/j.oceaneng.2021.110026).
- [89] Christian Windt et al. “On the assessment of numerical wave makers in CFD simulations”. In: *Journal of Marine Science and Engineering* 7.2 (2019). ISSN: 20771312. DOI: [10.3390/JMSE7020047](https://doi.org/10.3390/JMSE7020047).
- [90] Minghao Wu et al. “Experimental study of a moored floating oscillating water column wave-energy converter and of a moored cubic box”. In: *Energies* 12.10 (2019). ISSN: 19961073. DOI: [10.3390/en12101834](https://doi.org/10.3390/en12101834).
- [91] Wenchao Zhao and Decheng Wan. *Numerical Study of Interactions Between Phase II of OC4 Wind Turbine and Its Semi-Submersible Floating Support System*. Tech. rep. 1. 2015, pp. 45–53. URL: <http://www.isope.org/publications>.



# A

## MOORING LINE INPUT FILES

```

MoorDyn v1 input file for a moored floating box
FALSE Echo - echo the input file data (flag)
-----
LINE DICTIONARY
-----
LineType  Diam    MassDenInAir  EA    BA/-zeta    Can    Cat    Cdn    Cdt
(-)      (m)      (kg/m)      (N)    (Pa-s/-)    (-)    (-)    (-)    (-)
main    0.003656  0.0607      29     -0.8        1.0    0.0    1.6    0.05
-----
NODE PROPERTIES
-----
Node      Type    X          Y          Z          M          V          FX          FY          FZ          CdA    CA
(-)      (-)    (m)      (m)      (m)      (kg)      (m^3)     (kN)     (kN)     (kN)     (m^2)  (-)
1        Fix    -1.385    0.423    -0.5      0          0          0          0          0          0      0
2        Fix    -1.385    -0.423   -0.5      0          0          0          0          0          0      0
3        Fix    1.385     0.423    -0.5      0          0          0          0          0          0      0
4        Fix    1.385     -0.423   -0.5      0          0          0          0          0          0      0
5        Vessel -0.100    0.100    -0.0736   0          0          0          0          0          0      0
6        Vessel -0.100    -0.100   -0.0736   0          0          0          0          0          0      0
7        Vessel 0.100     0.100    -0.0736   0          0          0          0          0          0      0
8        Vessel 0.100     -0.100   -0.0736   0          0          0          0          0          0      0
-----
LINE PROPERTIES
-----
Line      LineType  UnstrLen  NumSegs   NodeAnch  NodeFair  Flags/Outputs
(-)      (-)      (m)      (-)      (-)      (-)      (-)
1        main     1.455    40        1         5         p
2        main     1.455    40        2         6         p
3        main     1.455    40        3         7         p
4        main     1.455    40        4         8         p
-----
SOLVER OPTIONS
-----
0.00002  dtM      - time step to use in mooring integration
0        WaveKin  - wave kinematics flag (0=neglect, the only option currently supported)
3.0e6    kBot     - bottom stiffness
3.0e5    cBot     - bottom damping
0.5      WtrDpth  - water depth
5        TmaxIC   - maximum simulation time to allow for IC generation without convergence
5.0      CdScaleIC - factor by which to scale drag coefficients during dynamic relaxation IC gen
0.001    threshIC - threshold for IC convergence
-----
OUTPUTS
-----
FairTen1
FairTen3
AnchTen1
AnchTen3
----- need this line -----

```

Figure A.1: MoorDyn input file: OpenFOAM case folder/Mooring

## Moody model file for 4 catenary chains

```
dimensionNumber = 3;
waterLevel = 0;           % [m]           z-coordinate of mean water level
waterDensity = 1000.0;    % [kg/m??]   Density of water
airDensity = 1.0;        % [kg/m??]   Density of air
gravity = 1;

time.start = 0;
```

Unable to perform assignment because dot indexing is not supported for variables of this type.

```
time.end = 30;
time.cfl = 0.9;
time.scheme = 'RK3';

print.dt = 0.02; % output interval.
```

## extra quadpoints used for increased ground contact performance.

it makes the difference between stable and non-stable results.

```
numLib.qPointsAdded = 10;
%----- Ground model input -----%
ground.type = 'springDampGround';
ground.level = -0.5;
ground.dampingCoeff = 1.0;
ground.frictionCoeff = 0.1;
ground.vc = 0.01;
ground.stiffness = 300.0e6;

%----- Type definition -----%
cableType1.diameter = 0.003656;
cableType1.gamma0 = 0.0607;
cableType1.CDn = 1.6;
cableType1.CDt = 0.05;
cableType1.CMn = 2.0;
cableType1.materialModel.type = 'bilinear';
cableType1.materialModel.EA = 29;

%----- Geometry -----%
% note that unconnected vertices are ignored.
vertexLocations = {
    1  [-1.385  0.423  -0.5  ];
    2  [-0.1   0.1    -0.0736];
    3  [-1.385 -0.423  -0.5  ];
    4  [-0.1  -0.1   -0.0736];
    5  [ 1.385  0.423  -0.5  ];
    6  [ 0.1   0.1   -0.0736];
    7  [ 1.385 -0.423  -0.5  ];
    8  [ 0.1  -0.1   -0.0736];
};

%----- Object definitions -----%
```

```

cable1.typeNumber = 1;
cable1.startVertex = 1; %
cable1.endVertex = 2; %
cable1.length = 1.455; %
cable1.IC.type = 'CatenaryStatic';
cable1.N = 10; %
% Copy remaining info from cable1. short hand
cable2=cable1;
cable2.startVertex = 3;
cable2.endVertex = 4;
%
cable3=cable1;
cable3.startVertex = 5;
cable3.endVertex = 6;
%
cable4=cable1;
cable4.startVertex = 7;
cable4.endVertex = 8;

%----- Boundary conditions -----%
% Four anchors defined by vertexLocations
bc1.vertexNumber = 1;
bc1.type = 'dirichlet';
bc1.mode = 'fixed';
%
bc2=bc1;
bc2.vertexNumber = 3;
%
bc3=bc1;
bc3.vertexNumber = 5;
%
bc4=bc1;
bc4.vertexNumber = 7;

bc5.vertexNumber = 2;
bc5.type = 'dirichlet';
bc5.mode = 'externalPoint';

bc6=bc5;
bc6.vertexNumber = 4;

bc7=bc5;
bc7.vertexNumber = 6;

bc8=bc5;
bc8.vertexNumber = 8;

% --- API connectivity --- %
API.bcNames = {'bc5', 'bc6', 'bc7', 'bc8'};
API.reboot= 'no';
API.syncOutput = 1;
API.staggerTimeFraction= 0.5;
API.output = 'Mooring/results';
% ===== END OF FILE ===== %

```

Figure A.2: Moody input file: OpenFOAM case folder/Mooring

```

g (0 0 -9.8065);

    restraints
    {
    catenaryLine1
    {
        sixDoFRigidBodyMotionRestraint mooringLine;
        anchor      (-1.385 0.423 -0.5); // Anchor point, where the line is attached to an immovable object
        refAttachmentPt  (-0.100 0.100 -0.0736); // Reference point of attachment to the solid body
        massPerLength  0.0607; // Mass per unit length
        lineLength     2; // Length of the mooring line
        gravityVector   $g; // Gravity vector
        thickness       0.1; // Line thickness, used only for visualization purposes
    }
    catenaryLine2
    {
        sixDoFRigidBodyMotionRestraint mooringLine;
        anchor      (-1.385 -0.423 -0.5); // Anchor point, where the line is attached to an immovable object
        refAttachmentPt  (-0.100 -0.100 -0.0736); // Reference point of attachment to the solid body
        massPerLength  0.0607; // Mass per unit length
        lineLength     2; // Length of the mooring line
        gravityVector   $g; // Gravity vector
        thickness       0.1; // Line thickness, used only for visualization purposes
    }
    catenaryLine3
    {
        sixDoFRigidBodyMotionRestraint mooringLine;
        anchor      (1.385 0.423 -0.5); // Anchor point, where the line is attached to an immovable object
        refAttachmentPt  (0.100 0.100 -0.0736); // Reference point of attachment to the solid body
        massPerLength  0.0607; // Mass per unit length
        lineLength     2; // Length of the mooring line
        gravityVector   $g; // Gravity vector
        thickness       0.1; // Line thickness, used only for visualization purposes
    }
    catenaryLine4
    {
        sixDoFRigidBodyMotionRestraint mooringLine;
        anchor      (1.385 -0.423 -0.5); // Anchor point, where the line is attached to an immovable object
        refAttachmentPt  (0.100 -0.100 -0.0736); // Reference point of attachment to the solid body
        massPerLength  0.0607; // Mass per unit length
        lineLength     2; // Length of the mooring line
        gravityVector   $g; // Gravity vector
        thickness       0.1; // Line thickness, used only for visualization purposes
    }
    }
}

```

Figure A.3: Waves2FoamMooring input file: OpenFoam case folder/constant/dynamic-MeshDict



# B

## ADDITIONAL RESULTS CHAPTER 4

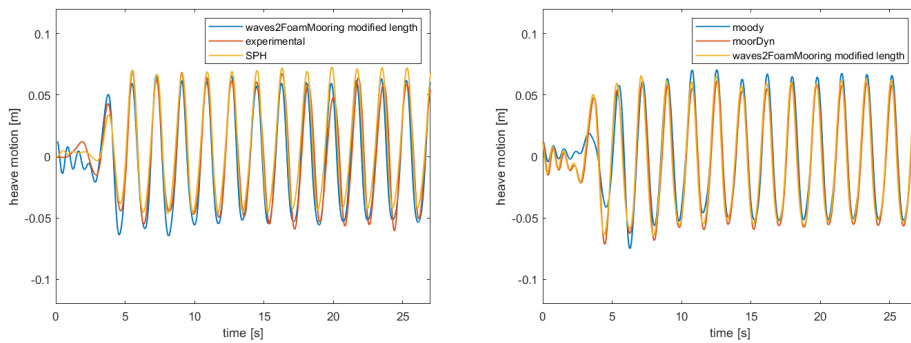


Figure B.1: Additional result comparing heave motion between waves2FoamMooring model with adjusted length, experimental, and SPH

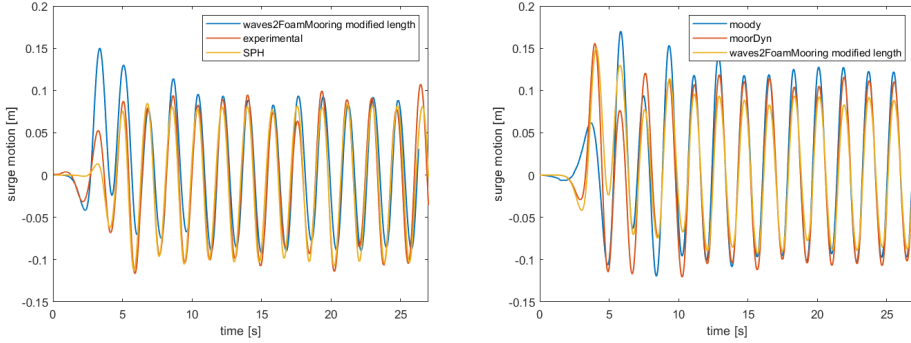


Figure B.2: Additional result comparing surge motion between waves2FoamMooring model with adjusted length, experimental, and SPH

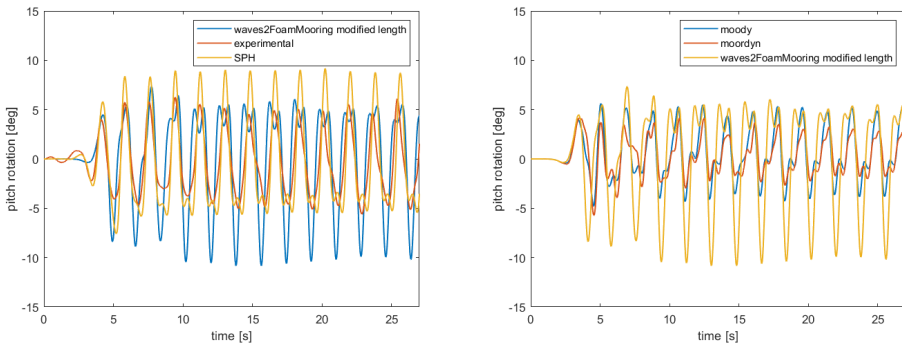


Figure B.3: Additional result comparing pitch rotation between waves2FoamMooring model with adjusted length, experimental, and SPH

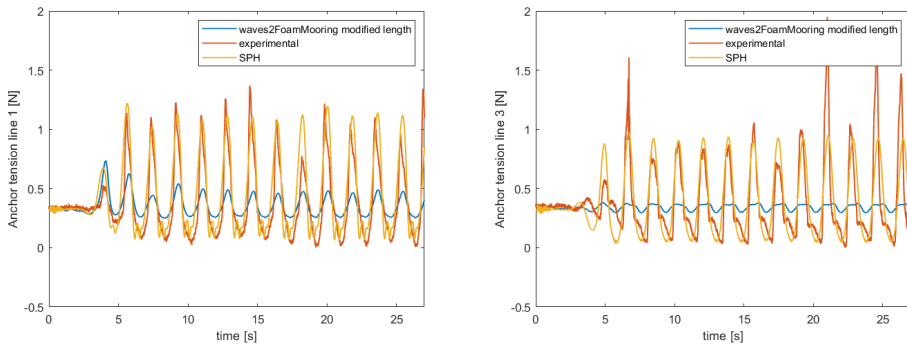


Figure B.4: Additional result comparing anchor tension of line 1 between waves2Foam-Mooring model with adjusted length, experimental, and SPH

# C

## MESH CONVERGENCE

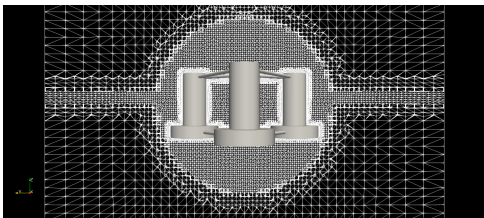


Figure C.1: Coarse mesh, front view

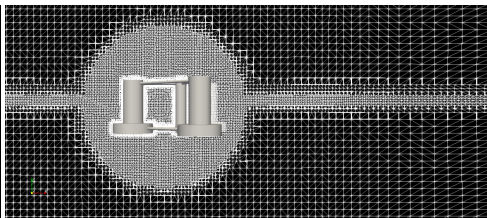


Figure C.2: Coarse mesh, side view

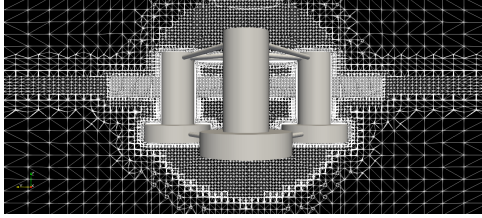


Figure C.3: Medium-coarse mesh, front view

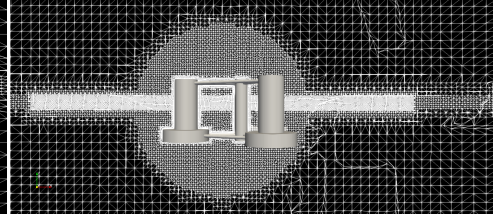


Figure C.4: Medium-coarse mesh, side view

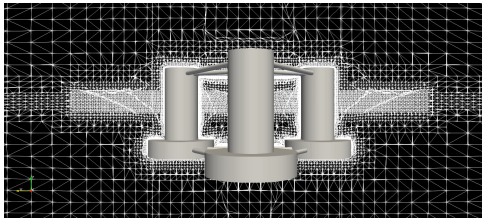


Figure C.5: Medium-fine mesh, front view

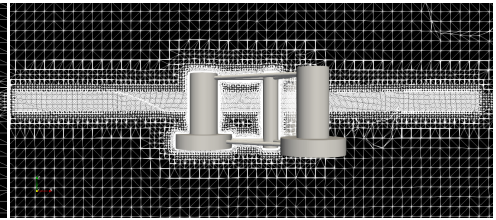


Figure C.6: Medium-fine mesh, side view

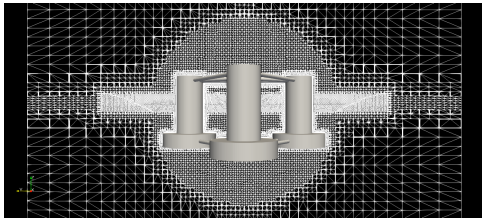


Figure C.7: Fine mesh, front view

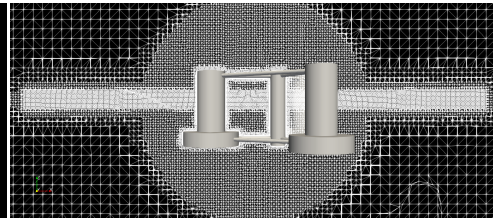


Figure C.8: Fine mesh, side view